

Copyright
by
Robert Raymond Luter, Jr.
2004

The Dissertation Committee for Robert Raymond Luter, Jr.
certifies that this is the approved version of the following dissertation:

Dynamic Tunneling and Chaos in Atom Optical Systems

Committee:

Linda E. Reichl, Supervisor

Mark G. Raizen

William C. Schieve

Qian Niu

Robert T. Wyatt

**Dynamic Tunneling and Chaos in Atom Optical
Systems**

by

Robert Raymond Luter, Jr., B.S., M.S.

DISSERTATION

Presented to the Faculty of the Graduate School of

The University of Texas at Austin

in Partial Fulfillment

of the Requirements

for the Degree of

DOCTOR OF PHILOSOPHY

THE UNIVERSITY OF TEXAS AT AUSTIN

December 2004

Dedicated to my parents
who encouraged me to search for truth.

Acknowledgments

I wish to express my gratitude to my advisor, Prof. Linda Reichl. She encouraged me when I needed it and got me back on the road too many times to count. I'm very grateful for her patience and her insight. I also want to thank Greg Morrow. Early discussions with him were the starting point for my research. Dr. Mark Raisen and his group have been very helpful. His group's experiments were the inspiration for much of the work I've done. Recent collaboration with Ben Holder has also been very stimulating. I look forward to continuing our work together. Finally, I want to thank my friend, Brian La Cour. We've had many discussions about life, physics, and work. These talks have helped keep me sane throughout this process.

Dynamic Tunneling and Chaos in Atom Optical Systems

Publication No. _____

Robert Raymond Luter, Jr., Ph.D.
The University of Texas at Austin, 2004

Supervisor: Linda E. Reichl

Dynamical tunneling has been observed in atom optics experiments by two groups, one in Texas using Cesium atoms and the other at NIST using a Bose–Einstein condensate. This tunneling is classically forbidden due to the isolation of the atoms in momentum space. The experimental results are extremely well described by time-periodic Hamiltonians with momentum quantized in units of the atomic recoil. The oscillations observed in these experiments are due to a few Floquet states that were excited by the initial conditions in the experiment. The observed tunneling has a well defined period when only two Floquet states dominate the dynamics. Beat frequencies are observed when three Floquet states dominate. Frequencies which are calculated theoretically match those observed by both experiments. The dynamical origin of the dominant Floquet states is identified as resulting from states which are excited by the initial conditions of the experiment.

Table of Contents

| | |
|--|-----------|
| Acknowledgments | v |
| Abstract | vi |
| List of Figures | x |
| Chapter 1. Introduction | 1 |
| 1.1 Atom Optics | 1 |
| 1.2 Classical Chaos | 3 |
| 1.3 Quantum Chaos | 3 |
| 1.4 Tunneling | 4 |
| Chapter 2. General Theory | 7 |
| 2.1 Double Well System | 7 |
| 2.1.1 Energy Levels | 7 |
| 2.1.2 Wave Functions | 10 |
| 2.1.3 Tunneling | 11 |
| 2.2 Classical Chaos | 14 |
| 2.2.1 Poincaré Surfaces of Section | 14 |
| 2.2.1.1 Henon-Heiles Example | 15 |
| 2.3 Periodic Hamiltonians | 17 |
| 2.3.1 Strobe Plots | 18 |
| 2.3.1.1 Underwater Acoustics Example | 18 |
| 2.3.2 Floquet Theory | 25 |
| 2.3.3 Husimi Plots | 29 |
| 2.4 Hamiltonians in Atom Optics | 30 |
| 2.4.1 Pendulum | 31 |
| 2.5 Dynamic Tunneling | 34 |

| | | |
|-------------------|---|-----------|
| 2.5.1 | Modulated Potential Well View | 35 |
| 2.5.2 | Moving Lattice View | 38 |
| Chapter 3. | Texas Experiment | 40 |
| 3.1 | Experiment Hamiltonian | 40 |
| 3.1.1 | System Model | 40 |
| 3.1.2 | Hamiltonian Derivation | 42 |
| 3.1.3 | Hamiltonian Scaling | 46 |
| 3.2 | Experimental Results | 47 |
| 3.3 | Theoretical Hamiltonian | 47 |
| 3.4 | Classical Dynamics | 49 |
| 3.5 | Quantum Evolution | 54 |
| 3.6 | Floquet Analysis | 59 |
| Chapter 4. | Nist Experiment | 74 |
| 4.1 | Experiment Hamiltonian | 74 |
| 4.1.1 | System Model | 74 |
| 4.1.2 | Hamiltonian Derivation | 74 |
| 4.1.3 | Hamiltonian Scaling | 75 |
| 4.2 | Experimental Results | 75 |
| 4.3 | Theoretical Hamiltonian | 76 |
| 4.4 | Classical Dynamics | 77 |
| 4.5 | Quantum Evolution | 78 |
| 4.6 | Floquet Analysis | 79 |
| 4.6.1 | Floquet States for Fixed Pendulum Amplitude at $\kappa = 1.66$ and Varying Modulation ε | 82 |
| 4.6.2 | Floquet States for Varying Pendulum Amplitude κ and Fixed Modulation at $\varepsilon = 0.29$ | 89 |
| Chapter 5. | Conclusions | 96 |
| | Appendix | 99 |

| | |
|--|------------|
| Appendix 1. Computer Codes | 100 |
| 1.1 Lyapunov Exponent | 100 |
| 1.2 Quantum Floquet Analysis | 105 |
| Bibliography | 112 |
| Index | 121 |
| Vita | 123 |

List of Figures

| | | |
|------|---|----|
| 2.1 | Double well potential for the infinite square well. | 8 |
| 2.2 | First four energy eigenvalues for the infinite double square well with a barrier width of $W = 0.2$ | 9 |
| 2.3 | First two eigenstates for the infinite double square well with a barrier width of $W = 0.2$ | 10 |
| 2.4 | Second pair of eigenstates for the infinite double square well with a barrier width of $W = 0.2$ | 12 |
| 2.5 | Left and right localized states for the infinite double square well with a barrier width of $W = 0.2$ | 13 |
| 2.6 | Poincaré surfaces of section for the Henon-Heils Hamiltonian. (a) $E = 1/24$, (b) $E = 1/12$, (c) $E = 1/8$, (d) $E = 1/6$ | 16 |
| 2.7 | Munk sound speed profile (blue) with range of internal wave perturbation (red) for $A = 0.01$ | 20 |
| 2.8 | Fan of 30 acoustic rays with $10^\circ \leq \theta \leq 10^\circ$ and a bottom depth of 5km. (a) $A = 0.0$, regular rays, (b) $A = 0.01$, distorted rays. | 21 |
| 2.9 | Strobe plot for $A = 0.01$, bottom depth of 5km, and $R = 10$ km. | 22 |
| 2.10 | Strobe plot for $A = 0.01$, bottom depth of 3km, and $R = 10$ km. | 23 |
| 2.11 | Lyapunov exponent calculation using an ensemble of initial points. | 24 |
| 2.12 | Lyapunov exponent as a function of range for selected rays with $R = 10$ km, bottom depth of $z_b = 5$ km, and amplitude $A = 0.01$ | 25 |
| 2.13 | Sticky state. Each of the dots is a strobe point from the same ray. | 26 |
| 2.14 | Energy eigenvalues of the quantum pendulum. | 32 |
| 2.15 | Husimi functions of the first four eigenvectors of the quantum pendulum for an amplitude of $A = 2.5$ | 33 |
| 2.16 | Husimi functions of eigenvectors 5-8 of the quantum pendulum for an amplitude of $A = 2.5$ | 34 |
| 2.17 | Modulated potential viewpoint of dynamic tunneling for the Texas Hamiltonian. | 36 |
| 2.18 | Modulated potential viewpoint of dynamic tunneling for the NIST Hamiltonian. | 37 |

| | | |
|------|--|----|
| 2.19 | Moving lattice viewpoint of dynamic tunneling. | 39 |
| 3.1 | Classical strobe plots of the Texas Hamiltonian with $\omega = 6.0$ at selected potential strengths. | 50 |
| 3.2 | Strobe plot for three trajectories at $\alpha = 9.7$ | 53 |
| 3.3 | Momentum evolution for three trajectories at $\alpha = 9.7$ | 54 |
| 3.4 | Evolution of momentum expectation value, $\langle n \rangle$ (in dimensionless units) for the Texas Hamiltonian. | 56 |
| 3.5 | Power spectral density plots for the Texas Hamiltonian. | 57 |
| 3.6 | Oscillation frequencies, $\Delta\Omega = (\Omega_j - \Omega_i)$, calculated from the Floquet eigenphase differences for varying dimensionless field strengths, α | 61 |
| 3.7 | Floquet eigenphases for the Texas Hamiltonian with 81 states as a function of α | 63 |
| 3.8 | Dominant Floquet eigenphases as a function of α for the Texas Hamiltonian with $\omega = 6.0$, $n_0 = 4.2$, and $\phi_0 = 0$ | 64 |
| 3.9 | Husimi plots of Floquet eigenstates for the Texas experiment for $\omega = 6.0$ and $\alpha = 9.7$ | 66 |
| 3.10 | Husimi plots of Floquet eigenstate 3 for the Texas Hamiltonian with $\omega = 6.0$ and selected values of α | 67 |
| 3.11 | Husimi plots of Floquet eigenstate 4 for the Texas Hamiltonian with $\omega = 6.0$ and selected values of α | 70 |
| 3.12 | Floquet eigenstates projected onto momentum for the Texas Hamiltonian at $\alpha = 2.0$ | 71 |
| 3.13 | Husimi plots of Floquet eigenstate 5 for the Texas Hamiltonian with $\omega = 6.0$ and selected values of α | 72 |
| 3.14 | Husimi plots of Floquet eigenstate 6 for the Texas Hamiltonian with $\omega = 6.0$ and selected values of α | 73 |
| 4.1 | Classical strobe plots for the NIST Hamiltonian at $\kappa = 1.66$ and selected values of ε | 78 |
| 4.2 | Evolution of momentum expectation value, $\langle n \rangle$ (in dimensionless units) for the NIST experiment. | 79 |
| 4.3 | Husimi plots of Floquet eigenstates for the NIST experiment with $\kappa = 1.66$, $\varepsilon = 0.29$, $\omega = 2.5$ and $\omega_m/2\pi = 250\text{kHz}$ | 80 |
| 4.4 | Floquet eigenphases for NIST experiment for 11 states as a function of ε at $\kappa = 1.66$ | 83 |

| | | |
|------|--|----|
| 4.5 | Husimi plots of Floquet eigenstates at $\kappa = 1.66$ and selected values of ε for the avoided crossing at $\varepsilon = 0.51$ | 84 |
| 4.6 | Husimi plots of Floquet eigenstates at $\kappa = 1.66$ and selected values of ε for the avoided crossing at $\varepsilon = 0.82$ | 85 |
| 4.7 | Husimi plots of Floquet eigenstates at $\kappa = 1.66$ and selected values of ε for the avoided crossings at $\varepsilon = 1.6$ | 86 |
| 4.8 | Oscillation frequencies as a function of ε at $\kappa = 1.66$ with a threshold of $P_i P_j = 4\%$ of combined overlap. | 87 |
| 4.9 | Oscillation frequencies as a function of κ at $\varepsilon = 0.29$ with a threshold of $P_i P_j = 4\%$ of combined overlap. | 88 |
| 4.10 | Classical strobe plots for NIST experiments at $\varepsilon = 0.29$ and selected values of κ | 89 |
| 4.11 | Husimi plots of Floquet eigenstates at $\varepsilon = 0.29$ and selected values of κ for the avoided crossing at $\kappa = 0.55$ | 91 |
| 4.12 | Floquet eigenphases for NIST Hamiltonian for 7 states as a function of κ at $\varepsilon = 0.29$ | 92 |
| 4.13 | Husimi plots of Floquet eigenstates for NIST experiments at $\varepsilon = 0.29$ and selected values of κ for the avoided crossing at $\kappa = 1.19$ | 93 |
| 4.14 | Husimi plots of Floquet eigenstates at $\varepsilon = 0.29$ and selected values of κ for the avoided crossing at $\kappa = 1.57$ | 94 |

Chapter 1

Introduction

This dissertation examines atom optical systems that exhibit quantum dynamic tunneling between regions separated in phase space by momentum. The main tool for analysis is the application of Floquet theory to the time-periodic Hamiltonians of the dynamical systems.

1.1 Atom Optics

In 1970, Ashkin proposed using a radiation pressure force to transfer momentum from a traveling laser wave to neutral two-level atoms [2]. The beam of radiation connects the ground state with an excited state. Experimental observation of this momentum transfer was made few years later [48, 56]. Eventually, it was discovered that this light pressure force could cool atoms [26] and ions. Kinetic energy is transferred from a low-density gas when it is illuminated by an intense laser which is at the lower-frequency half of the resonance line's Doppler width.

The interaction between the laser light and neutral atoms is due to a dipole moment that comes from the spatial distribution of electrons and protons within the atom. Since atoms have well defined internal energy values,

the interaction is a resonance between the atom and laser. The interaction is stronger when the difference between the frequency of the laser and the atomic transition is small. In general, the intensity of light depends upon the atom's position, while the force on the atom depends upon the gradient of the intensity.

Spontaneous emission occurs when light is scattered into a vacuum mode. This emission can be treated as a stochastic process using a density operator. The effect of the spontaneous emission is to damp the excited state, give random kicks to the atom, and disrupt the coherent evolution governed by Schrodinger's equation. Stimulated emission can be made to dominate over spontaneous emission by detuning the laser. If $\delta = \omega_L - \omega_0$ is large compared to the Rabi frequency, Ω , the atom makes a virtual transition to a higher energy state. After a short time, $\delta t \approx 1/\delta$, the atom most likely undergoes stimulated emission rather than spontaneous emission which could require more time.

The net effect of the laser is not on the internal state of the atom, but on its center-of-mass momentum. The momentum changes by $\hbar k_L$ with each coherent transition between the atom's internal states. If the atom emits a quanta of momentum $\hbar k_L$ in the same direction, then no net change to the atom's momentum takes place. However, if the momentum is emitted in the opposite direction, $-\hbar k_L$, then there is a net momentum change for the atom of $2\hbar k_L$.

The study of quantum nonlinear dynamics with cold atom was proposed by Graham, Schlautmann, and Zoller [24]. The wave nature of the atoms

must be taken into account since the de Broglie wavelength of cold atoms is large. Because the atoms are so cold, dissipation and noise is reduced. The optical potential that interacts with the atoms can be approximated as a one-dimensional potential. The experimentalists are able to exert control over this potential through various techniques. In this thesis, amplitude modulated potentials are studied.

1.2 Classical Chaos

In a mixed phase space of a classical system there are regions of regular dynamics and regions in which the dynamics exhibits chaotic behavior. The regular regions are sometimes isolated within a chaotic sea as stable resonant islands of stability. Classical transport between these islands is forbidden by KAM (Kolmogorov-Arnol'd-Moser) tori which act as dynamical barriers in the phase space. In the quantum regime, it is possible for tunneling between two stable islands to take place. The wave packet can then oscillate between the resonances.

1.3 Quantum Chaos

Quantum chaos concerns itself with the study of systems which are non-integrable in the corresponding classical systems. The three main areas of study in quantum chaos are semi-classical quantization, quantum ergodic theory, and quantum signatures of classical chaos. In trying to understand which systems should be subject to the Bohr-Sommerfeld-Epstein quantization rules,

Albert Einstein initiated the field of quantum chaos [20]. He concluded that the rules cannot be used when there are no invariant tori. Using periodic orbit theory, Gutzwiller semiclassically quantized a classically chaotic system [25]. Random matrix theory enabled Bohigas to find a relationship between the statistical properties of the spectra of a quantum system and its corresponding classical system's chaotic dynamics [7, 8].

1.4 Tunneling

In a static double-well potential, the states have definite parity due to the symmetry of the potential. As the barrier goes to infinity, the states become degenerate and increasingly have support only within the two wells.

Dynamical tunneling occurs when classical transport is forbidden due to system dynamics rather than a potential barrier. Classical trajectories become trapped in phase space regions of regular dynamics which are separated from other regions by an impenetrable barrier of chaotic dynamics. Quantum mechanics couples wave functions which are in the regular regions and allows dynamic tunneling [16]. The quantum levels corresponding to symmetric and separated tori are quasidegenerate [9, 10].

The idea that chaos can affect tunneling in a time dependent Hamiltonian was introduced by Lin and Ballentine [37]. They studied a particle in a double-well potential with an external oscillating driving field. The oscillatory driving force acts to replace the separatrix between the wells with a variable sized chaotic layer. Coherent tunneling oscillations between two stable islands

were observed when an initial coherent state was placed on one of the islands and then allowed to evolve in time. It was found that the tunneling rate with the chaos present was greater than ordinary tunneling without the driving field. Peres pointed out that a dynamical symmetry of the Hamiltonian,

$$H(p, x, t) = H(-p, -x, t + \pi/\omega), \quad (1.1)$$

was the cause of the increase in the tunneling rate [27, 47].

Chaos assisted tunneling was first described by Tomsovic and Ullmo [69]. Systems with symmetries have states which are degenerate to any power of \hbar . The degeneracies are lifted by tunneling, either by direct tunneling or by chaos assisted tunneling. The chaos assisted tunneling mechanism involves chaotic states which act as intermediaries for the tunneling. A crossing mechanism exists in which a chaotic level passes near two tunneling levels of states with opposite parity and affects the tunneling rates. The first experimental evidence of chaos assisted tunneling was obtained by Dembowski using a superconducting cavity [17, 23]. A number of systems have been studied which exhibit chaos assisted tunneling [34, 44].

In this study, I will analyze the recent dynamic tunneling experiments of the Texas and NIST groups using Floquet theory. Additionally, coherent states placed at the experimental location of the atoms will be evolved in time in a manner similarly to Lin and Ballentine [37]. The tunneling oscillations are affected by the symmetry of the quantum Floquet states and the characteristics of the initial state. The frequencies of the oscillations are ultimately

determined by the frequency differences in the eigenvalues of the Floquet states which are prominent in the decomposition of the initial state.

Chapter 2

General Theory

2.1 Double Well System

In order to understand dynamic tunneling, it is helpful to examine the more familiar tunneling which occurs in systems with a potential barrier. In order to make things simpler, I will examine the double well system using an infinite square well with a potential barrier in its center. The width of the total well is set to 1. The central inner potential barrier has a width of $W = 0.2$ and a variable height of V_0 as shown in Fig. 2.1. The walls of the outer wells have infinite potential, while the inner potential between the two wells and the central barrier is set to zero,

$$V(x) = \begin{cases} V_0, & \text{if } |x| < W/2; \\ 0, & \text{if } W/2 \leq |x| < 0.5; \\ \infty, & \text{otherwise.} \end{cases} \quad (2.1)$$

2.1.1 Energy Levels

The four lowest eigenvalue energies are plotted in Fig. 2.2. At $V_0 = 0$, the double well becomes the simple infinite square well with energies that are proportional to n^2 . As the magnitude of barrier potential increases, each of the symmetric ($|S\rangle$) and antisymmetric ($|A\rangle$) states pair up with a state of

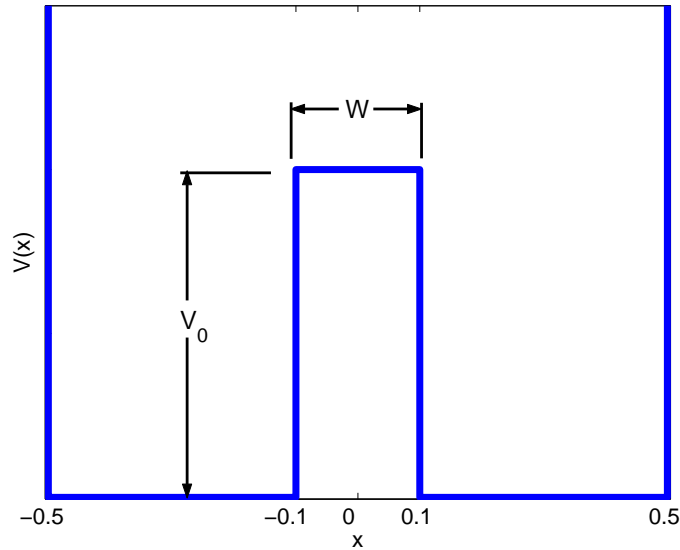


Figure 2.1: Double well potential for the infinite square well. The barrier height, V_0 , is variable, while its width, $W = 0.2$. The sides of the double well have infinite potential, so the wavefunction is bound within it.

the opposite parity and grow closer in energy to their partner. Eventually, each state becomes nearly degenerate. Only when the barrier reaches infinite potential does actual degeneracy take place [54].

The energy curves have positive slope because the energy eigenvalues must increase as the barrier potential gets larger. The growing barrier causes the eigenvectors to have greater curvature since they must increase curve closer to the axis at the barrier boundaries in order to avoid the classically forbidden region. This added curvature corresponds to a larger eigenvalue according to Schrödinger's equation.

The symmetric states are lower in energy than their corresponding an-

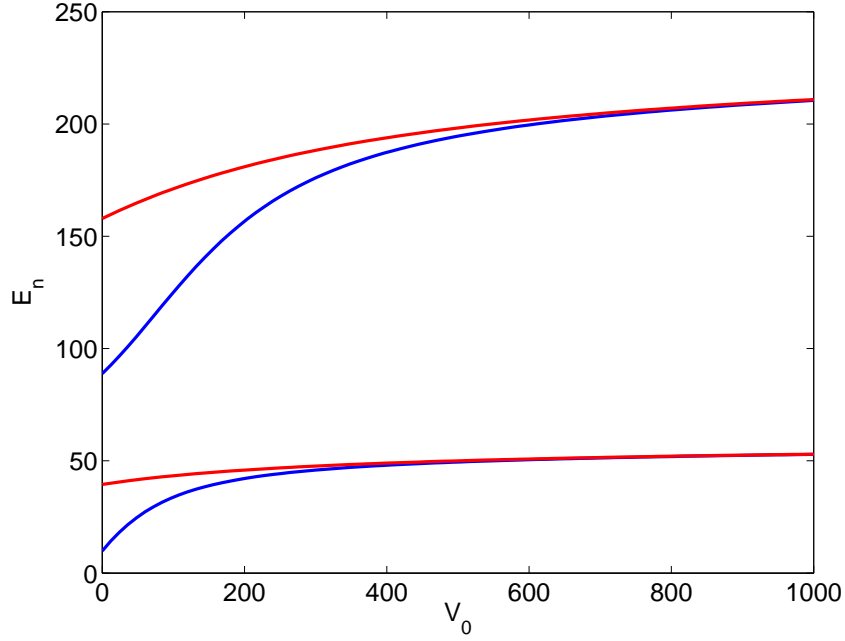


Figure 2.2: First four energy eigenvalues for the infinite double square well with a barrier width of $W = 0.2$. Both E_n and V_0 are scaled by $\hbar^2/2m$. The states are numbered according to their energy order. The blue curves correspond to the symmetric states 1 and 3, while the red curves are the antisymmetric states 2 and 4. For $V_0 = 0$, the eigenvalues are $E_n = n^2\pi^2$. At $V_0 = 1000$, the eigenvalues are $E_1 = 52.88354$, $E_2 = 52.947019$, $E_3 = 210.54438$, and $E_4 = 210.93595$.

antisymmetric states because of curvature. The antisymmetric states have to curve enough to cross the axis one additional time more than the previous symmetric state which is at a lower energy. As a result, the even and odd states alternate in Fig. 2.2 as energy increases. As the barrier increases, the eigenvalues of each state within a pair come closer together because the difference in curvature between the two states becomes very small.

2.1.2 Wave Functions

As the height of the potential barrier increases, the wave functions are distorted from their original sinusoidal shapes that occurs for a infinite square well with no barrier. States 1 and 2 are shown in Fig. 2.3. The four parts of the

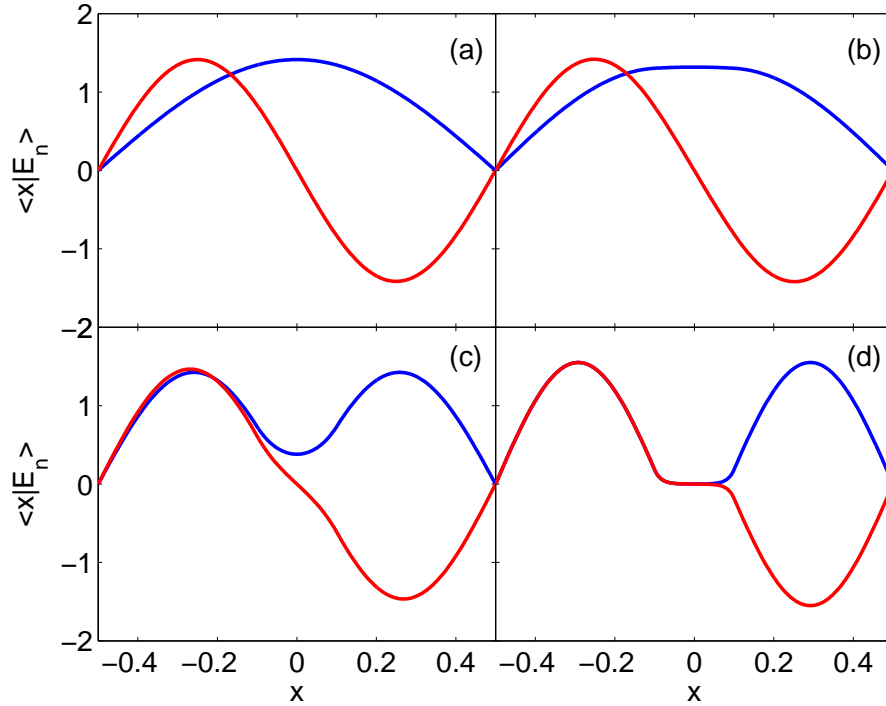


Figure 2.3: First two eigenstates for the infinite double square well with a barrier width of $W = 0.2$. The blue curves are state 1 and the red curves are state 2. (a) $V_0 = 0$, $E_1 = 9.8696$, $E_2 = 39.4784$, (b) $V_0 = 12$, $E_1 = 14.2609$, $E_2 = 40.0447$, (c) $V_0 = 204$, $E_1 = 42.3148$, $E_2 = 45.9576$, (d) $V_0 = 4008$, $E_1 = 57.0770$, $E_2 = 57.0770$. The energy and potential are scaled by $\hbar^2/2m$.

figure show two wave functions as the potential barrier increases. In Fig. 2.3a, there is no barrier, so we have only the infinite square well and the usual

sine waves. As soon as the central barrier is turned on, the wave functions are distorted. This is obvious for state 1 in Fig. 2.3b. It is still concave inward toward the axis, since the eigenvalue energy is greater than the barrier potential. After increasing the potential some more, the energy eigenvalues are finally less than the potential in Fig. 2.3c. This causes both states to have concave outward shapes within the barrier region. In Fig. 2.3d, the potential has been ramped up almost 20 times that of Fig. 2.3c. This causes the two states to have very small probabilities within the barrier. Notice that the two states are almost identical except for the parity difference. This is reflected in the energy eigenvalues which are degenerate to a precision of 10^{-5} .

The next two states are shown in Fig. 2.4. A similar progression to that of Fig. 2.3 is shown. In this case, it is much more difficult to see the distortion in the wave functions. Once the eigenvalue becomes less than the potential, as in Fig. 2.4c, the change from concave inward to concave outward becomes obvious. Finally, for $V_0 = 4008$ in Fig. 2.4d, the two wave functions have once again become nearly identical except for parity.

2.1.3 Tunneling

Tunneling occurs when a particle is initially confined in one of the two wells,

$$|R\rangle = \frac{1}{\sqrt{2}} (|S\rangle - |A\rangle), \quad (2.2)$$

$$|L\rangle = \frac{1}{\sqrt{2}} (|S\rangle + |A\rangle), \quad (2.3)$$

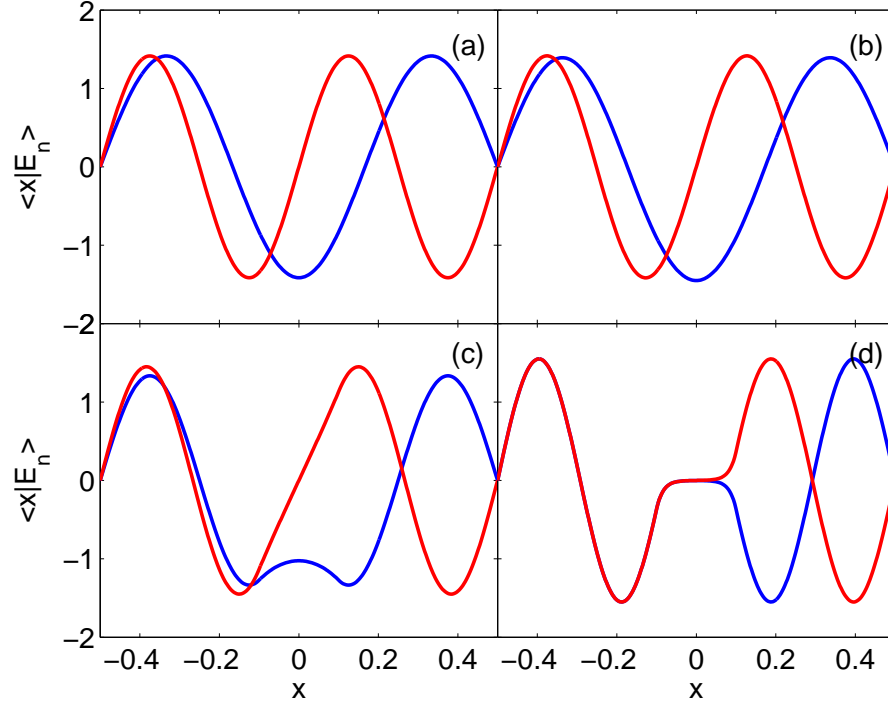


Figure 2.4: Second pair of eigenstates for the infinite double square well with a barrier width of $W = 0.2$. The blue curves are state 3 and the red curves are state 4. (a) $V_0 = 0$, $E_3 = 88.8264$, $E_4 = 157.9137$, (b) $V_0 = 12$, $E_3 = 92.5821$, $E_4 = 159.7209$, (c) $V_0 = 204$, $E_3 = 157.6799$, $E_4 = 181.3016$, (d) $V_0 = 4008$, $E_3 = 228.1804$, $E_4 = 228.1804$. The energy and potential are scaled by $\hbar^2/2m$.

where $|R\rangle$ is mostly confined to the right well and $|L\rangle$ is mostly in the left well as shown in Fig. 2.5. All of the states shown are combinations of the energy eigenstates. Fig. 2.5a and Fig. 2.5b are for a smaller potential barrier than for Fig. 2.5c and Fig. 2.5d. As a result, there is a noticeable amount of probability in the opposite wells. For the last two wavefunctions, the barrier is so high that almost no leakage into the opposite well occurs.

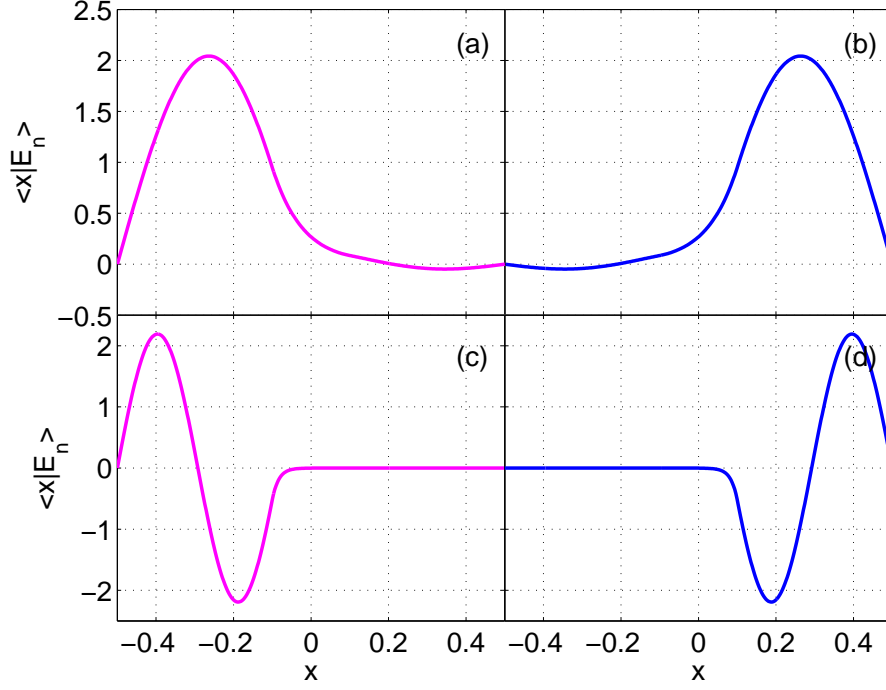


Figure 2.5: Left and right localized states for the infinite double square well with a barrier width of $W = 0.2$. The magenta curves are state $|L\rangle$ and the blue curves are state $|R\rangle$. (a) $|L_1\rangle = (|E_1\rangle + |E_2\rangle)/\sqrt{2}$ for $V_0 = 204$, (b) $|R_1\rangle = (|E_1\rangle - |E_2\rangle)/\sqrt{2}$ for $V_0 = 204$, (c) $|L_2\rangle = (|E_3\rangle + |E_4\rangle)/\sqrt{2}$ for $V_0 = 4008$, (d) $|L_2\rangle = (|E_3\rangle - |E_4\rangle)/\sqrt{2}$ for $V_0 = 4008$. The energy and potential are scaled by $\hbar^2/2m$.

These are nonstationary states that oscillate between the two wells with a frequency of $\omega = (E_A - E_S)/\hbar$. This result becomes evident by applying the time-evolution operator to these states,

$$|R(t)\rangle = \hat{U}(t) |R\rangle \quad (2.4)$$

$$= \frac{1}{\sqrt{2}} e^{-iE_S t/\hbar} (|S\rangle - e^{-i(E_A - E_S)t/\hbar} |A\rangle) \quad (2.5)$$

$$= |L(t + \pi\hbar/(E_A - E_S))\rangle. \quad (2.6)$$

Thus, the wave function in Fig. 2.5a changes into the one in Fig. 2.5b and the Fig. 2.5c wave function changes into the wave function of Fig. 2.5d after a period of $T_{L \rightarrow R} = T/2 = \pi \hbar / (E_A - E_S)$. The barrier height is much greater for Fig. 2.5c and Fig. 2.5d than for the first two parts of the figure. As a result, their frequency of oscillation is much smaller. As long as the eigenstates are not degenerate, which only happens when each well is completely isolated from the other, there must be oscillation between the two wells.

Note that computationally, degeneracy becomes a problem. With finite precision, two states that should actually be non-degenerate with a given potential strength, may appear to be degenerate. When this occurs, parity must be explicitly imposed, since non-parity wavefunctions are computationally permissible.

2.2 Classical Chaos

After quantum tunneling, the next element that needs to be considered is chaotic dynamics. Classical chaos in 2-dimensional systems provides a good starting point. These systems have many of the features of the atomic optic systems that are ultimately of interest.

2.2.1 Poincaré Surfaces of Section

A Poincaré surface of section is a means for analyzing autonomous, two degree of freedom, near-integrable Hamiltonian flows. For these systems, phase space is four dimensional. The surface of section reduces the flow to a

mapping on a two-dimensional surface. Each time a trajectory of the system passes through a select plane in a given direction, the intersection point is recorded.

Since the trajectory lies on a three-dimensional energy surface, if another constant of the motion exists, the resulting mapping on the surface of section will be a closed curve. If the mapping does not result in a curve, then the constant of the motion must not exist.

2.2.1.1 Henon-Heiles Example

The Henon-Heiles problem was first studied in its connection to galactic motion in the 1960s ???. It is much discussed in the literature on chaos [36, 50].

The Hamiltonian is

$$H = \frac{1}{2} (p_x^2 + p_y^2) + \frac{1}{2} (x^2 + y^2) + x^2 y - \frac{1}{3} y^3 = E. \quad (2.7)$$

Note the nonlinear terms in the potential. The equilibrium points are

$$\dot{x} = \dot{p}_x = \dot{y} = \dot{p}_y = 0. \quad (2.8)$$

The equations of motion are

$$\begin{aligned} \dot{p}_x &= -\frac{\partial H}{\partial x} = -x - 2xy, \\ \dot{p}_y &= -\frac{\partial H}{\partial y} = -y - x^2 + y^2, \\ \dot{x} &= \frac{\partial H}{\partial p_x} = p_x, \\ \dot{y} &= \frac{\partial H}{\partial p_y} = p_y. \end{aligned} \quad (2.9)$$

For the surface of sections in Fig. 2.6, $x = 0$ and $p_x > 0$ define the mapping. For $E < 1/6$, the motion is bounded. If the energy is greater than this, the

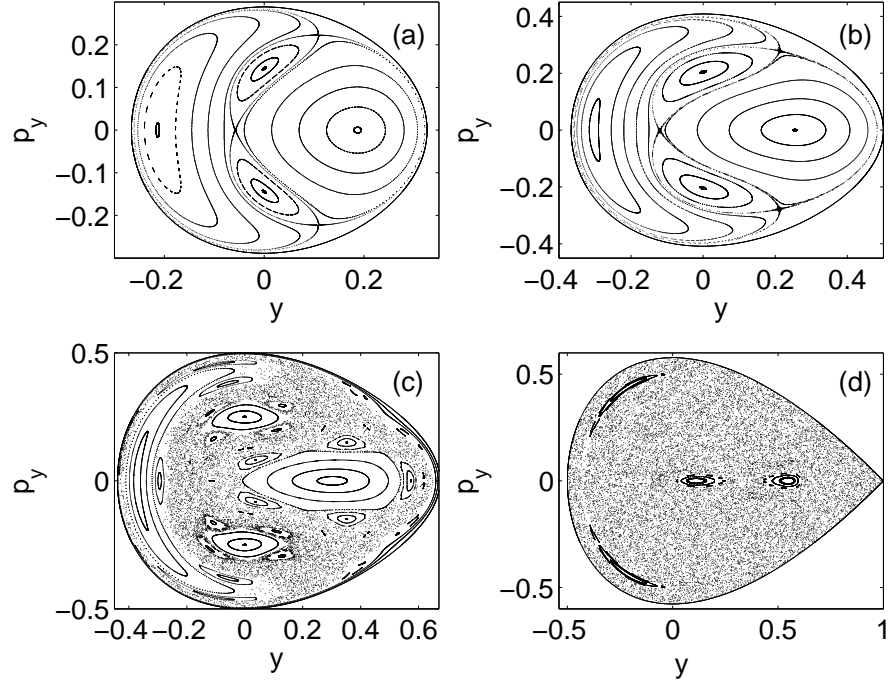


Figure 2.6: Poincaré surfaces of section for the Henon-Heiles Hamiltonian. (a) $E = 1/24$, (b) $E = 1/12$, (c) $E = 1/8$, (d) $E = 1/6$.

motion becomes unbounded.

Within the boundaries, the motion is either regular or chaotic, depending on the energy of the system and the initial condition. In Fig. 2.6a, the energy is low enough that all trajectories are regular. No stochastic orbits are observed. In Henon and Heiles original paper, they calculated the measure of the regular orbits and found it to be 1 for all energies below a threshold. After the threshold, which starts at approximately $E = 1/12$, the measure of the

stochastic region suddenly increases. The start of this onset of chaotic orbits can be seen in Fig. 2.6b at the hyperbolic points of the middle island chain (e.g., $y = -0.12$, $p_y = 0$). What looks like two separate orbits surrounding the islands is actually one chaotic orbit that begins at an unstable hyperbolic point. A mixed phase space of regular orbits in the midst of a chaotic sea can be seen in Fig. 2.6c. Each of the stable equilibrium points has survived as resonance islands. In addition, new higher order resonances can be observed in the form of island chains in the region between the primary resonances. The KAM theorem tells us that if the perturbation is not too large, some invariant tori will survive. Fig. 2.6d shows a space in which almost all of these tori have been destroyed. All that is left is the chaotic sea with a few very small islands of regular motion.

In the analysis of atomic optic systems, the Hamiltonians will lend themselves to similar plots as these for the Henon-Heiles problem. The only feature missing is the boundary of the phase space which is such a distinctive feature of these plots. The boundary is defined at the location in the $x = 0$ plane where $\dot{p} = 0$. Any trajectory that has this property stays within the plane instead of the normal looping around for another iteration.

2.3 Periodic Hamiltonians

The Hamiltonians used in atom optics are periodic in time and space. This periodicity allows a simplification in the analysis of both the classical and the quantum behavior of the system. Strobe plots are used for the classical

analysis in a manner very similar to the Poincaré surfaces of section that are used for two degrees of freedom systems. In the quantum analysis, Floquet theory handles the time periodicity, while Floquet-Block theory also accounts for the spacial periodicity.

2.3.1 Strobe Plots

If a one degree of freedom, nonautonomous Hamiltonian is periodic in time,

$$H(q, p, t) = H(q, p, t + T), \quad (2.10)$$

strobe plots can be used to capture the dynamics.

2.3.1.1 Underwater Acoustics Example

Sound wave propagation in the ocean is often described using ray theory, just like in optics. The ray equations can be written in a Hamiltonian form,

$$H(z, r, k_z, k_r, t) = c(z, r) \sqrt{k_z^2 + k_r^2} = \omega_0. \quad (2.11)$$

This results in four equations of motion,

$$\begin{aligned} \frac{dz}{dt} &= \frac{\partial H}{\partial k_z} \\ \frac{dk_z}{dt} &= -\frac{\partial H}{\partial z} \\ \frac{dr}{dt} &= \frac{\partial H}{\partial k_r} \\ \frac{dk_r}{dt} &= -\frac{\partial H}{\partial r} \end{aligned} \quad (2.12)$$

This is way more complicated than we wish. Fortunately, a simplification can be made that reduces the phase space. If it is assumed that propagation is in the forward direction only ($\frac{\partial r}{\partial t} > 0$), a new Hamiltonian can be written,

$$H(z, k_z, r) = \sqrt{\frac{\omega_0^2}{c(z, r)^2} - k_z^2} = -k_r. \quad (2.13)$$

This equation potentially has the form of a one degree of freedom, nonautonomous Hamiltonian with r acting like the time variable. The equations of motion are now only two,

$$\frac{dz}{dr} = -\frac{k_z}{H(z, k_z, r)} = \frac{k_z}{k_r} \quad (2.14)$$

$$\frac{dk_z}{dr} = \frac{1}{H(z, k_z, r) c(z, r)^3} \frac{\partial c}{\partial z} \quad (2.15)$$

The range periodicity comes in through the sound speed profile. A typical range-independent analytical model for the sound speed profile is the Munk profile,

$$c(z) = c_a \left[1 + \varepsilon \left(e^{-2(z-z_a)/B} + \frac{2(z-z_a)}{B} - 1 \right) \right]. \quad (2.16)$$

This profile has a minimum value of c_a at the sound channel axis, z_a . Internal waves in the ocean can affect the sound speed. The Munk profile is modified with a very simple range-periodic internal wave perturbation,

$$\begin{aligned} c(z) = c_a & \left[1 + \varepsilon \left(e^{-2(z-z_a)/B} + \frac{2(z-z_a)}{B} - 1 \right) \right] \\ & + A \left(\frac{2z}{B} \right) e^{-2z/B} \cos \left(\frac{2\pi r}{R} \right), \end{aligned} \quad (2.17)$$

where R is the wavelength of the perturbation and A is the amplitude. This sound speed profile for a 5km deep ocean is shown in Fig. 2.7. Note that the

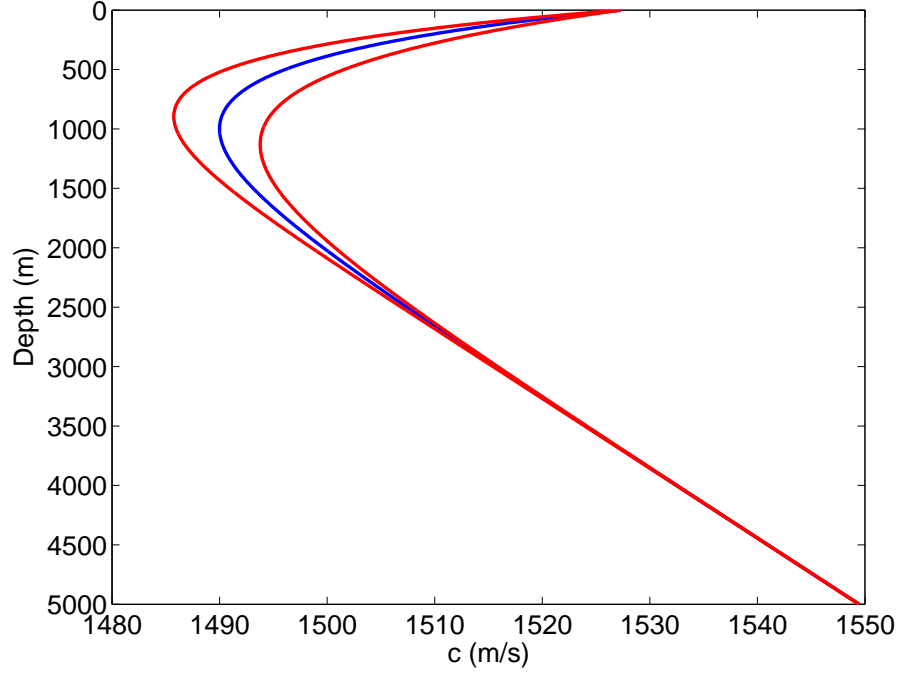


Figure 2.7: Munk sound speed profile (blue) with range of internal wave perturbation (red) for $A = 0.01$.

sound speed acts like a potential energy term in the usual Hamiltonians. The acoustic rays will therefore oscillate about the minimum sound speed just like a ball oscillates about a gravity potential minimum.

A fan of acoustic rays with and without the internal wave perturbation is shown in Fig. 2.8. While it is clear that the internal wave has cause distortion in the rays, it is not so obvious that any of the rays are chaotic. A strobe plot will be able to show the difference between the various rays.

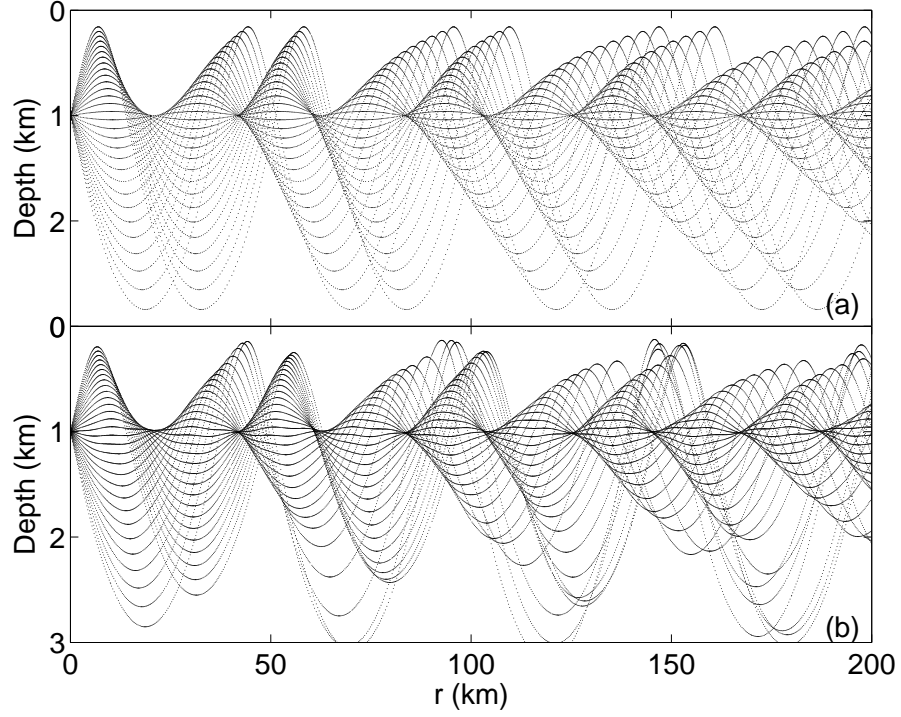


Figure 2.8: Fan of 30 acoustic rays with $10^\circ \leq \theta \leq 10^\circ$ and a bottom depth of 5km. (a) $A = 0.0$, regular rays, (b) $A = 0.01$, distorted rays.

For convenience, instead of plotting the wave vector, k_z , the grazing angle will be used instead,

$$\theta = -\tan\left(\frac{k_z}{H(z, k_z, r)}\right) \quad (2.18)$$

For $A = 0.01$, the strobe plot in Fig. 2.9 becomes a mixed phase space with a large stochastic sea, a central island, small island chains, and an outer region of KAM tori.

There are three parameters that can be changed to produce new strobe plots: the perturbation wavelength, R , the bottom depth, z_b , and the am-

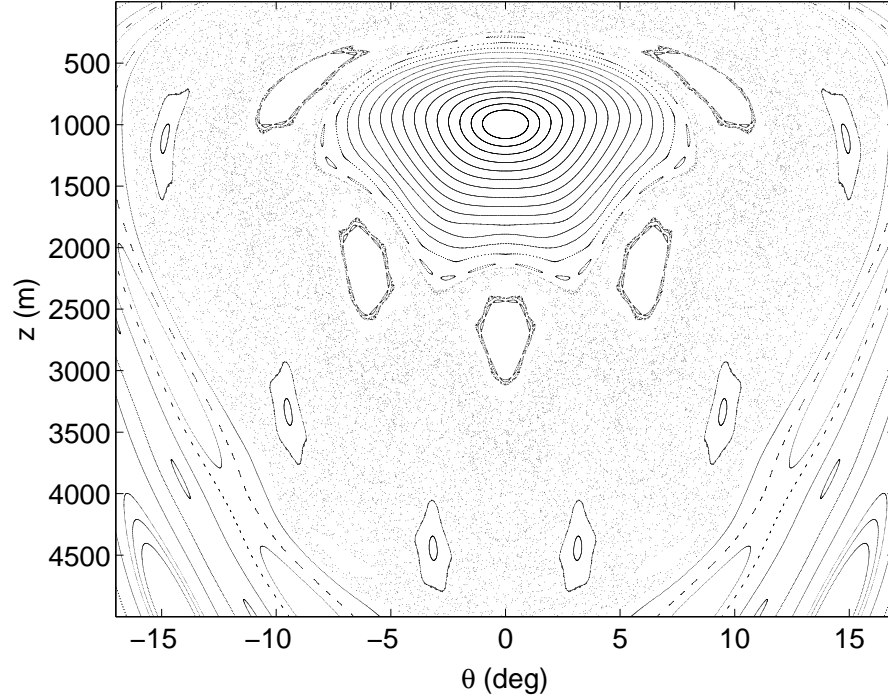


Figure 2.9: Strobe plot for $A = 0.01$, bottom depth of 5km, and $R = 10$ km.

plitude, A . The perturbation wavelength is important because it determines which rays will resonate. For example, if a ray completes an oscillation about the sound channel axis every 50km, then it will resonate with a perturbation wavelength of $R = 10$ km to produce a 5 island chain on the strobe plot. The bottom depth is important because steep rays will reflect off of it. These reflections can destroy resonances that existed for a deeper bottom, or they can create new resonances. As an example, Fig. 2.10 has the same basic structure as with the 5km strobe, but the resonance structure is different.

By far, however, the amplitude of the perturbation is the most impor-

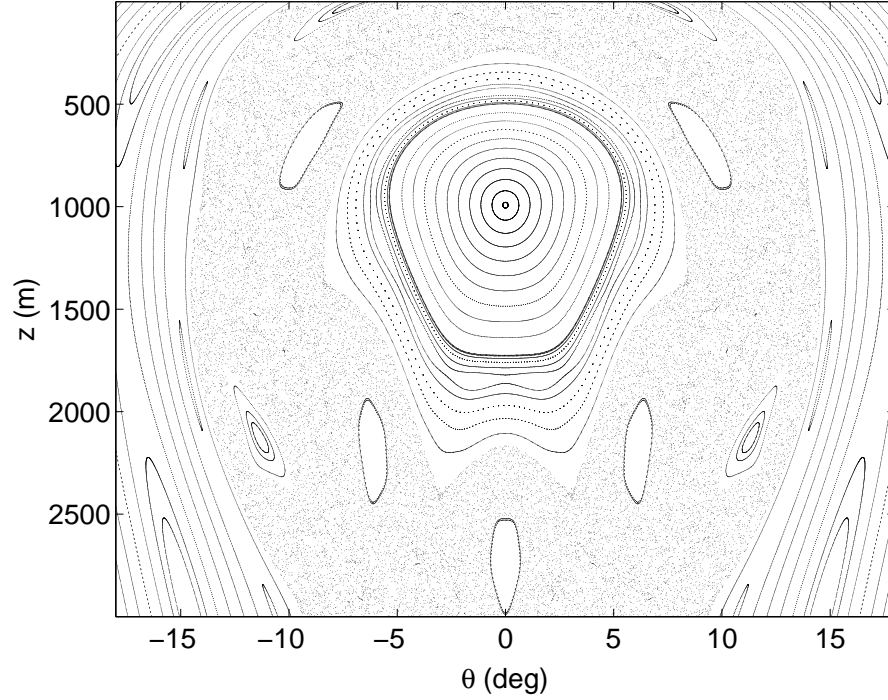


Figure 2.10: Strobe plot for $A = 0.01$, bottom depth of 3km, and $R = 10$ km.

tant factor in determining the detailed structure of the strobe plot. As the amplitude gets bigger, so does the chaotic sea, and that dominates everything. Additionally, the strength of the chaos increases as the amplitude increases as shown by the plot of Lyapunov exponents in Fig. 2.11. The chaos intensity can be measured using Lyapunov exponents since the inverse of the exponent gives the range at which one can no longer predict the trajectory of a ray. Thus, the larger the exponent, the sooner that predictability becomes impossible. A few rays have had their exponent calculated in Fig. 2.12. There are three types of rays shown: regular rays that have an exponent that goes to zero as

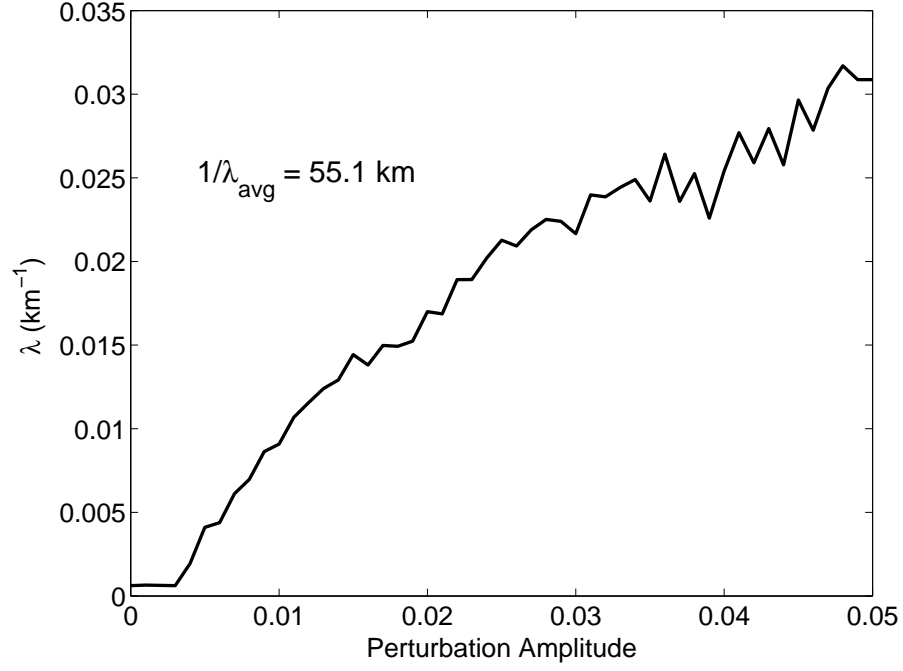


Figure 2.11: Lyapunov exponent calculation using an ensemble of initial points within the chaotic sea for $R = 10\text{km}$ and a bottom depth of $zb = 5\text{km}$.

the range increases, chaotic rays in the stochastic sea that have a finite value of the Lyapunov exponent, and sticky rays (Fig. 2.13) which are ultimately chaotic, but that have trajectories that run very close to a stable orbit. As a result, the sticky state starts off looking like its Lyapunov exponent will go to zero, but eventually, it joins the rest of the chaotic states with a finite value.

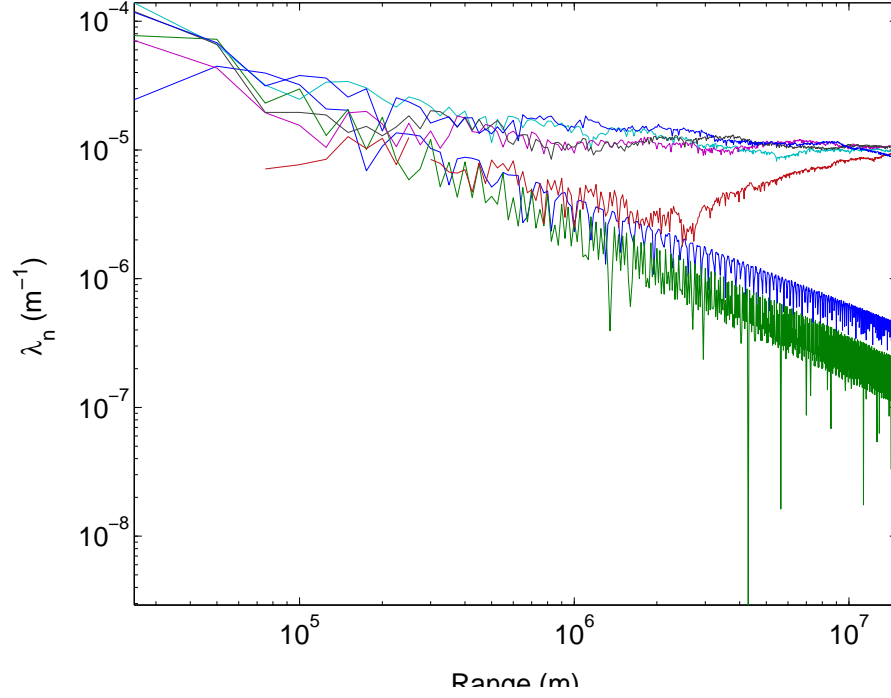


Figure 2.12: Lyapunov exponent as a function of range for selected rays with $R = 10\text{km}$, bottom depth of $z_b = 5\text{km}$, and amplitude $A = 0.01$.

2.3.2 Floquet Theory

Floquet theory can be used to analyze the quantum properties of the system, if the Hamiltonian is time periodic [55, 58, 71],

$$\begin{aligned}\hat{H}(t) &= \hat{H}_0 + \hat{V}(t) \\ &= \hat{H}(t+T),\end{aligned}\tag{2.19}$$

where the potential, $\hat{V}(t) = \hat{V}(t+T)$, is the source of the periodicity. The solution of Schrodinger's equation with a periodic Hamiltonian has the form

$$|\Psi_\alpha(t)\rangle = e^{-i\frac{\Omega_\alpha}{\hbar}t} |\Phi_\alpha(t)\rangle,\tag{2.20}$$

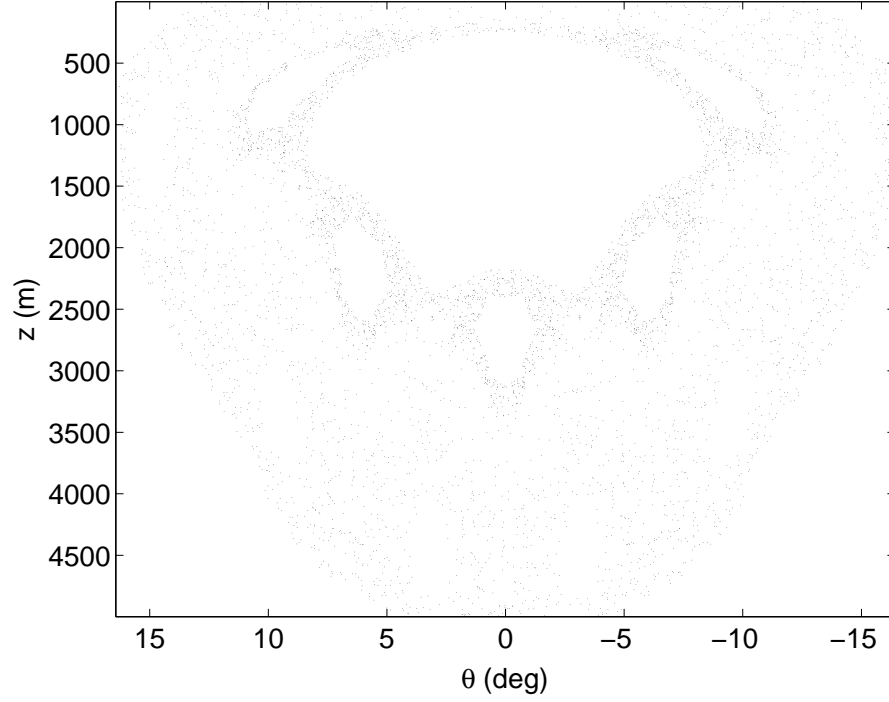


Figure 2.13: Sticky state. Each of the dots is a strobe point from the same ray.

where the Floquet states, $|\Phi_\alpha(t)\rangle = |\Phi_\alpha(t+T)\rangle$, have the same period as the Hamiltonian. The quasienergies and Floquet states obey the eigenvector equation,

$$\hat{H}_F(t) |\Phi_\alpha(t)\rangle = \Omega_\alpha |\Phi_\alpha(t)\rangle, \quad (2.21)$$

where the Floquet Hamiltonian is defined as

$$\hat{H}_F(t) = \hat{H}(t) - i\hbar \frac{\partial}{\partial t}. \quad (2.22)$$

This shows that Floquet states play the same role for periodic, time-dependent systems as stationary states do for autonomous systems.

An arbitrary state can be expanded using the Floquet states,

$$\begin{aligned}
|\Psi(t)\rangle &= \sum_{\alpha} A_{\alpha} |\Psi_{\alpha}(t)\rangle \\
&= \sum_{\alpha} A_{\alpha} e^{-i\frac{\Omega_{\alpha}t}{\hbar}} |\Phi_{\alpha}(t)\rangle \\
&= \sum_{\alpha} e^{-i\frac{\Omega_{\alpha}t}{\hbar}} |\Phi_{\alpha}(t)\rangle \langle \Phi_{\alpha}(0) | \Psi(0) \rangle, \tag{2.23}
\end{aligned}$$

since the Floquet states are orthonormal, $\langle \Phi_{\alpha}(t) | \Phi_{\beta}(t) \rangle = \delta_{\alpha\beta}$. The quasienergies and Floquet states are calculated from the Floquet matrix. This matrix is constructed from states that have been propagated forward in time by one period,

$$\begin{aligned}
|\Psi(T)\rangle &= \sum_{\alpha} e^{-i\frac{\Omega_{\alpha}T}{\hbar}} |\Phi_{\alpha}(0)\rangle \langle \Phi_{\alpha}(0) | \Psi(0) \rangle \\
&= \hat{U}(T) |\Psi(0)\rangle \\
&= e^{-i\int_0^T \hat{H}(\tau) d\tau} |\Psi(0)\rangle, \tag{2.24}
\end{aligned}$$

where $\hat{U}(T)$ is the Floquet operator, the unitary operator which propagates a state forward in time by one period. By inspection of Eq. 2.24, it can be seen that the Floquet states at $t = 0$ are the eigenvectors of the operator while the eigenvalues are $e^{-i\Omega_{\alpha}T/\hbar}$.

The Floquet matrix, $U_{mn}(t)$, is constructed using the unperturbed eigenstates of the Hamiltonian, \hat{H}_0 . The matrix elements, $\langle m | \hat{U} | n \rangle$, can be interpreted as the components of $\hat{U} | n \rangle$, which is the basis state $|n\rangle$ after one period. Therefore, evolving $|n\rangle$ by one period for each n gives each column of the matrix in turn.

The evolution of the basis states can be accomplished in a number of ways. First, direct integration of the Schrodinger equation is the simplest method. The split-operator method [21, 22] is an alternative way to propagate the states. It is a less expensive way of running larger problems. If a small enough time interval is used,

$$|\Psi(t + \delta t)\rangle \simeq e^{-i\hat{H}(t)\delta t} |\Psi(t)\rangle. \quad (2.25)$$

For a general Hamiltonian, $\hat{H}(t) = \hat{p}^2/2 + V(\hat{x}, t)$, the propagator can be split [43],

$$e^{-i(\hat{p}^2/2 + V(\hat{x}, t))\delta t} = e^{-i\hat{p}^2\delta t/4} e^{-iV(\hat{x}, t)\delta t} e^{-i\hat{p}^2\delta t/4} + \mathcal{O}(\delta t^3), \quad (2.26)$$

where each exponential operates on a state that is either in the position or momentum basis. In between each operation, the state is Fourier transformed using a Fast Fourier Transform (FFT) to the other basis.

After obtaining the Floquet matrix, the eigenvalues and eigenvectors need to be determined. The Floquet quasienergies can then be calculated from the eigenvalues and plotted as a function of the perturbation amplitude. The resulting quasienergy spectrum has a Brillouin zone structure [11],

$$|\Phi_{\alpha\beta}(t)\rangle = e^{-i\beta\omega t} |\Phi_{\alpha 0}(t)\rangle, \quad (2.27)$$

$$\Omega_{\alpha\beta} = \Omega_{\alpha 0} + \hbar\omega\beta,$$

where $\omega = 2\pi/T$. The quantum numbers α label the physical state, while the integers β pick out individual representatives. The first Brillouin zone

has quasienergies, $-\hbar\omega/2 \leq \Omega_\alpha < +\hbar\omega/2$. Each set of quasienergies labeled by α corresponds to a single Floquet eigenvector. One way of visualizing the eigenvectors is with Husimi plots.

2.3.3 Husimi Plots

The Husimi representation is a way to visual quantum states. It's a quantum distribution function that allows direct comparison with classical phase space distributions [31, 64]. It has often been used to study quantum chaotic systems [13, 14, 32, 59, 65]. A coherent state is a minimum uncertainty wavepacket centered at a point (q_0, p_0) which is used to construct a family of states where the coordinate values range over all of the phase space of interest. In the momentum basis, the state becomes [15],

$$\langle p | \Phi_{p_0, q_0} \rangle = \left(\frac{\sigma^2}{\pi \hbar^2} \right)^{1/4} \exp \left[-\frac{\sigma^2 (p - p_0)^2}{2\hbar^2} - i \frac{(p - p_0) q_0}{\hbar} \right]. \quad (2.28)$$

Alternatively, the position representation is

$$\langle q | \Phi_{p_0, q_0} \rangle = \left(\frac{1}{\sigma^2 \pi} \right)^{1/4} \exp \left[-\frac{(q - q_0)^2}{2\sigma^2} + \frac{i (q - q_0) p_0}{\hbar} \right]. \quad (2.29)$$

The expectation values shows that the state is indeed centered on q_0 and p_0 ,

$$\begin{aligned} \langle \Phi_{p_0, q_0} | \hat{p} | \Phi_{p_0, q_0} \rangle &= p_0 \\ \langle \Phi_{p_0, q_0} | \hat{q} | \Phi_{p_0, q_0} \rangle &= q_0. \end{aligned} \quad (2.30)$$

The Husimi function [50] uses the minimum uncertainty wavepacket and is given by

$$W_\Phi(p_0, q_0) = \frac{1}{2\pi\hbar} |\langle \Phi_{p_0 q_0} | \Psi \rangle|^2. \quad (2.31)$$

This function can be thought of either as a Gaussian smoothing of the Wigner Function, or a projection of a state into a Gaussian. [46] This function gives the probability that a particle lies within an area \hbar that is centered on (q_0, p_0) .

2.4 Hamiltonians in Atom Optics

In atom optics, the experimentalists create a standing wave which they then use to interact with atoms. The standing wave is often changed in some way to get the desired interaction. For the dynamic tunneling experiments, both the NIST group and the Texas group did an amplitude modulation of the laser standing wave.

The easiest way to represent the laser interaction is to separate the potential into a series of sinusoidal waves. Depending on the placement of the waves and in particular, the symmetry of the system, computation can proceed in a straight forward way.

The most general system that I've needed to use is

$$\hat{H} = \hat{n}^2 + \sum_{j=0}^N \nu_j A_j \cos \left(r_j \hat{\theta} + s_j \omega t \right), \quad (2.32)$$

where $\nu = \pm 1$, r_j and s_j are integers. If the Hamiltonian is symmetric in momentum space, then the energy basis should be used, else the momentum basis is adequate. The energy basis has definite parity which is used to overcome computational problems when near-degeneracies occur.

In the momentum basis $|n\rangle$, the Schrödinger equation, with $\hbar = 1$,

becomes

$$\begin{aligned}
i \frac{\partial}{\partial t} \langle n | \Psi \rangle &= n^2 \langle n | \Psi \rangle + \langle n | \widehat{V} | \Psi \rangle \\
&= n^2 \langle n | \Psi \rangle + \sum_{j=0}^N \frac{\nu_j A_j}{2} \left(e^{is_j \omega t} \langle n - r_j | \Psi \rangle + e^{-is_j \omega t} \langle n + r_j | \Psi \rangle \right).
\end{aligned} \tag{2.33}$$

The energy basis, $|E_k\rangle = |k\rangle$, is

$$\langle x | E_k \rangle = \begin{cases} \frac{1}{\sqrt{\pi}} \cos(kx), & \text{if } k > 0; \\ \frac{1}{\sqrt{2\pi}}, & \text{if } k = 0; \\ \frac{1}{\sqrt{\pi}} \sin(-kx), & \text{if } k < 0. \end{cases}$$

In the energy basis, the Schrödinger equation, with $\hbar = 1$, becomes

$$i \frac{\partial}{\partial t} \langle k | \Psi \rangle = E_k \langle k | \Psi \rangle + \langle k | \widehat{V} | \Psi \rangle. \tag{2.34}$$

Evaluating the potential depends upon the sign of k ,

$$\langle k | \widehat{V} | \Psi \rangle = \sum_{j=0}^N \frac{\nu_j A_j}{2} \begin{cases} \frac{1}{\sqrt{2}} e^{is_j \omega t} (\langle k - r_j | \Psi \rangle + \langle -k - r_j | \Psi \rangle) \\ + \frac{1}{\sqrt{2}} e^{-is_j \omega t} (\langle k + r_j | \Psi \rangle + \langle r_j - k | \Psi \rangle), \\ e^{is_j \omega t} \langle -r_j | \Psi \rangle + e^{-is_j \omega t} \langle r_j | \Psi \rangle, \\ \frac{1}{\sqrt{2}} e^{is_j \omega t} (\langle k - r_j | \Psi \rangle + \langle -k - r_j | \Psi \rangle) - \frac{1}{\sqrt{2}} e^{-is_j \omega t} (\langle k + r_j | \Psi \rangle + \langle r_j - k | \Psi \rangle) \end{cases}$$

2.4.1 Pendulum

The pendulum obtains from the general case by setting, $A_0 = A$, $\nu_0 = 1$, $r_0 = k$, and all other parameters equal to zero,

$$\widehat{H} = \widehat{n}^2 + A \cos k\widehat{\theta}. \tag{2.35}$$

As the amplitude of the cosine, A , increases, the energy eigenvalues also change. Changing the scale of the parameters to match the discussion in

Abramowitz and Stegun of Mathieu functions [1], the eigenvalues are given in Fig. 2.14. This plot is important because it is so similar to the quasienergy

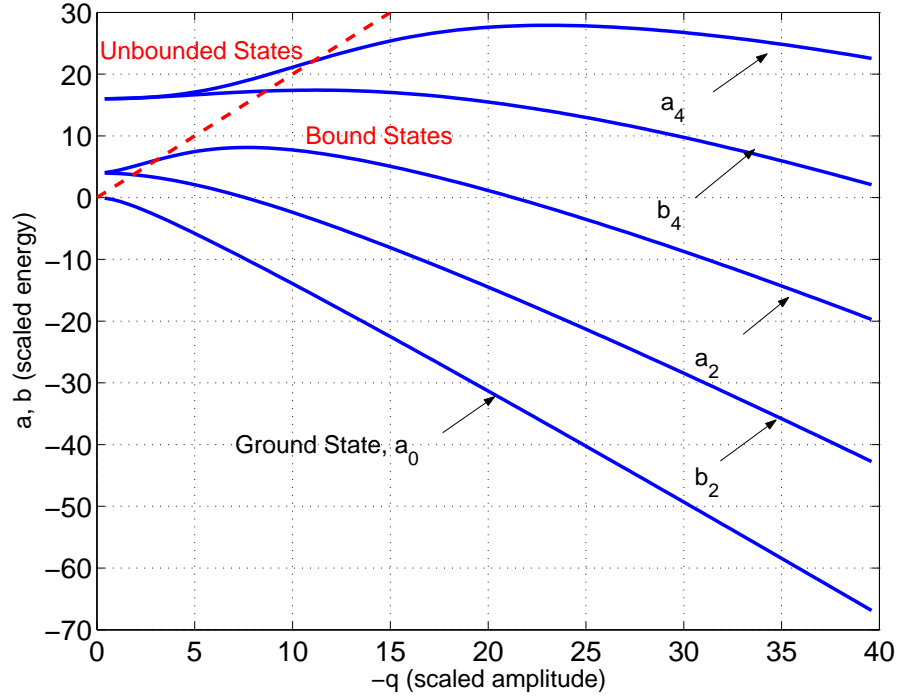


Figure 2.14: Energy eigenvalues of the quantum pendulum. The red dotted line separates the states which have energies less than the peak of the pendulum potential from those that have positive kinetic energy at all times. The notation is given in Abramowitz and Stegun.

plots obtained from the eigenvalues of the Floquet matrix for the atom optics experiments discussed in subsequent chapters. In particular, the distinctive downward shape of the ground state curve is present whenever a Floquet state is sitting on a resonance. The higher energy curves will also be recognized in these Floquet quasienergy plots.

In Fig. 2.15, the first four eigenstates are shown in Husimi plots. These plots also resemble the Husimi plots for the Floquet states which are calculated from the atom optics Hamiltonians in the subsequent chapters. The

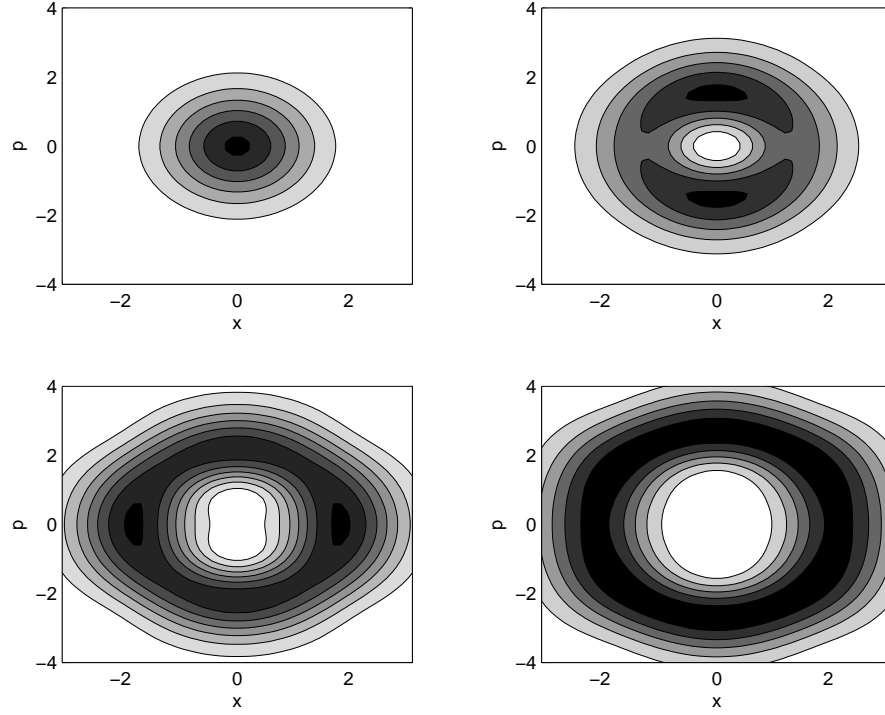


Figure 2.15: Husimi functions of the first four eigenvectors of the quantum pendulum for an amplitude of $A = 2.5$. (a) state 1, (b) state 2, (c) state 3, (d) state 4.

states start off by remaining within the oscillatory region of the pendulum. Eventually, the states occupy the rotation region, as seen in Fig. 2.16.

As a result of this close comparison between the eigenvalues and eigenvectors of the pendulum and the Floquet quasienergies and eigenstates, it must be concluded that resonances can be modeled as pendulum structures. This is

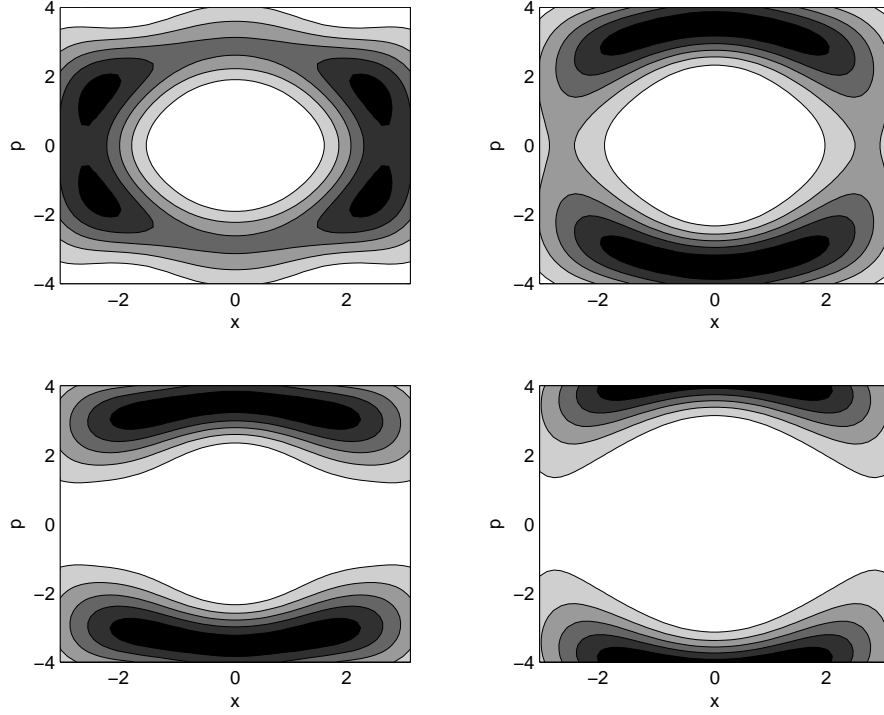


Figure 2.16: Husimi functions of eigenvectors 5-8 of the quantum pendulum for an amplitude of $A = 2.5$. (a) state 5, (b) state 6, (c) state 7, (d) state 8.

nothing new. It is indeed the easiest way to decide when the onset of chaos will occur, by calculating the width of a pendulum and seeing if it overlaps with another resonance. The nice thing is that we now have a tool for interpreting the Floquet states for various atom optics experiments.

2.5 Dynamic Tunneling

There are two ways to visualize the dynamic tunneling of the atomic optics experiments in this dissertation. Each of these viewpoints corresponds

to a different form of the Hamiltonian potential. The potential is written with either a single sinusoidal function of the position variable or as a sum of moving sinusoidal waves.

2.5.1 Modulated Potential Well View

The first viewpoint is that of a standing wave potential that has an amplitude modulation applied to it. This closely follows the actual way that the experiments are conducted. The Texas Hamiltonian has the form

$$V(\phi) = -2V_0 \cos^2\left(\frac{\omega_m t}{2}\right) \cos(\phi), \quad (2.36)$$

where ω_m is the modulation frequency. The modulation causes the amplitude to oscillate between $2V_0$ and 0. As a result, if the magnitude of the initial momentum is large enough, a resonance can be obtained by having the atom repeat its momentum from one well in the next well after one modulation period, as shown in Fig. 2.17.

So each time the atom reaches the bottom of a well, it has the same momentum as it had in the bottom of each of the previous wells. Both the strobe plots and the experiments measure the momentum of the atom at time intervals of the modulation period. The strobe plot will result in a single point for this resonance. Classically, periodic measurements of the momentum, when the atom is at the bottom of the well, will always result in the same momentum for an atom that is in resonance with the potential. However, if quantum dynamic tunneling occurs, then after a certain number of modulation periods,

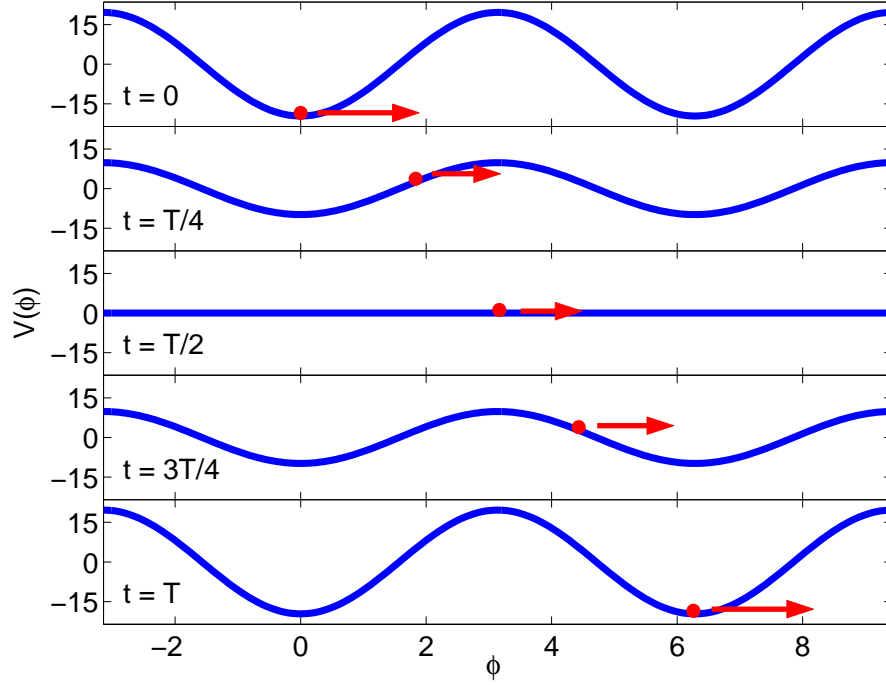


Figure 2.17: Modulated potential viewpoint of dynamic tunneling for the Texas Hamiltonian.

the measured momentum will be in the opposite direction. The initial state has tunneled into a second state with a momentum direction that is opposite of what the initial state had.

The NIST experiment has a Hamiltonian with the form

$$V(\phi) = 2\kappa(1 + 2\varepsilon \sin \omega_m t) \sin^2(\phi), \quad (2.37)$$

where κ and ε are amplitude parameters that can be varied experimentally. This potential is shown in Fig. 2.18. Note that the modulation never causes the potential to go to zero if $\varepsilon < 1/2$. Thus, a resonance can occur with the atom

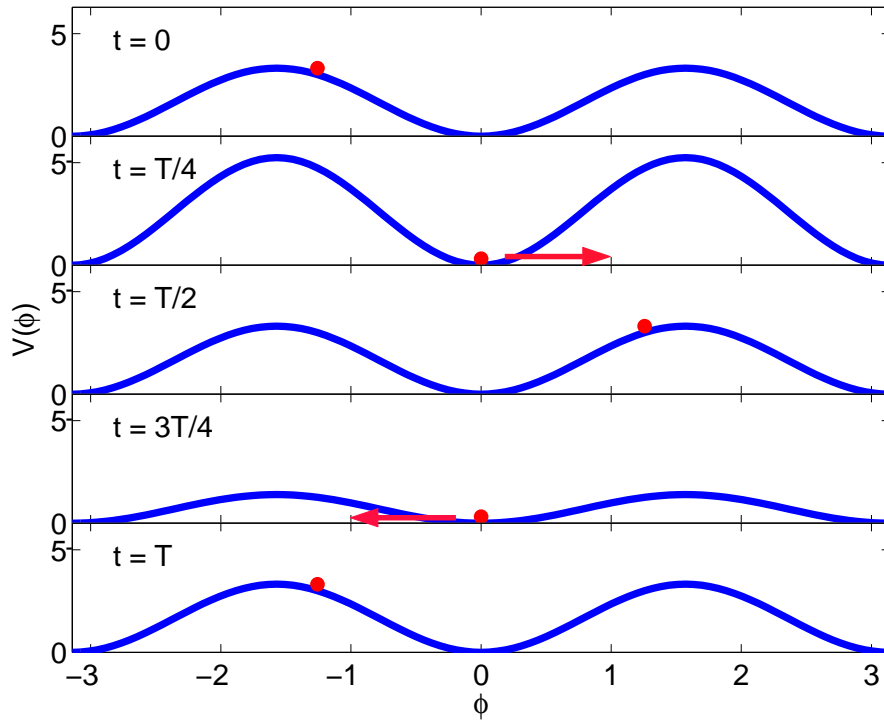


Figure 2.18: Modulated potential viewpoint of dynamic tunneling for the NIST Hamiltonian.

oscillating within a single potential well. If the experimental measurements start at $t = T/4$ and continue at intervals of the modulation period, classically, the momentum will always be the same for an atom in resonance with the potential. Again, if dynamic tunneling occurs, then after a number of periods, the measured momentum will be in the opposite direction.

With both the Texas and NIST potentials, the momentum is measured at multiples of the modulation period. Classically, the momentum must continue to be in the same direction when it is measured periodically. In both

experiments, the measured momentum eventually switches to the opposite direction. Since this is not possible from a classical perspective, it must be the result of quantum tunneling.

2.5.2 Moving Lattice View

An alternative viewpoint of the dynamic tunneling comes from restructuring the Hamiltonian potential using trigonometric identities,

$$V_0(\phi) = A \cos \phi + B \cos(\phi - \omega_m t) + B \cos(\phi + \omega_m t). \quad (2.38)$$

Although the NIST potential has some extra terms, both systems have these three common functions of the position coordinate. Thus, the potential consists of a stationary lattice and two lattices traveling in opposite directions with the same momentum magnitude. These moving lattices are shown in Fig. 2.19. An atom can be pictured as being located at the bottom of one of the wells of one of the moving lattices. The atom has the same momentum as the lattice. When dynamic tunneling occurs, the atom tunnels into the opposite traveling lattice and obtains its momentum.

This viewpoint fits nicely with the strobe plots. Each of the strobe plots have pairs of resonances at positive and negative momentum values. These resonances can be thought of as the two moving lattices. When an atom has an initial state in one of the resonance islands, it is equivalent to being in the corresponding lattice.

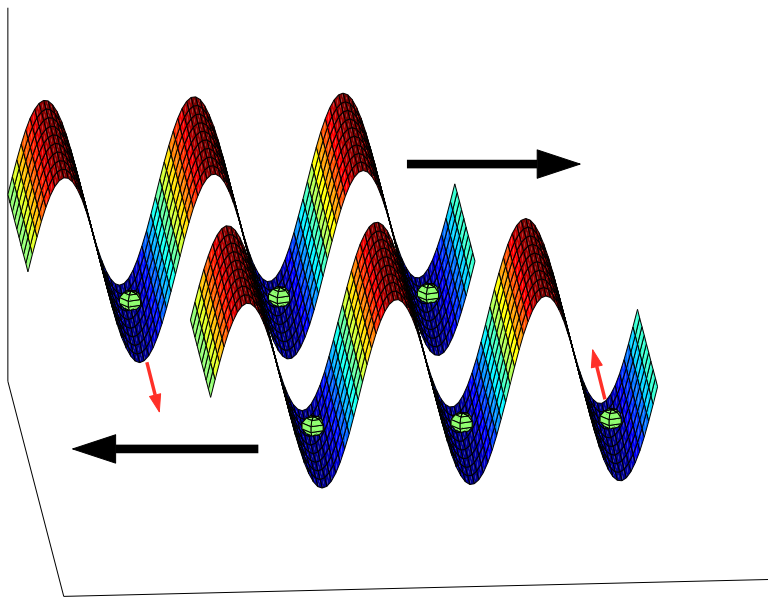


Figure 2.19: Moving lattice viewpoint of dynamic tunneling.

Chapter 3

Texas Experiment

3.1 Experiment Hamiltonian

3.1.1 System Model

The Texas experiment uses laser-cooled trapped cesium atoms [53, 63]. The ultracold atoms are in a magneto-optical cell trap (MOT) ???. For laser cooling, the laser must be tuned slightly to the red of an atomic transition. In the cesium experiments, the laser drove the $F = 4 \longrightarrow F' = 5$ hyperfine component of the D_2 transition. The MOT uses six laser beams in three orthogonal directions to control the atoms in a vacuum chamber. The atoms are trapped using Helmholtz gradient coils which position the atoms at the center of the MOT. A gaussian distribution of position ($\sigma_x = 0.15\text{mm}$) and momentum ($\sigma_p = 8\hbar k_L$) results. Just before the standing wave interaction, the atoms are optically pumped to the ground state. The sample is dilute enough that atom-atom interactions are negligible. This results in an ensemble of single-atom experiments.

The optical lattice that interacted with the atoms was provided by a high-intensity, far-detuned Ti:sapphire laser. The laser produced single-mode light that was tunable for several nm around 852nm. In particular, the atoms sit in a standing wave produced by the interference between a laser beam

and its reflection which is propagating in the opposite direction. The counter-propagating beams are focused to a large waist of 1.5mm, which is significantly larger than the size of the MOT atom cloud. The laser is near-resonant at ω_L . However, the excited state amplitude is adiabatically eliminated with a sufficiently large detuning, $\delta_L = \omega_0 - \omega_L$, where $\hbar\omega_0$ is the energy difference between excited state $|e\rangle$ and the ground state $|g\rangle$ of the two-level atoms. An acousto-optic modulator (AOM) allows the experimenters to control the intensity of the laser and put a time dependent factor into the system Hamiltonian.

Momentum measurements by the experimentalists are made by allowing the atoms to drift for controlled time periods by turning off all lasers and gradient coils. To stop the motion, an optical molasses is formed by turning on the MOT lasers.

There are two interactions between the atoms and the laser. The first is the incoherent radiation pressure force. This force is due to the stimulated absorption of photons. It occurs along the direction of the beam due to the absorption of a photon from the laser beam which results in an atom recoil of $m\Delta v = \hbar k_L$. For cesium, the recoil velocity is $\Delta v = 4.4\text{cm/sec}$. If the atoms are already in the excited upper state, they will spontaneously emit a photon with the atom recoil from this emission in a random direction.

The second interaction is the coherent dipole force. This is stimulated absorption followed by stimulated emission via a virtual state. A polarized atom experiences a force in the gradient field of a laser. The resulting atom recoil is $2\hbar k_L$. This recoil results from an atom absorbing a photon from one

beam and emitting a photon into the opposite beam. For far detuned light, this process dominates spontaneous emission. In the theoretical Hamiltonian in this thesis, I will do a canonical transformation that explicitly uses this two photon recoil.

3.1.2 Hamiltonian Derivation

Semiclassical theory is used for the atom-field interaction. The atom is treated as a two-level system and the optical field is treated classically. As long as the two levels are nearly resonant with the driving field and the other levels are highly detuned, the two-level atom can be coupled with a single mode of the electromagnetic field.

The Hamiltonian for the interaction of a single two-level atom with a single-mode field can be divided into two parts

$$\hat{H} = \hat{H}_0 + \hat{H}_1, \quad (3.1)$$

where \hat{H}_0 is the unperturbed part and \hat{H}_1 is the interaction part [57]. Using the eigenvalue equation $\hat{H}_0 |a\rangle = \hbar\omega_a |a\rangle$ and the completeness relation $|e\rangle\langle e| + |g\rangle\langle g| = \mathbf{1}$, the unperturbed part becomes

$$\hat{H}_0 = (|e\rangle\langle e| + |g\rangle\langle g|) \hat{H}_0 (|e\rangle\langle e| + |g\rangle\langle g|) \quad (3.2)$$

$$= \hbar\omega_e |e\rangle\langle e| + \hbar\omega_g |g\rangle\langle g| \quad (3.3)$$

$$= \hbar\omega_0 |e\rangle\langle e|, \quad (3.4)$$

where ω_g has been set to zero and $\omega_e = \omega_0$ is the atomic transition frequency for cesium.

The interaction part of the Hamiltonian, for an electric field given by $E(t) = E_0 \cos \omega_L t$, can be calculated using the dipole approximation

$$\hat{H}_1 = -exE(t) \quad (3.5)$$

$$= -e(|e\rangle\langle e| + |g\rangle\langle g|)x(|e\rangle\langle e| + |g\rangle\langle g|)E_0 \cos \omega_L t \quad (3.6)$$

$$= -(d|e\rangle\langle g| + d^*|g\rangle\langle e|)E_0 \cos \omega_L t \quad (3.7)$$

where $d = e\langle e|x|g\rangle$ is the matrix element of the dipole moment. This expression can be simplified[41] by using the rotating wave approximation

$$\hat{H}_1 = -\left(\frac{dE_0}{2}|e\rangle\langle g| + \frac{d^*E_0}{2}|g\rangle\langle e|\right)(e^{i\omega_L t} + e^{-i\omega_L t}) \quad (3.8)$$

$$\approx -\left(\frac{dE_0}{2}e^{-i\omega_L t}|e\rangle\langle g| + \frac{d^*E_0}{2}e^{i\omega_L t}|g\rangle\langle e|\right) \quad (3.9)$$

$$= -\frac{\hbar\Omega_R}{2}e^{-i\omega_L t}|e\rangle\langle g| - \frac{\hbar\Omega_R^*}{2}e^{i\omega_L t}|g\rangle\langle e|, \quad (3.10)$$

where $\Omega_R = \frac{dE_0}{\hbar}$ is the Rabi frequency. In this expression, terms that will ultimately yield exponentials with $\omega_0 + \omega_L$ are dropped.

For the Texas experiments, the electric field is more complicated than the one used above. The electric field [53] for two counterpropagating beams becomes a standing wave along the x-axis with polarization along the y-axis

$$\vec{E}(x, t) = \hat{y}E_0 \cos(\omega_L t + k_L x) + \hat{y}E_0 \cos(\omega_L t - k_L x) \quad (3.11)$$

$$= \hat{y}E_0 \cos(k_L x) (e^{-i\omega_L t} + e^{i\omega_L t}). \quad (3.12)$$

The interaction Hamiltonian now becomes

$$\hat{H}_1 \approx -dE_0 \cos(k_L x) e^{-i\omega_L t} |e\rangle\langle g| - d^*E_0 \cos(k_L x) e^{i\omega_L t} |g\rangle\langle e| \quad (3.13)$$

$$= -dE_0 \cos(k_L x) e^{-i\omega_L t} \sigma_+ - d^*E_0 \cos(k_L x) e^{i\omega_L t} \sigma_-, \quad (3.14)$$

where σ_{\pm} are Pauli spin-flip operators. For example,

$$\sigma_+ = |e\rangle \langle g| = \begin{pmatrix} 1 \\ 0 \end{pmatrix} \begin{pmatrix} 0 & 1 \end{pmatrix} = \begin{pmatrix} 0 & 1 \\ 0 & 0 \end{pmatrix}. \quad (3.15)$$

Finally, after adding the kinetic energy of the atom, the total Hamiltonian becomes [24]

$$\hat{H} = \frac{\hat{p}^2}{2m} + \hbar\omega_0 |e\rangle \langle e| - (dE_0 \cos(k_L \hat{x}) e^{-i\omega_L t} \sigma_+ + H.c.), \quad (3.16)$$

where \hat{p} is the center-of-mass momentum of the atoms. As stated above, the dipole and rotating wave approximations were used to derive this equation.

The wave function for the atomic state can be represented as

$$\Psi(x, t) = \Psi_g(x, t) |g\rangle + \Psi_e(x, t) e^{-i\omega_L t} |e\rangle. \quad (3.17)$$

Substituting the wave function into the time-dependent Schrödinger's equation and then multiplying by $\langle g|$ and $\langle e|$ in turn, yields

$$i\hbar \frac{\partial \Psi_g}{\partial t} = -\frac{\hbar^2}{2m} \frac{\partial^2 \Psi_g}{\partial x^2} - d^* E_0 \cos(k_L x) \Psi_e \quad (3.18)$$

$$i\hbar \frac{\partial \Psi_e}{\partial t} = -\frac{\hbar^2}{2m} \frac{\partial^2 \Psi_e}{\partial x^2} + \hbar(\omega_0 - \omega_L) \Psi_e - dE_0 \cos(k_L x) \Psi_g. \quad (3.19)$$

Cleaning up these coupled equations, we get

$$i\hbar \frac{\partial \Psi_g}{\partial t} = -\frac{\hbar^2}{2m} \frac{\partial^2 \Psi_g}{\partial x^2} - \frac{\hbar\Omega^*}{2} \cos(k_L x) \Psi_e \quad (3.20)$$

$$i\hbar \frac{\partial \Psi_e}{\partial t} = -\frac{\hbar^2}{2m} \frac{\partial^2 \Psi_e}{\partial x^2} + \hbar\delta_L \Psi_e - \frac{\hbar\Omega}{2} \cos(k_L x) \Psi_g, \quad (3.21)$$

where $\Omega/2 = \frac{dE_0}{\hbar} = \Omega_R$ is the Rabi frequency, E_0 is the electric field strength, d is the dipole moment of cesium, and $\delta_L = \omega_0 - \omega_L$ is the detuning.

By having a high detuning, spontaneous emission from the upper level can be neglected. Adiabatic elimination is achieved by setting the derivatives of Ψ_e equal to zero. This results in a relation between the excited and ground states

$$\Psi_e = \frac{\Omega}{2\delta_L} \cos(k_L x) \Psi_g. \quad (3.22)$$

Substituting this relation into the remaining equation of motion gives

$$i\hbar \frac{\partial \Psi_g}{\partial t} = -\frac{\hbar^2}{2m} \frac{\partial^2 \Psi_g}{\partial x^2} - \frac{\hbar\Omega^2}{4\delta_L} \cos^2(k_L x) \Psi_g. \quad (3.23)$$

Extracting the Hamiltonian from the uncoupled Schrödinger equation, gives

$$\hat{H} = \frac{\hat{p}^2}{2m} - \frac{\hbar\Omega_{eff}}{4} \cos^2(k_L \hat{x}), \quad (3.24)$$

where $\Omega_{eff} = \frac{\Omega^2}{\delta_L}$ is the ac-Stark shift. By neglecting a constant potential, we get the final form for an atom in a standing wave

$$\hat{H} = \frac{\hat{p}^2}{2m} - \frac{\hbar\Omega_{eff}}{8} \cos(2k_L \hat{x}). \quad (3.25)$$

The experimentalists have the ability to modulate the standing wave with various time dependent functions [53]

$$\hat{H} = \frac{\hat{p}^2}{2m} - \frac{\hbar\Omega_{eff}}{8} f(t) \cos(2k_L \hat{x}). \quad (3.26)$$

The modulation for the experiments which produced dynamic tunneling yields a time-dependent Hamiltonian

$$\hat{H} = \frac{\hat{p}^2}{2m} - 2V_0 \cos^2\left(\frac{\omega_m t}{2}\right) \cos(2k_L \hat{x}), \quad (3.27)$$

where $V_0 = \hbar\Omega_{eff}/8 = \hbar\Omega^2/8\delta_L$ and $\omega_m = 2\pi/T_m$ is the modulation frequency.

3.1.3 Hamiltonian Scaling

The Hamiltonian in the experimental scaled units [60, 61] is

$$\hat{H}_{exp} = \frac{\hat{\rho}^2}{2} - 2\alpha \cos^2(\pi\tau) \cos(\hat{\phi}), \quad (3.28)$$

where the time is $\tau = \omega_m t / 2\pi = t / T_m$, the momentum operator is $\hat{\rho} = 4\pi k_L \hat{p} / m\omega_m$, the position operator is $\hat{\phi} = 2k_L \hat{x}$, and the Hamiltonian is $\hat{H}_{exp} = 16\pi^2 k_L^2 \hat{H} / m\omega_m^2$. The new commutation relation becomes

$$i\hat{k} \equiv [\hat{\phi}, \hat{\rho}] \quad (3.29)$$

$$= (2k_L) \left(\frac{4\pi k_L}{m\omega_m} \right) [\hat{x}, \hat{p}] \quad (3.30)$$

$$= i8\omega_r T_m, \quad (3.31)$$

where $\omega_r = \hbar k_L^2 / 2m$ is the recoil frequency of the atom and \hat{k} is the scaled Planck constant. As a result, the scaled momentum can be written

$$\hat{\rho} = \frac{\hat{k}}{2\hbar k_L} \hat{p}, \quad (3.32)$$

which means integer multiples of \hat{k} in the scaled momentum is equivalent to integer multiples of two-photon recoils ($2\hbar k_L$) in the real momentum. In the experiments, the initial state is well localized at discrete momentum states separated by $2\hbar k_L$. This quantization of the momentum occurs naturally in the experiment due to the presence of the counterpropagating laser beams which cause two-photon transitions.

3.2 Experimental Results

A number of experiments were done with a laser modulated at a period of $T_m = 20\mu s$ using cesium atoms with a recoil frequency of $\omega_r = 1.30 \times 10^4 \text{ rad/s}$. Originally [61], the experiments used values of α set approximately at 10.0. At this amplitude value, there are two small resonances at $\rho = \pm 4.2k$ with a chaotic sea between them. The experimentalists were able to create a localized wave packet centered at one of the two outer resonance islands. The state then oscillated between the two islands. The measured oscillation frequency was matched by the theory below. Subsequent experiments produced additional frequencies. The theory given below also predicts the existence of these multiple frequencies.

Eventually, the experimentalists varied α over a fairly wide range and made measurements of the frequencies. A distinctive plot of the oscillation frequencies as a function of α was created. This plot of the measured frequencies is matched by a theoretical plot which is produced below.

3.3 Theoretical Hamiltonian

For the theoretical analysis, a scaling is used that explicitly quantizes the moment in units of $2\hbar k_L$. This will produce scaled momentum values that are simple integers. As shown later, this scaling allows the use of Floquet theory rather than Floquet-Bloch theory which deals with a continuum of momentum states [44].

Starting with the canonical transformation $\hat{\phi} = 2k_L\hat{x}$ and $\hat{J} = \hat{p}/2k_L$, the Hamiltonian in Eq 3.27 becomes

$$\hat{H} = \frac{\hat{J}^2}{2I} - 2V_0 \cos^2\left(\frac{\omega_m t}{2}\right) \cos(\hat{\phi}) \quad (3.33)$$

$$= \frac{\hat{J}^2}{2I} - V_0 \left(\cos(\hat{\phi}) + \frac{1}{2} \cos(\hat{\phi} - \omega_m t) + \frac{1}{2} \cos(\hat{\phi} + \omega_m t) \right), \quad (3.34)$$

where $I = m/4k_L^2$ and some trig identities have been used to get the last form. Rescaling the momentum, $\hat{J} = \hat{n}\hbar$, the theoretical Hamiltonian simplifies to

$$\hat{H}_{th} = \hat{n}^2 - \frac{\alpha\omega^2}{8\pi^2} \left(\cos(\hat{\phi}) + \frac{1}{2} \cos(\hat{\phi} - \omega t') + \frac{1}{2} \cos(\hat{\phi} + \omega t') \right), \quad (3.35)$$

where $\alpha = 8\omega_r T_m^2 V_0/\hbar$ is the experimental amplitude and $\hat{H}_{th} = 2I\hat{H}/\hbar^2 = m\hat{H}/2\hbar^2 k_L^2$. The time was also rescaled, $t' = (\hbar/2I)t = 4\omega_r t$, to accommodate the change in momentum operators from \hat{J} to \hat{n} . This then caused a rescaling in the frequency, $\omega = \omega_m t/t' = 2\pi/T$, where T is the scaled period.

The final scaled momentum used in the theory is related to the original momentum by

$$\hat{n} = \frac{\hat{p}}{2\hbar k_L}. \quad (3.36)$$

This shows that \hat{n} is a dimensionless momentum operator which gives the momentum in units of $2\hbar k_L$. Since the momentum is quantized in units of this amount, the eigenvalues of \hat{n} are integer valued, $-\infty \leq n \leq \infty$, with eigenstates $|n\rangle$.

3.4 Classical Dynamics

In order to understand the quantum dynamics of this system, it is useful first to examine the structure of the underlying classical phase space. The classical motion is obtained from Hamilton's equations,

$$\dot{n} = \frac{\partial n}{\partial t'} = -\frac{\partial H_{th}}{\partial \phi} \quad (3.37)$$

$$= \frac{\alpha\omega^2}{8\pi^2} \left(\sin(\phi) + \frac{1}{2} \sin(\phi - \omega t') + \frac{1}{2} \sin(\phi + \omega t') \right) \quad (3.38)$$

$$\dot{\phi} = \frac{\partial \phi}{\partial t'} = \frac{\partial H_{th}}{\partial n} \quad (3.39)$$

$$= 2n. \quad (3.40)$$

Since Eq. 3.35 is time-periodic, the classical equations of motion will also be time-periodic. This allows Poincare surface of sections to be created by strobing the system at time intervals of the driving period, $t' = rT$, where r is a positive integer. The strobe plots at four values of α are given in Fig. 3.1. The first is at $\alpha = 2.0$ and shows the system before the resonance islands have completely overlapped. The plot in Fig. 3.1a shows three primary resonances centered at $(n = 0, \phi = 0)$ and $(n = \pm\omega/2, \phi = 0)$ which are caused by the three cosine potential wells in the Hamiltonian Eq. (3.35).

For small values of α ($\alpha < 1.5$), the primary resonances have pendulum-like structure. The half-width of a resonance is approximated by half the distance between the separatrices of a pendulum having the same amplitude as the resonance. The resonance at $n = 0$ has a half-width of $\Delta n_0 = \sqrt{\frac{\alpha\omega^2}{4\pi^2}}$, while the outer resonances at $n_{\pm} = \pm\omega/2$ have half-widths of $\Delta n_{\pm} = \Delta n_0/\sqrt{2}$ [50].

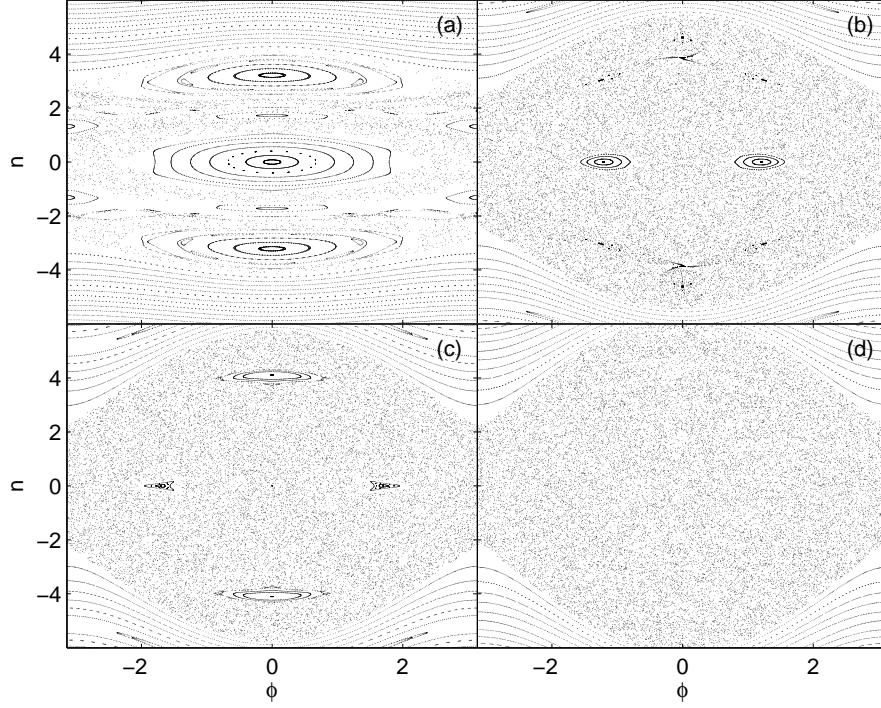


Figure 3.1: Classical strobe plots of the Texas Hamiltonian with $\omega = 6.0$ at selected potential strengths: (a) $\alpha = 2.0$, (b) $\alpha = 8.0$, (c) $\alpha = 10.0$, and (d) $\alpha = 13.0$.

The half-widths give an indication of how close the resonant islands can be before they start to overlap.

For small α and a scaled modulation frequency of $\omega = 6.0$, the outer primary islands are located at $n_{\pm} = \pm 3.0$. Even at the experimental field strength of $\alpha = 2.0$, the islands have already started to move apart and resonance overlap has started. As a result, we have a mixed phase space of KAM tori, their broken remnants, the cantori, and chaotic regions between the islands [50]. At the initial condition of the coherent state, the atoms for this

value of α are trapped by the KAM tori to the outside of the islands and by the large outer islands themselves. There shouldn't be any transport from positive to negative momentum.

As α increases, the islands eventually overlap completely and produce a phase space that is almost completely chaotic. Along the way, the central primary resonance at $n = 0$ bifurcates at $\alpha \approx 7.0$. For Fig. 3.1b, $\alpha = 8.0$ and the primary resonance at $n = 0$ can be seen to have indeed bifurcated. The two outer primaries are barely visible as small isolated islands in a chaotic sea. Note that the stochastic region is surrounded by KAM tori at higher momentum values. It can be expected that an initial condition of the coherent state that is within the chaotic sea region would now be able to move freely.

At $\alpha = 9.7$, the pendulum approximation for the half-widths of the two outer primary resonances gives $\Delta n_{\pm} = 2.1$, while the half-width of the central island is $\Delta n_0 = 3.0$. Thus the experiment is in the strong field regime since the primary resonances have overlapped. Considerable chaos is expected [50]. A surface of section of the classical phase space for $\alpha = 9.7$ is very similar to the one shown in Fig. 3.1c, where the outer islands are centered at momentum values $n = \pm 4.2$. This strobe plot also has very similar characteristics to the previous plot at $\alpha = 8.0$. The difference being that the outer islands are slightly bigger and the inner bifurcated islands have moved apart some. An initial state located near one of the outer islands should be able to move more easily through the central region with the additional separation of the bifurcated islands. Note also that the chaotic region lies in the interval $-5 \leq$

$n \leq +5$, indicating that approximately 11 quantized momentum states will ultimately determine the dynamics in the chaotic region.

The two outer primaries remain visible until $\alpha \approx 13.0$. The central primary resonance has been largely destroyed and all that is left is the chaotic sea. There is now no barrier to transport of a state from one region to another within the stochastic part of the phase space. Surprisingly, as α is increased to very high values (greater than those used experimentally), the central island eventually reappears.

Fig. 3.2 shows a strobe plot for three trajectories with $\alpha = 9.7$. These three orbits represent most of the relevant trajectories for the system. The resonance island orbit at $(\phi = 0, n = 4.1)$ is a regular orbit that is isolated from the rest of the system by additional KAM tori that surround it. Classically, an initial state placed here must remain in the neighborhood of the stable equilibrium point. The outer orbit at $(\phi = 0, n = 6.0)$ is a KAM tori that helps to bound the central chaotic sea. Initial states placed here will maintain their positive momentum for all time, but will continuously increase their position coordinate. The chaotic orbit at $(\phi = 0, n = 1.0)$ fills much of the phase space between $n = \pm 6$. It is bounded internally by the resonance islands and on the outside by KAM tori stretching across all values of ϕ . An initial state placed anywhere within the stochastic sea will take on unpredictable values of the coordinates, but remain bounded by the KAM tori on the edges of the sea.

The three trajectories have a momentum evolution as shown in Fig. 3.3. The momentum values for the outer KAM tori and the near-resonance trajec-

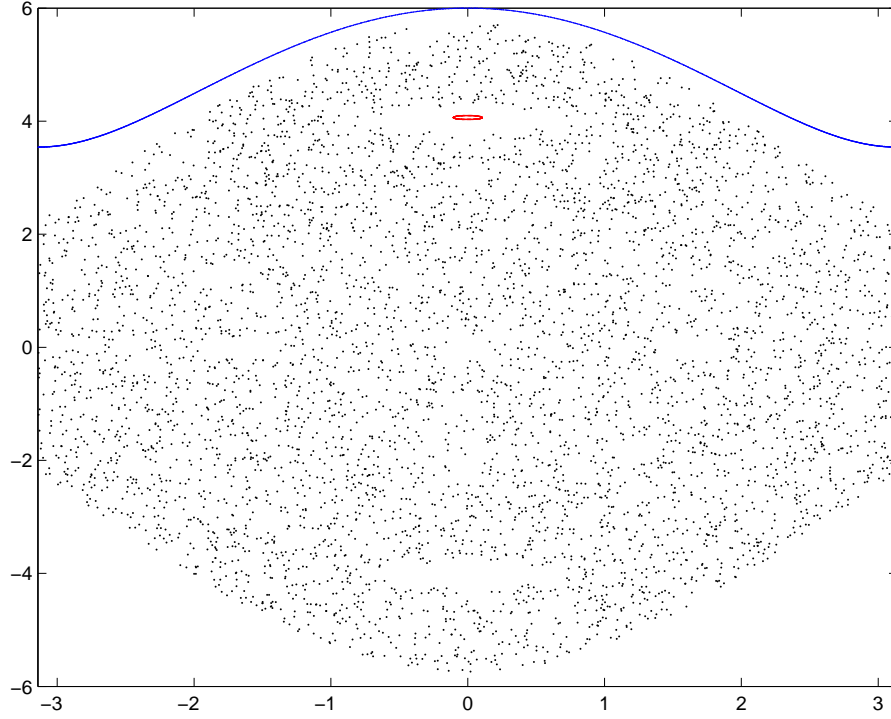


Figure 3.2: Strobe plot for three trajectories at $\alpha = 9.7$. The near-resonance regular trajectory at $(\phi = 0, n = 4.1)$ is in red. The chaotic orbit at $(\phi = 0, n = 1.0)$ is in black. The outer KAM curve at $(\phi = 0, n = 6.0)$ is in blue.

tory oscillate in time. Although their momentum oscillates, it never becomes negative. In contrast, the chaotic trajectory takes on unpredictable values of momentum, including negative values. For a trajectory to start off with positive momentum and then to later reverse itself with a negative momentum, it must be initially located somewhere in the chaotic sea. All initial states that are initially located in the regular KAM regions are effectively isolated from the negative momentum values. While this is true classically, we shall see that the quantum system does not have this restriction.

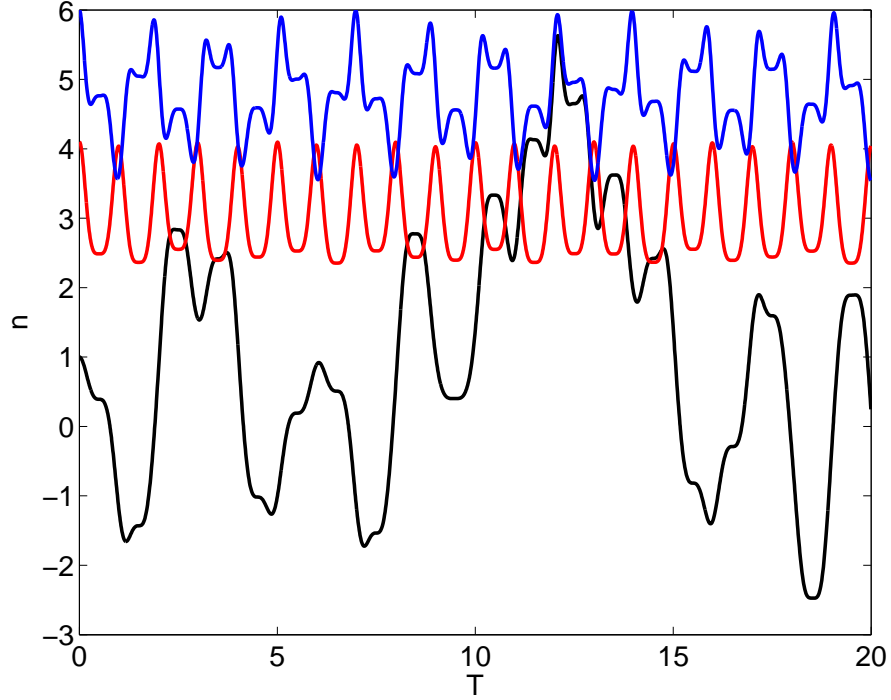


Figure 3.3: Momentum evolution for three trajectories at $\alpha = 9.7$. The near-resonance regular trajectory at $(\phi = 0, n = 4.1)$ is in red. The chaotic orbit at $(\phi = 0, n = 1.0)$ is in black. The outer KAM curve at $(\phi = 0, n = 6.0)$ is in blue.

3.5 Quantum Evolution

The experiments used atoms prepared initially with a narrow momentum distribution peaked at $n = 4.2$ (on the upper island). To numerically simulate this initial condition, we solved the Schrodinger equation,

$$i \frac{\partial |\Psi(t')\rangle}{\partial t'} = \hat{H}_{th} |\Psi(t')\rangle, \quad (3.41)$$

using momentum states, $|n\rangle$, as a basis. A coherent state,

$$\langle n | \Psi(0) \rangle \equiv \langle n | \phi_0 n_0 \rangle = \left(\frac{\sigma^2}{\pi} \right)^{\frac{1}{4}} \exp \left[\frac{-\sigma^2}{2} (n - n_0)^2 - i (n - n_0) \phi_0 \right] \quad (3.42)$$

centered at $(n = n_0, \phi = \phi_0)$ is used as the initial state, with width $\sigma = 1.2$ which was used in the experiment. In the momentum basis, the Schrodinger equation reduces to a system of coupled first order differential equations for the amplitudes, $\langle n | \Psi(t) \rangle$. This system was truncated, and 81 equations for the states $\langle n | \Psi(t) \rangle$ were kept with the momentum $-40 \leq n \leq 40$. This truncation is valid since the chaotic sea, which is the region of interest for determining the dynamics of the system, extends to a maximum momentum value of $n \leq \pm 6$ for each value of α used in the experiments and in the theory.

The time variation of the average momentum, $\langle n \rangle$, is shown in Fig. 3.4 for various values of α . Fig. 3.5 gives the corresponding power spectral density plot for each of these values of α . In all cases, the initial coherent state is located at $(n_0 = 4.2, \phi_0 = 0)$. In Fig. 3.4a, the amplitude parameter is $\alpha = 2.0$. The location of the initial state puts it slightly above the outer island, in the KAM tori region. As a result, there is only a small localized oscillation. No dynamic tunneling occurs because the KAM tori confines the state in its initial location. Note that the power spectrum for this time series is in Fig. 3.5a. It has a single dominant oscillation frequency of $f = 0$, as expected.

For the remaining the values of α in Fig. 3.4, dynamic tunneling from positive momentum to negative momentum occurs. Since the initial state is located approximately at the location of one of the outer island resonances,

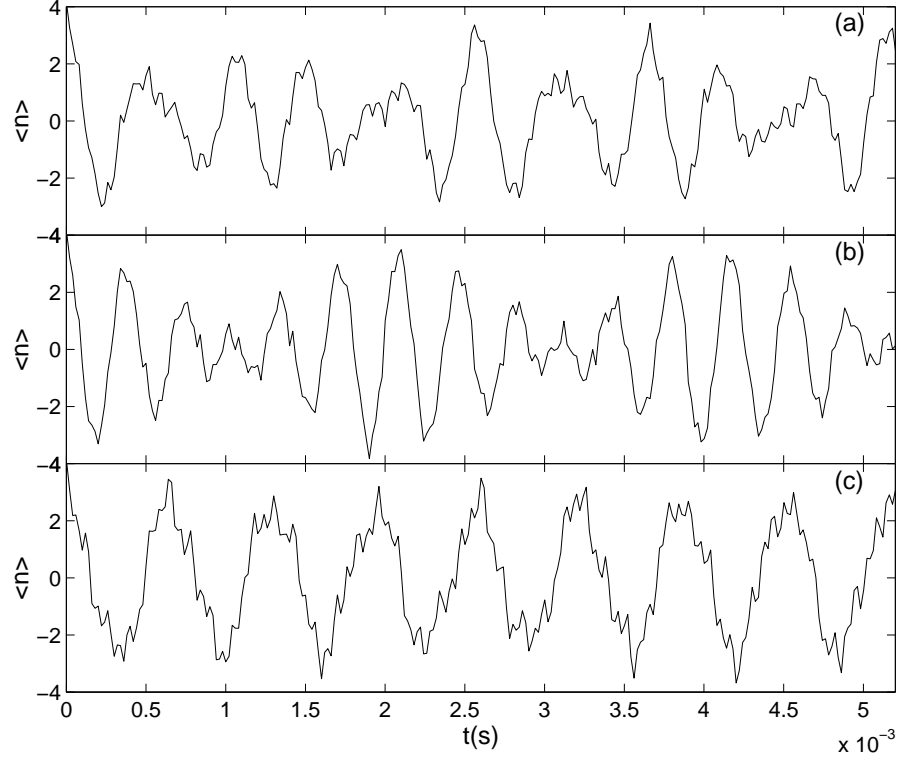


Figure 3.4: Evolution of momentum expectation value, $\langle n \rangle$ (in dimensionless units) for the Texas Hamiltonian with $\omega = 6.0$, $n_0 = 4.2$, and $\phi_0 = 0$: (a) $\alpha = 2.0$, (b) $\alpha = 8.0$, (c) $\alpha = 10.0$, (d) $\alpha = 13.0$, (e) $\alpha = 14.0$, and (f) $\alpha = 16.0$.

the observed oscillations can be considered as tunneling between classically forbidden states. The main differences between Figs. 3.4b-f (Figs. 3.5b-f) are the number of dominant frequencies. Fig. 3.5b, for $\alpha = 8.0$, shows three dominant frequencies which result in a complicated oscillation which is shown in Fig. 3.4b. The Two largest frequencies in the power spectrum are $f_1 = 1.95kHz$ and $f_2 = 2.73kHz$. The experimentalists only recorded one frequency for this value of α . The larger of the theoretical frequencies is almost exactly

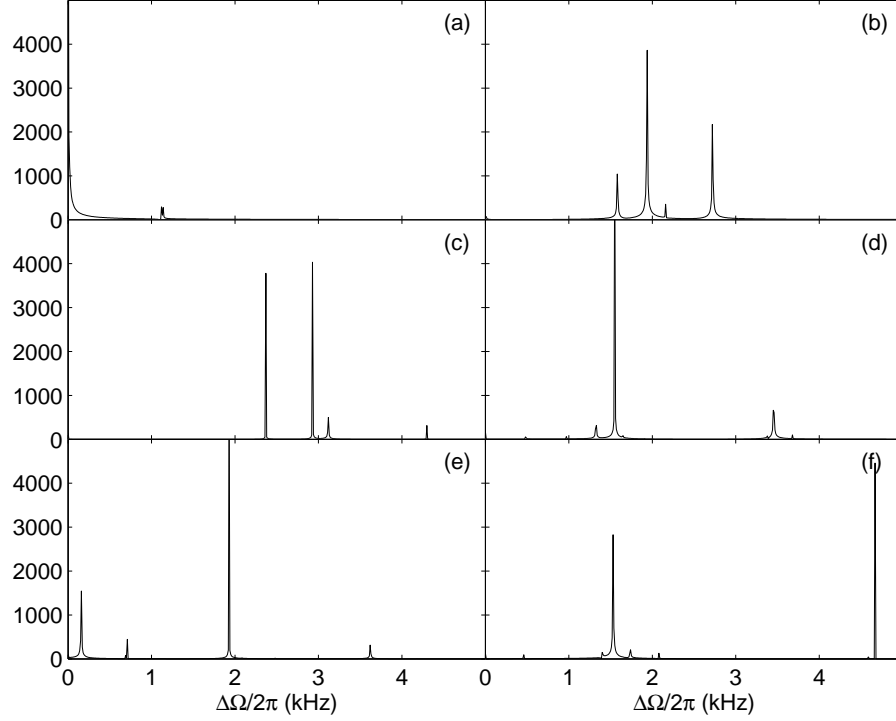


Figure 3.5: Power spectral density plots for the Texas Hamiltonian with $\omega = 6.0$, $n_0 = 4.2$, and $\phi_0 = 0$: (a) $\alpha = 2.0$, (b) $\alpha = 8.0$, (c) $\alpha = 10.0$, (d) $\alpha = 13.0$, (e) $\alpha = 14.0$, and (f) $\alpha = 16.0$.

the same as the observed experimental frequency, and it is certainly within the given experimental error bars. [62]

Two close and dominant frequencies are present at $\alpha = 10.0$ in Fig. 3.5c which results in a clear beat frequency in Fig. 3.4c. The two frequencies observed here match the two frequencies which were measured by the experimentalists. Once again, the values were well within the reported experimental error bars. These two frequencies were also the most widely separated frequen-

cies observed experimentally. It may be that when multiple frequencies are predicted by the theory for other values of α that there is a limit to how much they can be separated and still be observed experimentally. A similar analysis of time evolution with two dominant frequencies can be made for Fig. 3.5f, which is at $\alpha = 16.0$. However, these two frequencies are seen to be further apart, so the time evolution plot in Fig. 3.4f has beats which are more closely spaced than in Fig. 3.4c. The experiments cutoff just below $\alpha = 15$, so these frequencies were not observed.

A single dominant frequency occurs in Fig. 3.5d and Fig. 3.5e for $\alpha = 13.0$ and $\alpha = 14.0$, respectively. The time evolution plots in Fig. 3.4d and Fig. 3.4e show this clean single frequency oscillation. Once again, these two frequencies are in agreement with the experimentally observed frequencies within their reported error bars.

All these plots differ with experimental results on two counts. One, the amplitude of the experimental average momentum oscillations were not as great. This is probably because the experiment measures the average momentum of all the cesium atoms and not all atoms participate in the oscillations. Two, fewer frequencies were observed experimentally. The Floquet analysis which follows will give an explanation and alternate method for determining the dominant experimental frequencies.

3.6 Floquet Analysis

It is useful to examine these results using Floquet theory [50]. Floquet analysis is appropriate for this system because the Hamiltonian, \hat{H}_{th} , has time periodic coefficients. Time evolution of the initial state is controlled by the Floquet matrix. The Floquet matrix takes an initial state into a state at a time one period later.

$$|\Psi(T)\rangle = \hat{U}(T) |\Psi(0)\rangle. \quad (3.43)$$

The Floquet matrix, in the momentum basis, is an 81×81 matrix. It is constructed by taking a momentum eigenstate as the initial state and evolving it for one period, T , using the Schrodinger equation. The resulting vector is a column of the Floquet matrix in the momentum basis. Continuing this process through all the momentum eigenstates in our basis, $(-40 \leq n \leq 40)$, builds the matrix.

Once the Floquet matrix has been constructed, the Floquet eigenstates and Floquet eigenphases may be obtained by diagonalizing the Floquet matrix. The Floquet states are solutions of the Schrodinger equation which have the form

$$\langle n | \Psi(t') \rangle = e^{-i\Omega_j t'} \langle n | \chi_j(t') \rangle, \quad (3.44)$$

where Ω_j is the j^{th} Floquet eigenphase and $|\chi_j(t')\rangle$ is the j^{th} Floquet eigenstate. The Floquet eigenphases are conserved quantities, while the Floquet eigenstates are periodic in time, $|\chi_j(t')\rangle = |\chi_j(t' + T)\rangle$ and form a complete orthonormal basis [50]. As a result, Floquet states can be used to analyze the

dynamics of the system. The states, $|\chi_j(0)\rangle$, are eigenfunctions of the Floquet matrix, $\hat{U}(T)$, and the phase functions, $e^{-i\Omega_j T}$, are its eigenvalues. The Floquet matrix is computed by taking a momentum eigenstate as the initial state and evolving it for one period, T , using the Schrodinger equation. The resulting vector (in the momentum basis) is a column of the Floquet matrix.

Dynamic tunneling frequencies can be found from the differences in the Floquet eigenphases. If the initial state is a coherent state, then the state of the system $|\Psi(t')\rangle$, at time t' can be expanded in a complete set of Floquet eigenstates and has the form

$$\begin{aligned}\langle n | \Psi(t') \rangle &= \sum_j A_j \exp(-i\Omega_j t') \langle n | \chi_j(t') \rangle \\ &= \sum_j \exp(-i\Omega_j t') \langle n | \chi_j(t') \rangle \langle \chi_j(0) | \phi_0 n_0(0) \rangle\end{aligned}\quad (3.45)$$

The probability to find the system in momentum state, $|n\rangle$, at time t' , can be written

$$\begin{aligned}|\langle n | \Psi(t') \rangle|^2 &= \sum_i \sum_j \exp(-i(\Omega_j - \Omega_i)t') \langle n | \chi_j(t') \rangle \langle \chi_i(t') | n \rangle \\ &\quad \times \langle \chi_j(0) | \phi_0 n_0(0) \rangle \langle \phi_0 n_0(0) | \chi_i(0) \rangle,\end{aligned}\quad (3.46)$$

where t' is the scaled time and Ω_j is a scaled frequency. The frequencies can be rescaled by multiplying by $t'/t = 4\omega_r$ to get $\Omega_j/2\pi$ in units of Hertz.

From Eq. ??, the tunneling oscillation frequencies that are observed in the experiments, f_{exp} , can be equated to differences between Floquet eigenphases, so that $f_{exp} = (\Omega_i - \Omega_j)/2\pi$. The Floquet states that dominate the dynamics can be found from the overlap probabilities, $P_j \equiv |\langle \chi_j(0) | \phi_0 n_0(0) \rangle|^2$.

The difference between the eigenphases of the two states with the largest overlaps should produce the dominant oscillation frequency. The dominant frequencies were computed as a function of the amplitude parameter, α , with the initial state at $(n_0 = 4.2, \phi_0 = 0)$. A plot of these frequencies for the range of parameters shown in the experiment [62] was made with a threshold of $P_i P_j \geq 0.04$ and is shown in Fig. 3.6. This plot matches the experimental

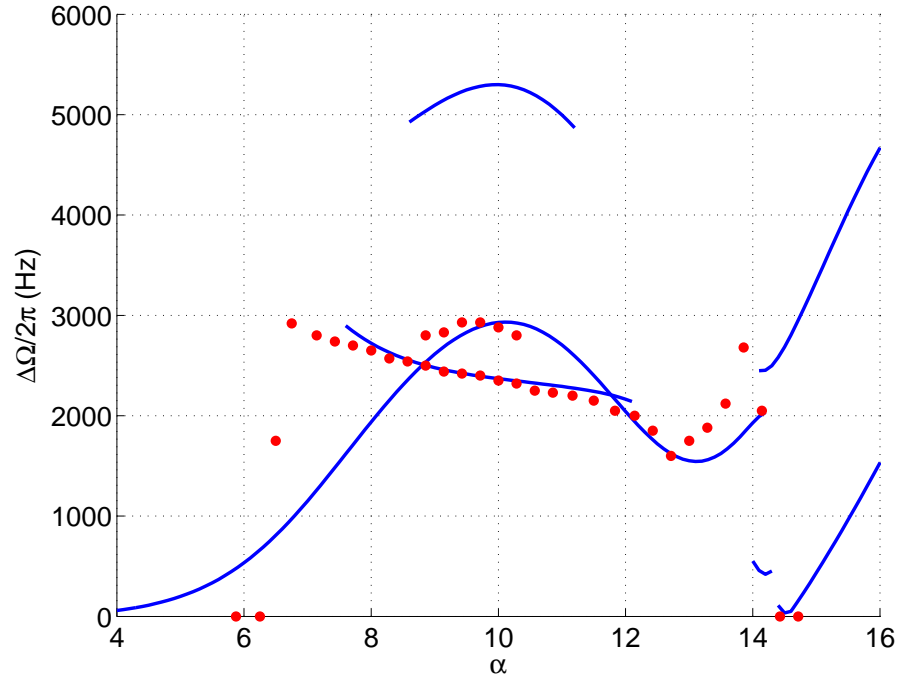


Figure 3.6: Oscillation frequencies, $\Delta\Omega = (\Omega_j - \Omega_i)$, calculated from the Floquet eigenphase differences for varying dimensionless field strengths, α . Theoretical curves are in blue, while the experimental data is plotted with red dots. A threshold of $P_i P_j \geq 0.04$ overlap probability was used to select the dominant theoretical frequencies. The three frequencies shown at $\alpha = 9.7$ correspond to $(\Omega_{3.9a} - \Omega_{3.9b})/2\pi$, $(\Omega_{3.9a} - \Omega_{3.9c})/2\pi$, and $(\Omega_{3.9b} - \Omega_{3.9c})/2\pi$.

results quite well. The frequencies also match the dominant frequencies in the power spectral density plots of Fig. 3.5.

Each curve of Fig. 3.6 is a plot of the frequency difference between two Floquet states as a function of α . At values of α where there are multiple curves there are more than two dominant eigenphase frequencies. The experiment was able to resolve the multiple dominant oscillation frequencies, $f_{exp} < 3\text{kHz}$, in the interval between $\alpha \approx 8.7$ and $\alpha \approx 10.3$ and are plotted in the figure as red dots. The theoretical analysis closely reproduces those experimental results, with each of the theoretical curves being within the experimental error bars for each value of α at which the data was taken [62]. In the amplitude range, $\alpha \approx 7.6$ to $\alpha \approx 11.6$, two oscillation frequencies dominate in the theoretical plot and give rise to the beats which are most obvious in the time evolution plot of Fig. 3.4c. In the experimental plot of the data [62], large error bars occur in the regions $\alpha \leq 7.0$ and $\alpha \geq 13.7$. This may be due to the rapid change in the dominant frequencies in those regions. A fundamental change in the dynamics occurs for $\alpha > 14$, where a different set of Floquet states begins to dominate the dynamics. The threshold of $P_i P_j \geq 0.04$ which was used to calculate the figure was selected in order to best match the experimental data. Changing the threshold will change the extent and number of the theoretical curves.

It is helpful to examine the individual Floquet eigenstates that lead to the dominant frequencies. Fig. 3.7 shows all of the Floquet eigenphases as a function of α . Most are approximately straightlines and correspond to Floquet eigenstates which lie outside the chaotic region. The eigenphases

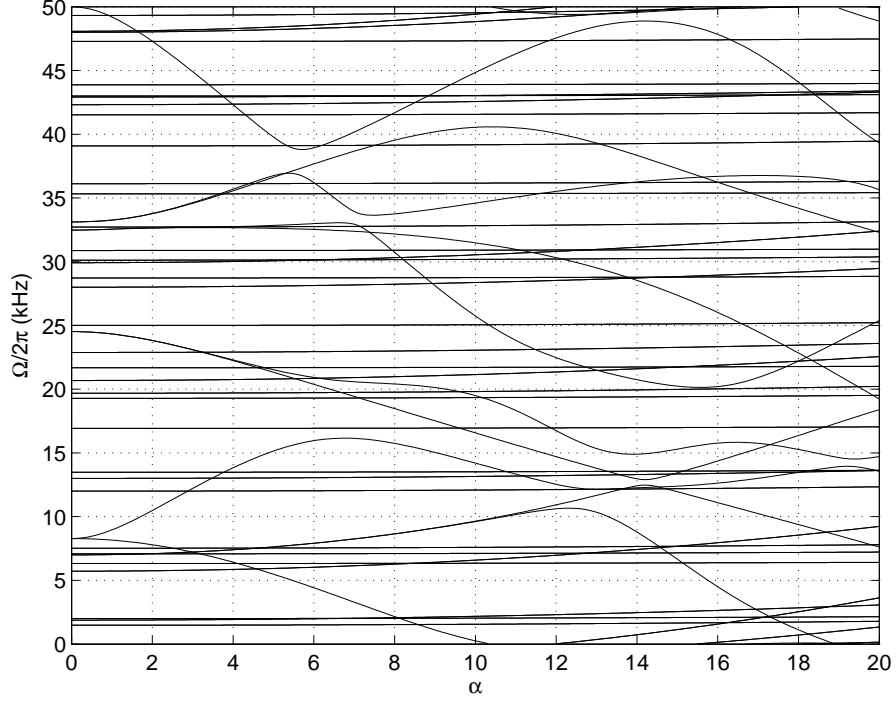


Figure 3.7: Floquet eigenphases for the Texas Hamiltonian with 81 states as a function of α .

which undergo substantial variation as a function of α lie in the chaotic region. Note that there are many avoided crossings among these states.

Fig. 3.8 shows the eigenstates with a threshold of $P_j \geq 0.17$, at various strength parameters, α . This overlap threshold was chosen to obtain the combined overlap, $P_i P_j$, that successfully matched the experimental frequencies. Each value of α in Fig. 3.8 corresponds to those in Fig. 3.4 and Fig. 3.5. Each continuous line in the figure shows the behavior of the eigenphase of a single Floquet as a function of α . Only six Floquet states are shown in Fig. 3.8, and

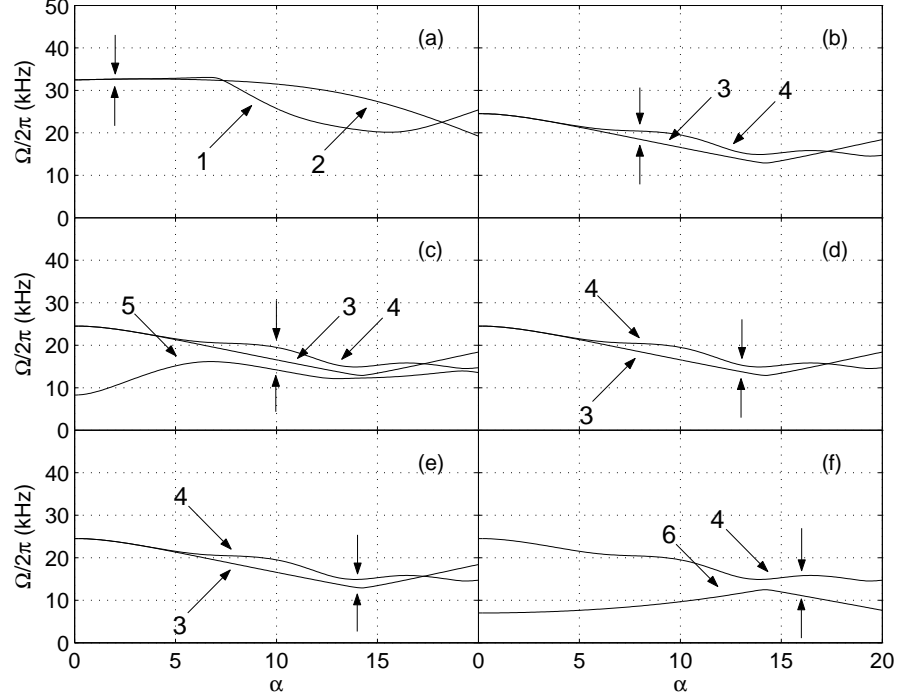


Figure 3.8: Dominant Floquet eigenphases as a function of α for the Texas Hamiltonian with $\omega = 6.0$, $n_0 = 4.2$, and $\phi_0 = 0$. The double vertical arrows show the locations in α for which the dominant states were chosen. A probability threshold of 17.0% was applied at each selected α to determine the dominant states. Overlap probabilities and eigenphase frequencies at the selected values of α for the numbered states are: (a) at $\alpha = 2.0$, $P_1 = 24.2\%$, $\Omega_1/2\pi = 32.6\text{kHz}$, $P_2 = 24.1\%$, $\Omega_2/2\pi = 32.6\text{kHz}$, (b) at $\alpha = 8.0$, $P_3 = 37.6\%$, $\Omega_3/2\pi = 18.5\text{kHz}$, $P_4 = 25.3\%$, $\Omega_4/2\pi = 20.4\text{kHz}$, (c) at $\alpha = 10.0$, $P_3 = 42.2\%$, $\Omega_3/2\pi = 16.6\text{kHz}$, $P_4 = 22.2\%$, $\Omega_4/2\pi = 19.5\text{kHz}$, $P_5 = 20.3\%$, $\Omega_5/2\pi = 14.2\text{kHz}$, (d) at $\alpha = 13.0$, $P_3 = 45.5\%$, $\Omega_3/2\pi = 13.8\text{kHz}$, $P_4 = 30.3\%$, $\Omega_4/2\pi = 15.3\text{kHz}$, (e) at $\alpha = 14.0$, $P_3 = 35.9\%$, $\Omega_3/2\pi = 13.0\text{kHz}$, $P_4 = 28.5\%$, $\Omega_4/2\pi = 14.9\text{kHz}$, and (f) at $\alpha = 16.0$, $P_6 = 48.7\%$, $\Omega_6/2\pi = 11.1\text{kHz}$, $P_4 = 19.3\%$, $\Omega_4/2\pi = 15.8\text{kHz}$.

each of those is assigned a number to help identify it. The double vertical arrows in each segment of Fig. 3.8 shows the location in α at which the states shown in that segment are dominant and have an overlap probability above the threshold. Taking the difference between the frequencies of the states at these values of α will give the dominant oscillation frequencies at that α .

For $\alpha = 2.0$ in Fig. 3.8a, there are two dominant states which are degenerate at low values of α . Therefore, the oscillation frequency at $\alpha = 2.0$ is 0. At higher values of α the two states separate, but by that point they are no longer dominant. For the remaining values of α shown in the figure, except for $\alpha = 16$, the state 3 and state 4 are dominant with state 3 have the largest overlap probability. Therefore, simply taking the difference between only these two state's eigenfrequencies will determine the dominant frequency for much of the range of α . At $\alpha = 10$, a third state is above the threshold. This additional state gives two additional possible frequencies for the tunneling oscillations. Experimentally, only two of these frequencies, $\Delta\Omega_{12}$ and $\Delta\Omega_{13}$, were observed. For $\alpha = 16$, the second state is the same as those at lower values of α , but the primary state has changed. This change is because of the avoided crossing which occurs at $\alpha = 14.2$ between the previously strongest state and this new state.

Husimi plots for the Floquet states are instructive for understanding the reason why they dominate for various values of α . Only 11 Floquet states have support in momentum in the region, $n = -5$ to $n = 5$, and thus determine the dynamics in the chaotic region. The Husimi plots for the Floquet states which,

for the experimental amplitude parameter value of $\alpha = 9.7$, have the largest overlap probability are shown in in Figs. 3.9a-d. Three of these states dominate

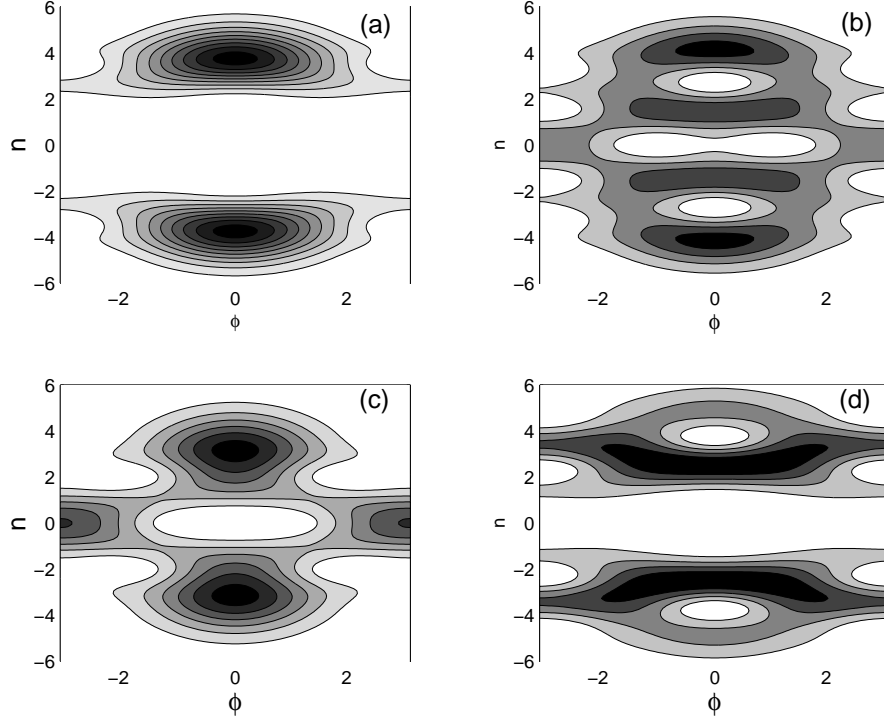


Figure 3.9: Husimi plots of Floquet eigenstates for the Texas experiment for $\omega = 6.0$ and $\alpha = 9.7$. (a) Floquet eigenphase $\Omega_{3.9a}/2\pi = 16.9\text{kHz}$ and an overlap probability, $P_{3.9a} = 0.416$. State (b) Floquet eigenphase $\Omega_{3.9a}/2\pi = 19.7\text{kHz}$ and an overlap probability, $P_{3.9b} = 0.224$. (c) Floquet eigenphase $\Omega_{3.9a}/2\pi = 14.5\text{kHz}$ and an overlap probability, $P_{3.9c} = 0.20$. (d) Floquet eigenphase $\Omega_{3.9a}/2\pi = 18.4\text{kHz}$ and an overlap probability, $P_{3.9d} = 0.045$.

the dynamics. The dark regions of these plots show the region of the classical phase space where the probability of finding the cesium atoms is largest. The eigenphase differences, $(\Omega_{3.9b} - \Omega_{3.9a})/2\pi = 2.89\text{kHz}$ and $(\Omega_{3.9a} - \Omega_{3.9c})/2\pi = 2.40\text{kHz}$ correspond to the two dominant oscillation frequencies observed by

the Texas experiment at $\alpha = 9.7$. The state in Fig. 3.9d has the fourth highest overlap probability, $P_d = 0.045$, but it lies in the chaotic sea. The state in Fig. 3.9d and others not shown contribute to the fine scale structure in these curves.

Husimi Plots for Floquet state 3 in Fig. 3.8 are shown in Fig. 3.10. This

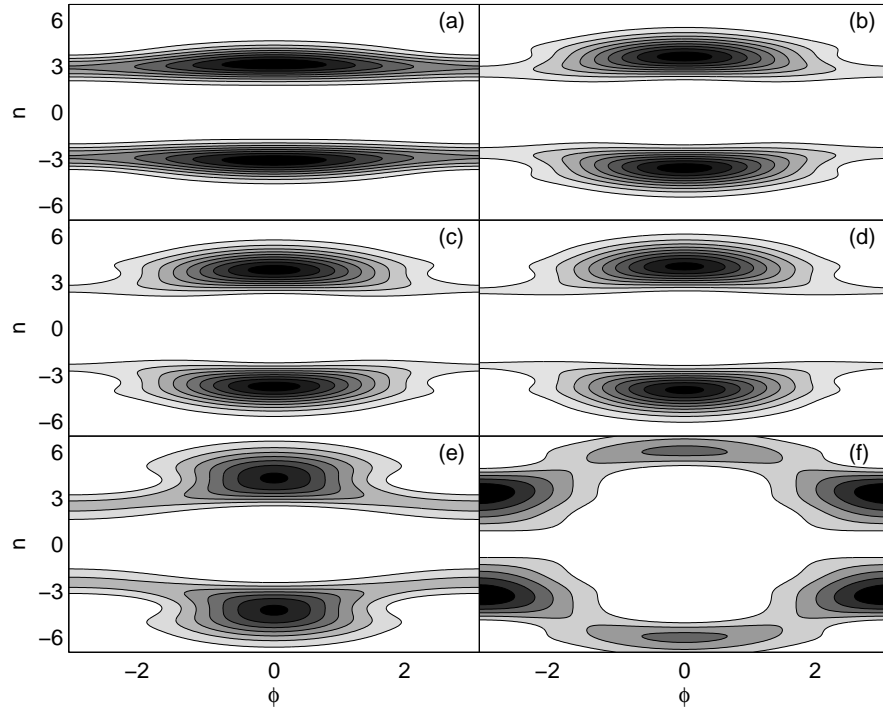


Figure 3.10: Husimi plots of Floquet eigenstate 3 for the Texas Hamiltonian with $\omega = 6.0$ and selected values of α : (a) at $\alpha = 2.0$, $P_3 = 14.0\%$, $\Omega_3/2\pi = 23.8$ kHz, (b) at $\alpha = 8.0$, $P_3 = 37.6\%$, $\Omega_3/2\pi = 18.5$ kHz, (c) at $\alpha = 10.0$, $P_3 = 42.2\%$, $\Omega_3/2\pi = 16.6$ kHz, (d) at $\alpha = 13.0$, $P_3 = 45.5\%$, $\Omega_3/2\pi = 13.8$ kHz, (e) at $\alpha = 14.0$, $P_3 = 35.9\%$, $\Omega_3/2\pi = 13.0$ kHz, and (f) at $\alpha = 16.0$, $P_3 = 0.2\%$, $\Omega_3/2\pi = 14.4$ kHz.

is the dominant state for much of the range of α because of its large support

over the outer islands shown in the classical strobe plots of Fig. 3.1. Since this is where the initial coherent state is located, the coherent state has its largest overlap with this Floquet state. In Fig. 3.8, state 3 is dominant except for $\alpha = 2.0$ and $\alpha = 16.0$. Note that these are the two values of α in Fig. 3.10a and Fig. 3.10f in which the shape of the Husimi function changes from its large support at $n_0 = 4.2$.

The Husimi plots for Floquet state 4 are given in Fig. 3.11. This state has the second largest support over the outer islands for every α shown except for $\alpha = 2.0$. Even though it has support at $n_0 = 4.2$, only a fraction of its probability lies in the neighborhood of $n = 4.2$. This takes away from its probability amplitude at the values of momentum where the initial coherent state is located. Thus, it is not the most dominant state. Comparing Fig. 3.10a to Fig. 3.11a shows that these two dominant states start off with the same shape at low values of α . This is because they are degenerate states at these values of α , as shown in Figure Fig. 3.8b. Fig. 3.12a and Fig. 3.12b show the probability amplitude of these two states at $\alpha = 2.0$. They are obviously a symmetric and antisymmetric pair. However, as α increases and the degeneracy lifts, they change shape and cease to be a symmetric and antisymmetric pair.

The Husimi plot for state 5, which is the third dominant state at $\alpha = 10.0$ is shown in Fig. 3.13. It changes shape throughout the range of α due to multiple avoided crossings. This is evident from Fig. 3.8c. Fig. 3.13c shows large support at the outer islands which is the reason for its dominance. The shape which gives a large overlap with the initial coherent state starts to

develop at $\alpha = 8.0$, as shown in Fig. 3.13b. Thus, for a range of α there are multiple dominant frequencies due to this third state being present. This is consistent with the experiment which obtained multiple oscillation frequencies for the range of α from 8.9 to 10.3 [62] and with our own results in Fig. 3.6.

Fig. 3.14 shows the Husimi plots for state 6 before and after the avoided crossing. This state is only dominant for large values of α , as shown in Fig. 3.8f. Comparing Fig. 3.14d with Fig. 3.10f and Fig. 3.14f with Fig. 3.10d shows that states 3 and 6 have switched shapes after their avoided crossing. They have also switched dominance. Before $\alpha = 14.2$, the location of the avoided crossing, state 3 has the largest overlap with the initial coherent state because of its large support on the outer islands. After the avoided crossing, state 6 becomes the dominant state because it takes on that same shape.

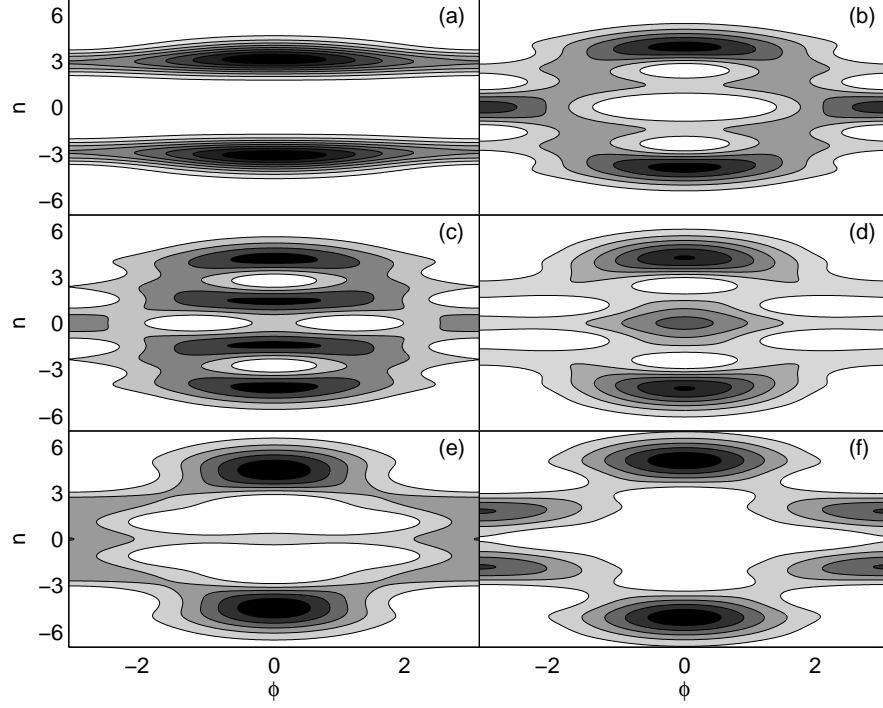


Figure 3.11: Husimi plots of Floquet eigenstate 4 for the Texas Hamiltonian with $\omega = 6.0$ and selected values of α : (a) at $\alpha = 2.0$, $P_4 = 14.0\%$, $\Omega_4/2\pi = 23.8$ kHz, (b) at $\alpha = 8.0$, $P_4 = 25.3\%$, $\Omega_4/2\pi = 20.4$ kHz, (c) at $\alpha = 10.0$, $P_4 = 22.2\%$, $\Omega_4/2\pi = 19.5$ kHz, (d) at $\alpha = 13.0$, $P_4 = 30.3\%$, $\Omega_4/2\pi = 15.3$ kHz, (e) at $\alpha = 14.0$, $P_4 = 28.5\%$, $\Omega_4/2\pi = 14.9$ kHz, and (f) at $\alpha = 16.0$, $P_4 = 19.3\%$, $\Omega_4/2\pi = 15.8$ kHz.

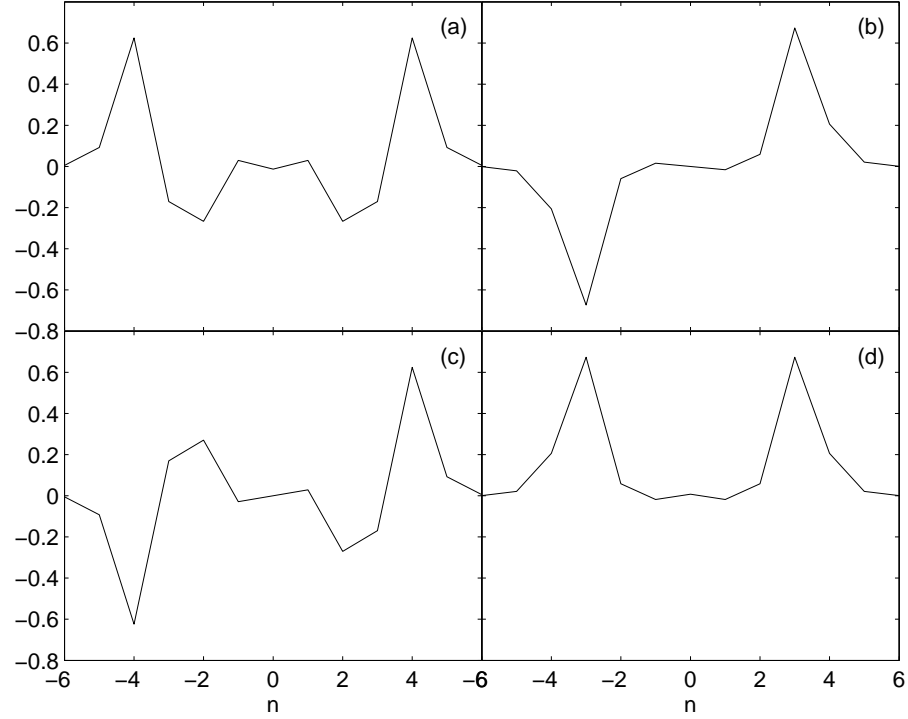


Figure 3.12: Floquet eigenstates projected onto momentum for the Texas Hamiltonian at $\alpha = 2.0$: (a) $\langle n | \chi_1 \rangle$, (b) $\langle n | \chi_3 \rangle$, (c) $\langle n | \chi_2 \rangle$, (d) $\langle n | \chi_4 \rangle$. Symmetric and antisymmetric pairs are placed vertically in the chart. Floquet states 1 and 2 and states 3 and 4 are degenerate pairs.

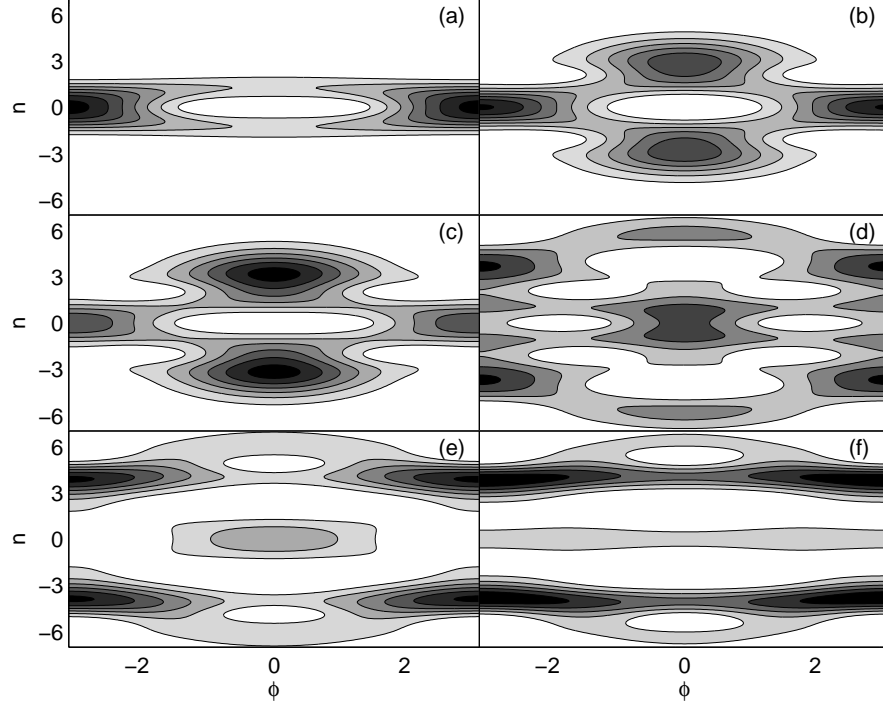


Figure 3.13: Husimi plots of Floquet eigenstate 5 for the Texas Hamiltonian with $\omega = 6.0$ and selected values of α : (a) at $\alpha = 2.0$, $P_5 = 0\%$, $\Omega_5/2\pi = 10.5$ kHz, (b) at $\alpha = 8.0$, $P_5 = 13.9\%$, $\Omega_5/2\pi = 15.7$ kHz, (c) at $\alpha = 10.0$, $P_5 = 20.3\%$, $\Omega_5/2\pi = 14.2$ kHz, (d) at $\alpha = 13.0$, $P_5 = 0.1\%$, $\Omega_5/2\pi = 12.2$ kHz, (e) at $\alpha = 14.0$, $P_5 = 6.1\%$, $\Omega_5/2\pi = 12.3$ kHz, and (f) at $\alpha = 16.0$, $P_5 = 15.8\%$, $\Omega_5/2\pi = 12.6$ kHz.

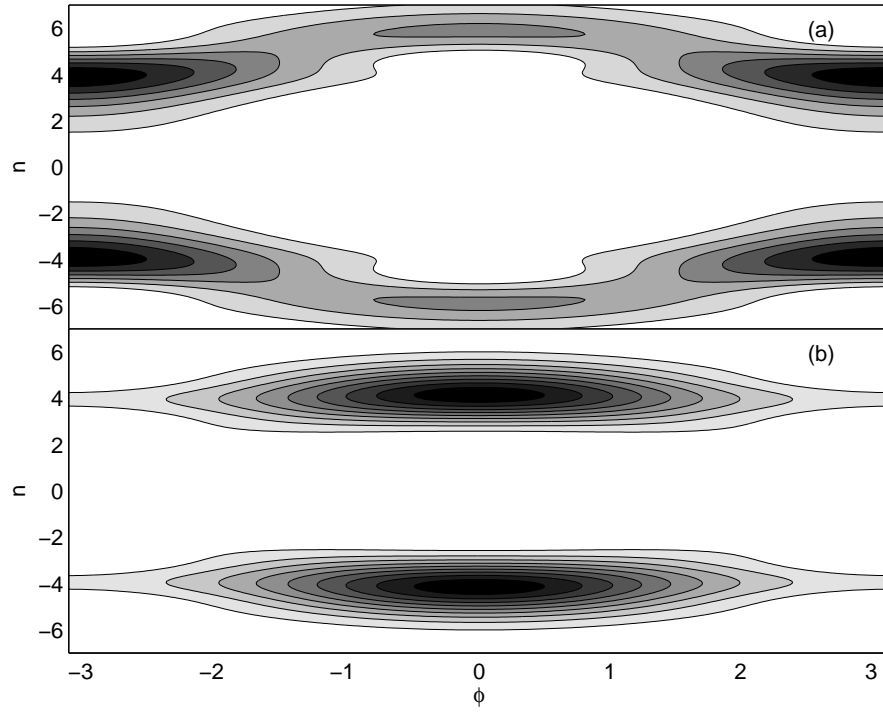


Figure 3.14: Husimi plots of Floquet eigenstate 6 for the Texas Hamiltonian with $\omega = 6.0$ and selected values of α : (a) at $\alpha = 13.0$, $P_6 = 1.4\%$, $\Omega_6/2\pi = 11.7$ kHz, (b) at $\alpha = 16.0$, $P_6 = 48.7\%$, $\Omega_6/2\pi = 11.1$ kHz.

Chapter 4

Nist Experiment

I now consider the NIST experiment [29], which used a Bose-Einstein condensate of sodium atoms to observe dynamic tunneling. Formation of a condensate with the sodium atoms yields a narrower distribution of initial momenta than the Texas experiment.

4.1 Experiment Hamiltonian

4.1.1 System Model

In the NIST experiment, even though the atoms are prepared as a BEC, once they are placed in the standing wave of the laser, the nonlinearities of the BEC have negligible effects and the dynamics appears to be well described by the linear Schrödinger equation.

4.1.2 Hamiltonian Derivation

The Hamiltonian used to model the dynamics observed in the experiment is

$$\hat{H} = \frac{\hat{p}^2}{2m} + \hbar U_0^2 (1 + 2\varepsilon \sin \omega_m t) \sin^2 k_L \hat{x}, \quad (4.1)$$

where \hat{x} and \hat{p} are the center-of-mass position and momentum variables respectively, U_0 is the well depth, ω_m is the modulation frequency, t is the time, m is the mass, k_L is the laser wave vector, and ε is an adjustable modulation parameter.

4.1.3 Hamiltonian Scaling

The scaled Hamiltonian used by the experimentalists [29] is given by

$$\hat{H}_{\text{exp}} = \frac{\hat{\rho}^2}{2} + 2\kappa (1 + 2\varepsilon \sin \omega_m t) \sin^2 \frac{\hat{\phi}}{2}, \quad (4.2)$$

where $\hat{\rho} = (2k_L/m\omega_m)\hat{p}$, $\hat{\phi} = 2k_L x$, $\kappa = 2\hbar k_L^2 U_0^2 / m\omega_m^2$, and $\hat{H}_{\text{exp}} = (4k_L^2 / m\omega_m^2)\hat{H}$. The experimental data was not taken with starting time, $t = 0$, but rather with starting times, $t = T_m/4$ and $t = 3T_m/4$, where $T_m = 2\pi/\omega_m$ is the modulation period.

4.2 Experimental Results

The experiment reported observing a number of dynamic tunneling oscillation periods, τ . For $\omega_m/2\pi = 250$ kHz ($\omega/2\pi = 2.5$), $\kappa = 1.66$, and $\varepsilon = 0.29$, they find $\tau = 10.3T$ (10.3 modulation periods). For $\omega_m/2\pi = 250$ kHz, $\kappa = 1.75$, and $\varepsilon = 0.23$, they find $\tau = 13T$. The experimentally observed oscillation periods are reproduced below using Floquet analysis. It is found that the dynamical tunneling observed in the experiment is in all cases due to the interference of two Floquet states which have a very large probability to be excited by the initial conditions of the experiment.

4.3 Theoretical Hamiltonian

Interaction of the sodium atoms with the modulated standing wave of light, induces momentum transfer between the standing wave and the atoms in integer multiples of $2\hbar k_L$. This induces a quantization of the allowed momentum changes of the sodium atoms, as they interact with the standing wave, and allows us to construct a very simple theory of the atomic dynamics. The dynamics of this system can be modeled with a Hamiltonian in which the momentum is explicitly quantized in units of $2\hbar k_L$. This is done by scaling the variables in Eq. (4.2) so that $\hat{\rho} = (4\hbar k_L^2/m\omega_m)\hat{n}$, and $\hat{H}_{\text{exp}} = (8k_L^4\hbar^2/m^2\omega_m^2)\hat{H}_{\text{th}}$. If we incorporate the time shifts into the Hamiltonian, then Eq. (4.2) takes the form

$$\begin{aligned} \hat{H}_{\text{th}} = \hat{n}^2 + \frac{\omega^2\kappa}{2} \Big[& 1 + 2\nu\varepsilon \cos \omega t' - \cos \hat{\phi} \\ & - \nu\varepsilon \cos (\hat{\phi} - \omega t') - \nu\varepsilon \cos (\hat{\phi} + \omega t') \Big], \end{aligned} \quad (4.3)$$

where \hat{n} is a scaled atomic center of mass momentum whose eigenvalues, n , are the integers, $-\infty \leq n \leq \infty$, ω and t are the scaled nondimensional frequency and time, and $\nu = \pm 1$. For $\nu = +1$ ($\nu = -1$), Eq. (4.3), with starting time $t = 0$ reproduces the dynamics of the NIST experiment which has starting time $t = T_m/4$ ($t = 3T_m/4$). From Eq. (4.3), we see that the NIST experiment can be modeled in terms of a modulated pendulum, where κ determines the amplitude of the unmodulated pendulum and ε determines the amplitude of the modulation. The modulation period, in our new scaled units, is $T = 2\pi/\omega$. In the experiment, the two parameters, κ and ε , can be varied independently.

4.4 Classical Dynamics

To understand the quantum dynamics of the system whose dynamics is governed by the Hamiltonian in Eq. 4.3, it is useful first to examine the structure of the underlying classical phase space. The classical limit of Eq. 4.3 can be obtained simply by allowing n to take on a continuum of values. The equations of motion for the classical system are then given by Hamilton's equations, $dn/dt = -\partial H/\partial\phi$ and $d\phi/dt = \partial H/\partial n$.

For small amplitudes, κ and $\kappa\varepsilon$, the NIST Hamiltonians have three primary resonances. For $\nu = -1$, they are located at $(n = 0, \phi = 0)$ and $(n = \pm\omega/2, \phi = \pm\pi)$, while for $\nu = +1$, they are located at $(n = 0, \phi = 0)$ and $(n = \pm\omega/2, \phi = 0)$. They have half-widths, $\Delta n_0 = \sqrt{\omega^2\kappa}$ and $\Delta n_{\pm} = \sqrt{\omega^2\kappa\varepsilon}$ [50].

A strobe plot of the classical phase space for the Hamiltonian in Eq. ?? with $\nu = -1$ and experimental parameters $\omega_m/2\pi = 250\text{kHz}$, $\omega = 2.5$, $\kappa = 1.66$ and $\varepsilon = 0.29$ is shown in Fig. 4.1c. Seven Floquet states determine the dynamics in the chaotic region between $n = -3$ and $n = 3$. For the parameters used in the experiment, the pendulum approximation predicts the primary resonances to lie at $n = 0$ and $n = \pm 1.25$, and have half-widths, $\Delta n_0 = 3.2$ and $\Delta n_{\pm} = 1.7$. We find that the primary resonances are totally destroyed at $\kappa \approx 0.2$, and then new resonances, which resemble the primaries, reappear and disappear repeatedly as κ is increased. For $\kappa = 1.66$ and $\varepsilon = 0.29$, a large resonance exists at $(n = 0, \phi = 0)$ and three small pairs of higher order resonances exist at $(n \approx \pm 1.5, \phi = \pm\pi)$, $(n \approx \pm 3.0, \phi = 0)$ and $(n \approx \pm 2.0, \phi =$

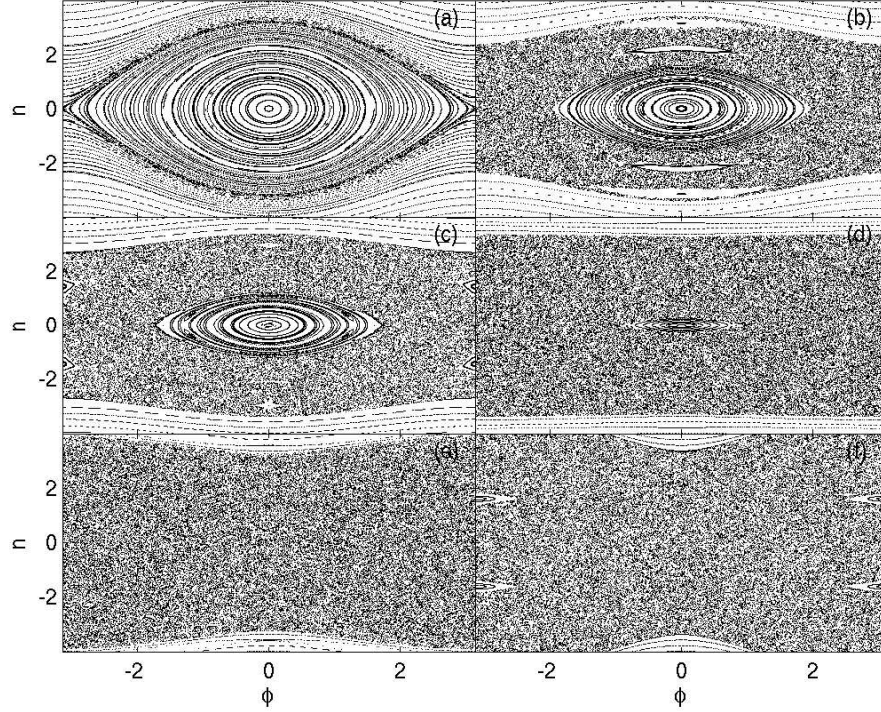


Figure 4.1: Classical strobe plots for the NIST Hamiltonian at $\kappa = 1.66$ and selected values of ε : (a) $\varepsilon = 0.0$, (b) $\varepsilon = 0.2$, (c) $\varepsilon = 0.29$, (d) $\varepsilon = 0.5$, (e) $\varepsilon = 0.7$ and (f) $\varepsilon = 1.0$.

0).

4.5 Quantum Evolution

In Fig. 4.2 we show the time evolution of the momentum expectation value for two different initial conditions for the $\nu = -1$ Hamiltonian at parameter values, $\kappa = 1.66$, $\varepsilon = 0.29$, $\omega = 2.5$ and $\omega_m/2\pi = 250\text{kHz}$. Fig. 4.2a, with $(n_0 = 1.6, \phi_0 = 0)$, shows a somewhat noisy oscillation with a dominant frequency 24.9kHz (10.0 modulation periods), which is in good agreement with

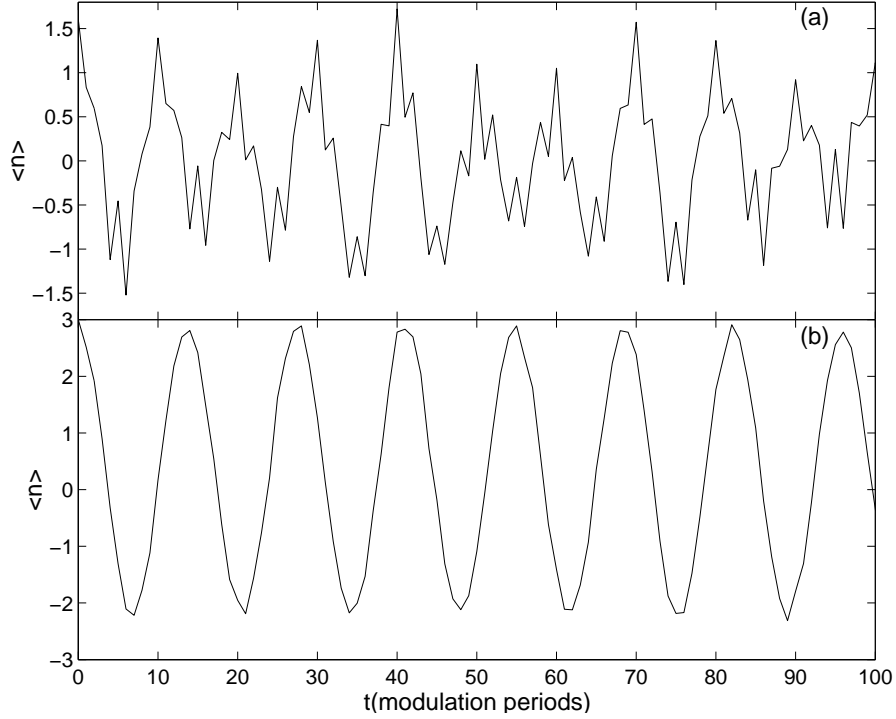


Figure 4.2: Evolution of momentum expectation value, $\langle n \rangle$ (in dimensionless units) for the NIST experiment for $\kappa = 1.66$, $\varepsilon = 0.29$, $\omega = 2.5$ and $\omega_m/2\pi = 250\text{kHz}$: (a) $n_0 = 1.6$, and $\phi_0 = 0$; (b) $n_0 = 3.0$, and $\phi_0 = 0$.

the experimental result. Fig. 4.2b shows the case with $(n_0 = 3.0, \phi_0 = 0)$. A clean oscillation with frequency 18.3kHz (13.7 modulation periods) occurs. This oscillation was not observed in the experiment, but we expect it would show up in a power spectrum of the experimental data.

4.6 Floquet Analysis

We now consider a Floquet analysis for both Hamiltonians, $\nu = \pm 1$. The Floquet eigenphases for $\nu = \pm 1$ are identical, but the Floquet eigenstates

associated with each eigenphase are different for the two Hamiltonians. Let us first consider the $\nu = -1$ Hamiltonian with parameters, $\kappa = 1.66$, $\varepsilon = 0.29$, $\omega = 2.5$ and $\omega_m/2\pi = 250\text{kHz}$. In Fig. 4.3a and Fig. 4.3b, we show the two Floquet states which dominate the dynamics for initial condition, $(n_0 = 1.6, \phi_0 = 0)$. They have a frequency difference, $(\Omega_b - \Omega_a)/2\pi = 25.0\text{kHz}$.

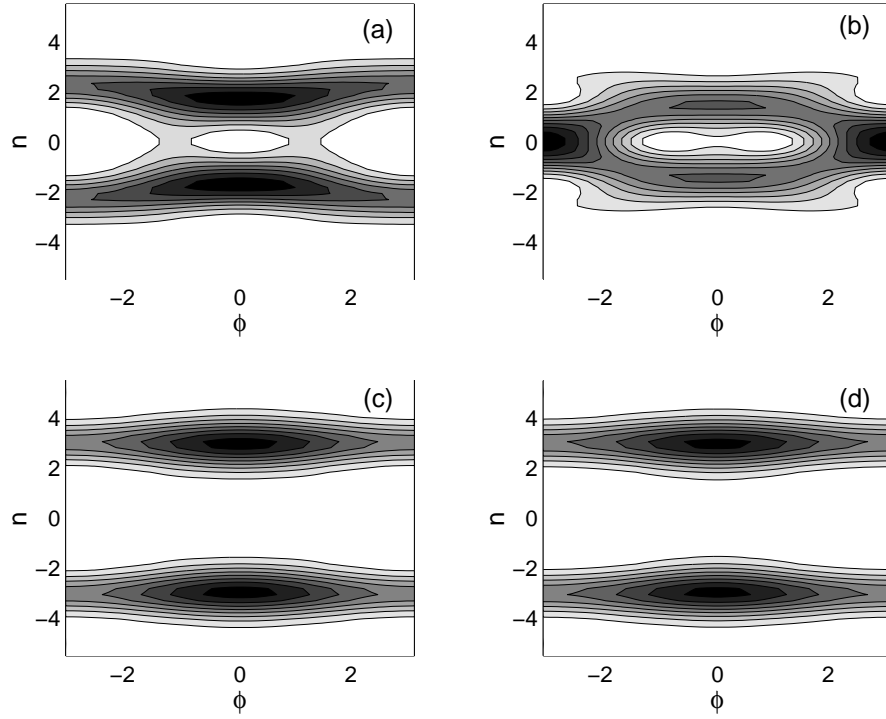


Figure 4.3: Husimi plots of Floquet eigenstates for the NIST experiment with $\kappa = 1.66$, $\varepsilon = 0.29$, $\omega = 2.5$ and $\omega_m/2\pi = 250\text{kHz}$. (a) Floquet eigenphase $\Omega_a/2\pi = 49.0\text{kHz}$ and overlap probability $P_a = 0.380$. State (b) Floquet eigenphase $\Omega_{6b}/2\pi = 73.9\text{kHz}$ and overlap probability $P_b = 0.306$. (c) Floquet eigenphase $\Omega_c/2\pi = 15.3\text{kHz}$ and overlap probability $P_c = 0.427$. (d) Floquet eigenphase $\Omega_d/2\pi = 33.5\text{kHz}$ and overlap probability $P_d = 0.421$.

Their frequency difference accounts for the oscillation of 10 modulation periods

reported in [29]. These Floquet states are not even-odd pairs as suggested in [29], and they both lie in the chaotic sea. If the effective Planck's constant for this experiment were smaller, more Floquet states would be supported by the chaotic region and we would not expect to find this simple oscillation [66] for this initial condition.

If we take initial condition, $(n_0 = 3.0, \phi_0 = 0)$ for $\nu = -1$, we obtain the oscillation shown in Fig. 4.2b. This oscillation results from the even-odd Floquet pair shown in Fig. 4.3c and Fig. 4.3d. Fig. 4.3c (Fig. 4.3d) is even (odd) under the transformation $n \rightarrow -n$. They have a frequency difference, $(\Omega_c - \Omega_d)/2\pi = 18.3\text{kHz}$. This oscillation appears to result from states sitting the outer-most nonlinear resonance.

We finally consider the $\nu = +1$ Hamiltonian with parameters, $\kappa = 1.66$, $\varepsilon = 0.29$, $\omega = 2.5$ and $\omega_m/2\pi = 250\text{kHz}$. We find that the 25.0kHz (10 modulation periods) oscillation dominates those initial momentum states which are centered at $\phi = 0$ and lie in the interval $n_0 = 1.7$ to $n_0 = 3.0$. These oscillations appear to result from the two Floquet states which lie in the chaotic sea. If we change the parameters to $\kappa = 1.82$ and $\varepsilon = 0.30$ and the modulation frequency to $\omega_m = 222\text{kHz}$, the dominant frequency for initial state, $(n_0 = 2.0, \phi_0 = 0)$, is 36.8kHz (6.03 modulation periods), which is in agreement with the NIST experiment.

4.6.1 Floquet States for Fixed Pendulum Amplitude at $\kappa = 1.66$ and Varying Modulation ε

Fig. ?? shows surfaces of section (strobe plots) of the classical phase space for six different values of ε for $\kappa = 1.66$. The first is at $\varepsilon = 0.0$ and shows the pendulum structure of the Hamiltonian, Eq. (??), due to the $\cos \hat{\phi}$ term. As ε increases, the chaotic region surrounding the central island increases in size. For Fig. ??b, $\varepsilon = 0.2$ a pair of islands symmetrical in momentum space appear. By $\varepsilon = 0.29$, the experimental value, in Fig. ??c, the outer islands have been greatly reduced in size. In the rest of Fig. ??, the chaotic region increases and all islands eventually disappear in the central momentum region. It is important to note that the region of mixed phase space extends approximately over the interval, $-3 \leq n \leq 3$. This means that for the quantum system, the region of underlying mixed classical phase space extends over seven momentum states.

We can obtain “surfaces of section” of the Floquet eigenstates by means of Husimi plots [31] which give the distribution of probability of an eigenstate in the underlying classical phase space. In examining the Husimi plots for this system, we find that eleven Floquet states have significant probability in the region of phase space dominated by the resonances and chaotic orbits. A few of these states lie in the region of KAM tori outside the chaotic region but still appear to interact with the states in the chaotic region. In Fig. 4.4 we plot the Floquet eigenphases for these states as a function of ε . There are a number of interesting features that we can comment on. For example,

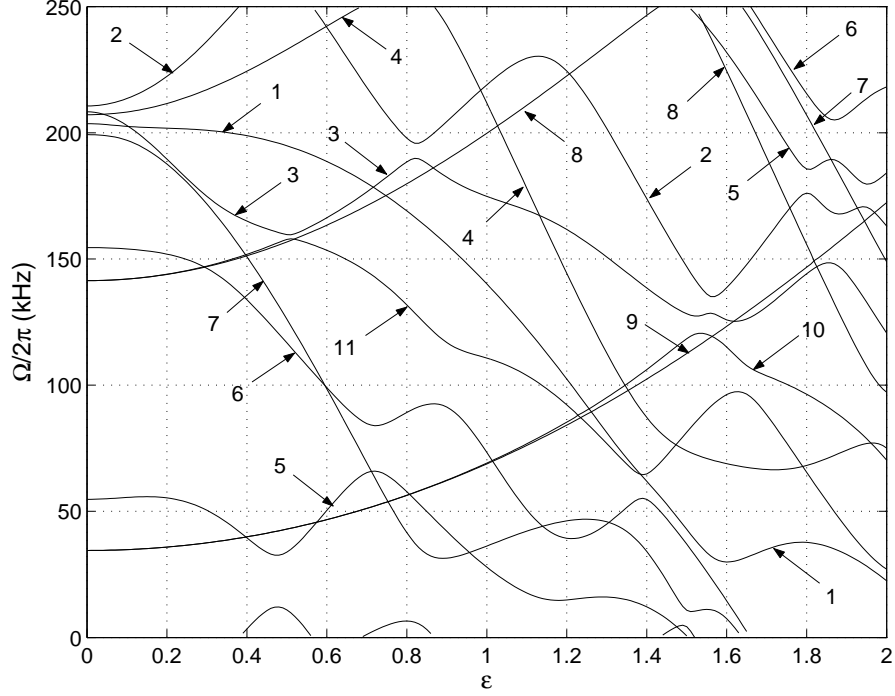


Figure 4.4: Floquet eigenphases for NIST experiment for 11 states as a function of ε at $\kappa = 1.66$.

consider the avoided crossing at $\varepsilon = 0.51$ between Floquet states 3 and 11. This avoided crossing causes state 3 and state 11 to exchange shapes. This is obvious by comparing state 3 before ($\varepsilon < 0.51$) the avoided crossing, Fig. 4.5a, to state 11 after ($\varepsilon > 0.51$) the avoided crossing, Fig. 4.5d. State 11 before the avoided crossing has support in the KAM tori region outside of the chaotic sea as shown in Fig. 4.5c, while state 3 has this same support after the avoided crossing as shown in Fig. 4.5b.

There is an avoided crossing at $\varepsilon = 0.82$ between Floquet states 2 and

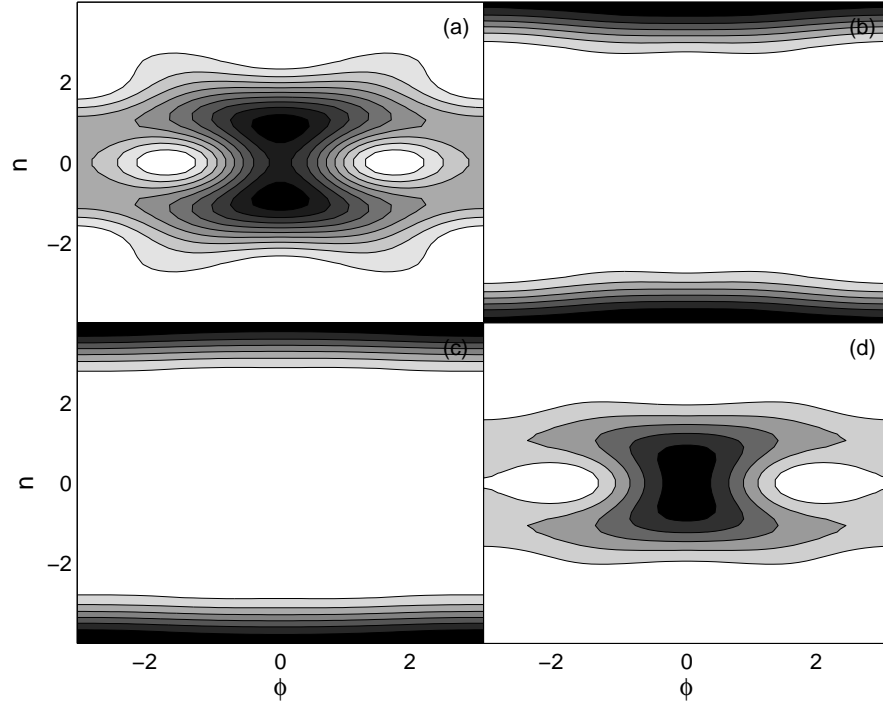


Figure 4.5: Husimi plots of Floquet eigenstates at $\kappa = 1.66$ and selected values of ε for the avoided crossing at $\varepsilon = 0.51$: (a) state 3 at $\kappa = 0.45$, $P_3 = 11.0\%$, (b) state 3 at $\kappa = 0.6$, $P_3 = 0.1\%$, (c) state 11 at $\kappa = 0.45$, $P_{11} = 0.3\%$, and (d) state 11 at $\kappa = 0.6$, $P_{11} = 5.8\%$.

3. This avoided crossing causes state 2 and state 3 to exchange shapes. This is shown in Fig. 4.6. In Fig. 4.6a we show state 2 before the avoided crossing and in Fig. 4.6d we show state 3 after the avoided crossing. Before the avoided crossing, state 2 has support on the two pairs of islands at $\phi = \pm\pi$, while state 3 has support in the KAM tori region outside of the chaotic sea [see Fig. 4.6c]. After the avoided crossing the two states have interchanged identities.

In Fig. 4.7, we show the result of a multiple avoided crossing which

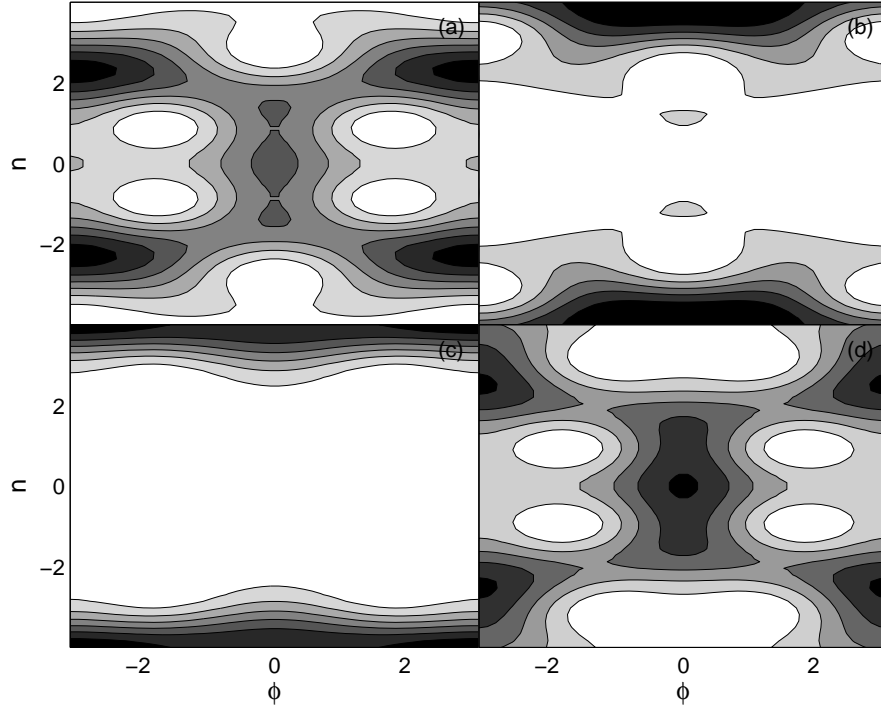


Figure 4.6: Husimi plots of Floquet eigenstates at $\kappa = 1.66$ and selected values of ε for the avoided crossing at $\varepsilon = 0.82$: (a) state 2 at $\kappa = 0.8$, $P_2 = 11.3\%$, (b) state 2 at $\kappa = 0.85$, $P_2 = 0.6\%$, (c) state 3 at $\kappa = 0.8$, $P_3 = 2.5\%$, and (d) state 3 at $\kappa = 0.85$, $P_3 = 14.7\%$.

illustrates a mechanism, described in Timberlake and Reichl [66], by which wavefunction becomes extended throughout the chaotic region. The multiple avoided crossing at $\varepsilon = 1.6$, shown in Fig. 4.4 involves primarily the Floquet states 2, 10, and 11. The Husimi plots for these states are shown in Fig. 4.7. The spatial distribution of each state changes as they pass through the avoided crossing. Comparison of state 2 before the avoided crossing [Fig. 4.7a] and after the avoided crossing shows that it becomes a superposition of states 10

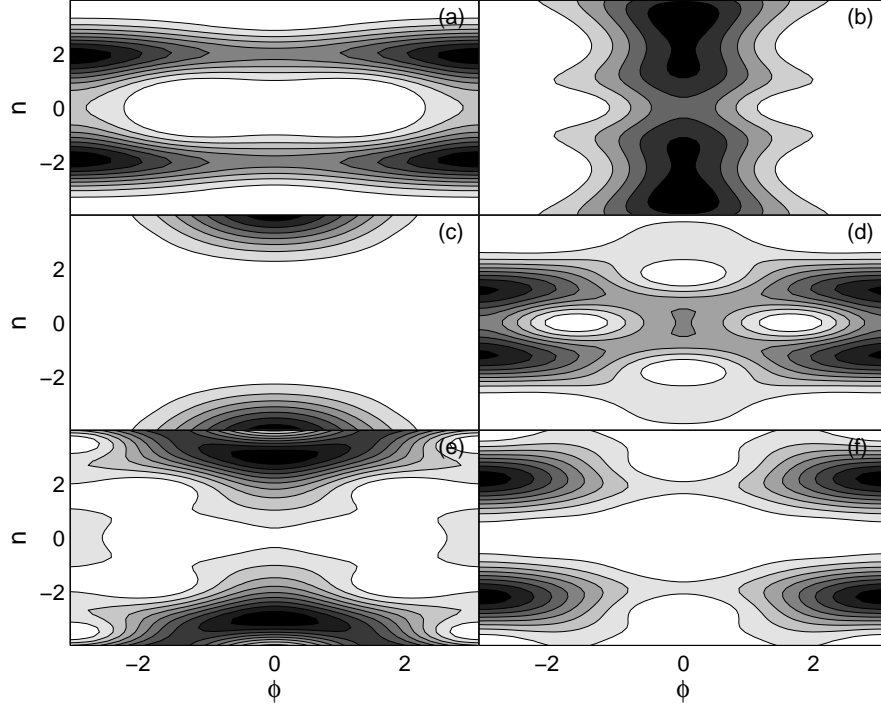


Figure 4.7: Husimi plots of Floquet eigenstates at $\kappa = 1.66$ and selected values of ε for the avoided crossings at $\varepsilon = 1.6$: (a) state 2 at $\kappa = 1.5$, $P_2 = 21.3\%$, (b) state 2 at $\kappa = 1.7$, $P_2 = 25.6\%$, (c) state 10 at $\kappa = 1.45$, $P_{10} = 3.3\%$, (d) state 10 at $\kappa = 1.6$, $P_{10} = 2.1\%$, (e) state 11 at $\kappa = 1.5$, $P_{11} = 10.7\%$, and (f) state 11 at $\kappa = 1.7$, $P_{11} = 4.9\%$.

and 11. Similarly states 10 and 11 take on much of the character of state 2. However, all states are significantly altered by the multiple avoided crossings and become a mixture of the states involved.

Let us now consider what dynamic tunneling frequencies might be observed in an experiment. Experimentally observable dynamic tunneling oscillation frequencies are shown in Fig. 4.8 as a function of ε . Only those frequen-

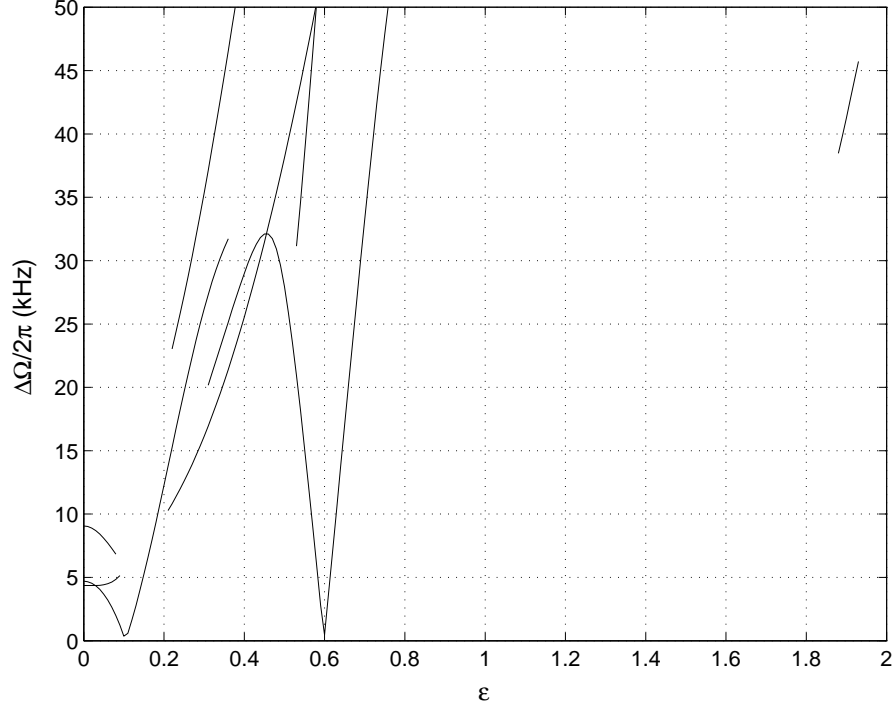


Figure 4.8: Oscillation frequencies as a function of ε at $\kappa = 1.66$ with a threshold of $P_i P_j = 4\%$ of combined overlap.

cies originating from pairs of Floquet states which have an overlap probability with the initial state greater than the threshold of $P_i P_j \geq 0.04$ are plotted. Note that at the experimental value of $\varepsilon = 0.29$, there are three oscillation frequencies. This matches Fig. 7 at the experimental value of $\kappa = 1.66$. Only one of these frequencies was observed in the experiment $\Delta\Omega_{13}/2\pi = 25.0$ kHz. This oscillation frequency is due to interference of Floquet states, 1 and 3, in Fig. 4.4. The Husimi plot for these states are shown in Fig. 4.3. Below we discuss a possible reason why only one of these frequencies was observed in the

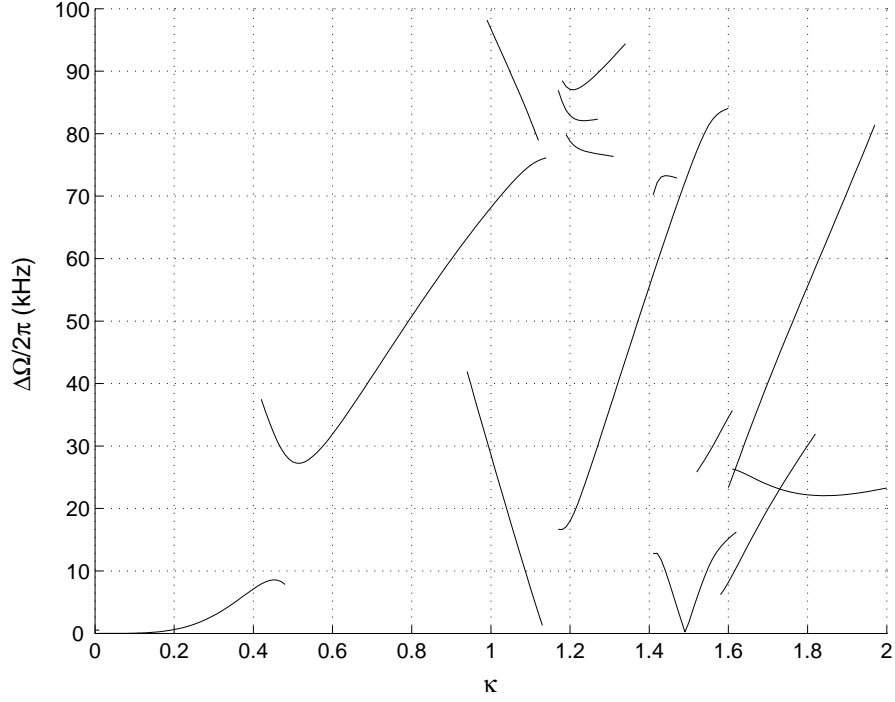


Figure 4.9: Oscillation frequencies as a function of κ at $\varepsilon = 0.29$ with a threshold of $P_i P_j = 4\%$ of combined overlap. At $\kappa = 1.66$, three frequencies have an overlap of 5.8%: $\Delta\Omega_{12}/2\pi = 33.6$ kHz, $\Delta\Omega_{13}/2\pi = 25.0$ kHz and $\Delta\Omega_{14}/2\pi = 15.4$ kHz.

NIST experiment. Note also that for $\varepsilon > 0.8$ there are no more low frequency oscillations. Examining the strobe plots of Fig. ??e and Fig. ??f shows that at this point the central island has disappeared into the chaotic sea. This means that multiple states, each spread throughout the chaotic sea, will be present at the location of initial coherent state. None of those states will dominate over the others, and therefore no single dominant oscillation frequency will be produced.

4.6.2 Floquet States for Varying Pendulum Amplitude κ and Fixed Modulation at $\varepsilon = 0.29$

Let us now consider the behavior of the classical phase space for the case where we hold the modulation amplitude fixed, but vary the over all amplitude of the pendulum. For small values of pendulum amplitude, κ , for fixed $\varepsilon = 0.29$, the Hamiltonian, Eq. (4.3), has three primary resonances as can be seen in Figs. 4.10a and 4.10b. They are located at $(n = 0, \phi = 0)$

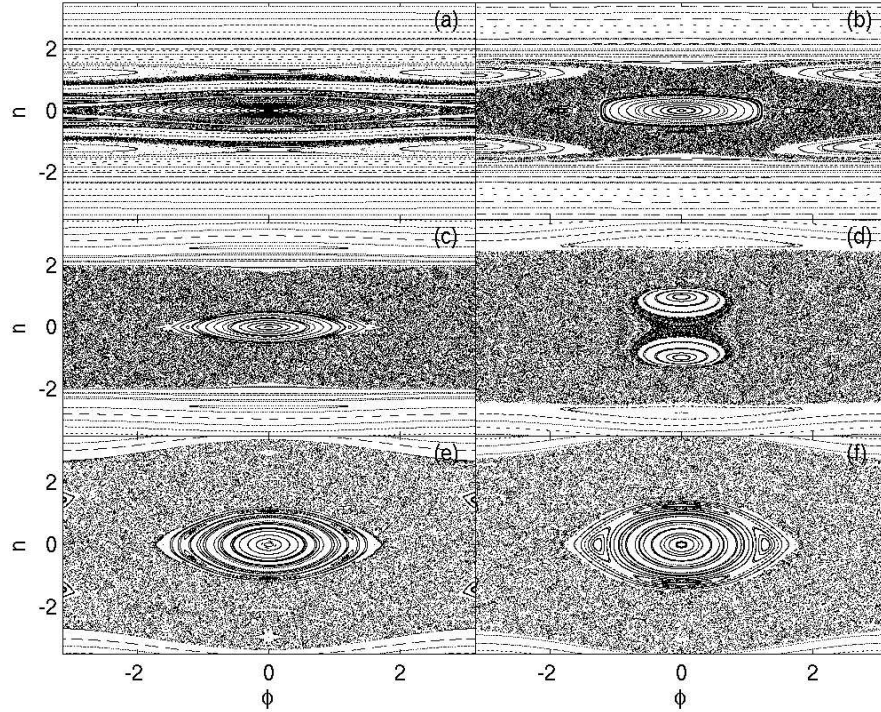


Figure 4.10: Classical strobe plots for NIST experiments at $\varepsilon = 0.29$ and selected values of κ : (a) $\kappa = 0.03$, (b) $\kappa = 0.1$, (c) $\kappa = 0.5$, (d) $\kappa = 1.1$, (e) $\kappa = 1.66$ and (f) $\kappa = 1.9$.

and $(n = \pm\omega/2, \phi = \pm\pi)$. They have half-widths, $\Delta n_0 = \sqrt{\omega^2 \kappa}$ and $\Delta n_{\pm} =$

$\sqrt{\omega^2 \kappa \varepsilon}$. For the scaled modulation frequency of $\omega/2\pi = 2.50$, the outer islands are at $n_{\pm} = \pm 1.25$ for small values of κ . For $\kappa = 0.03$ [Fig. 8(a)], the islands are separated by KAM tori and there is very little chaos in the phase space. As the pendulum amplitude, κ , increases, the islands overlap and the phase space contains a mixture of KAM tori, cantori, and chaotic regions between the islands [50].

As κ increases further, the outer islands are destroyed, the pendulum structure begins to dominate and is surrounded by a chaotic sea. For Fig. 4.10c, $\kappa = 0.5$, only the central island remains. As κ is increased further, the island formed by the pendulum bifurcates into two islands [see $\kappa = 1.1$, Fig. 4.10d]. As κ is increased still further, the bifurcated islands move apart and can be identified as the two outer islands at the experimental value of $\kappa = 1.66$ in Fig. 4.10e. A new stable island forms between them. For still higher values of κ , the newly created central island dominates the phase space.

As we vary κ , only seven Floquet states appear to play a significant role in the dynamics. Fig. 4.11 shows how the Floquet eigenphases of these seven states vary as a function of κ . Most are approximately straight lines and correspond to Floquet eigenstates which lie outside the chaotic region. The eigenphases which undergo substantial variation as a function of κ , lie in the chaotic region. Note that there are many avoided crossings among these states. The rapid rise in the the values of the Floquet eigenphases is due to the constant term, $\omega^2 \kappa/2$, that appears in the Hamiltonian.

Let us again look at the Floquet states involved in the avoided crossings.

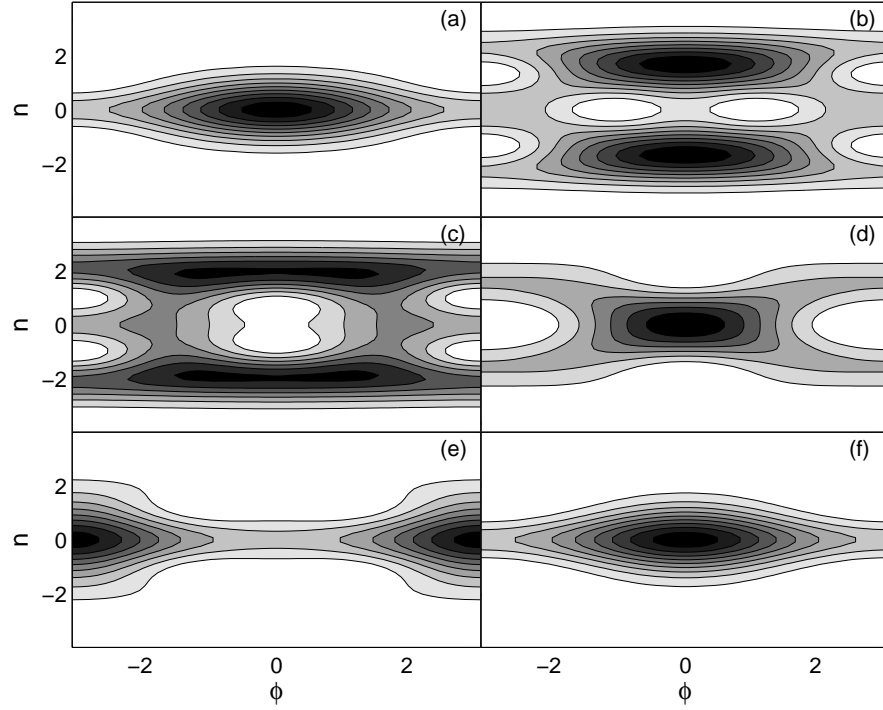


Figure 4.11: Husimi plots of Floquet eigenstates at $\varepsilon = 0.29$ and selected values of κ for the avoided crossing at $\kappa = 0.55$: (a) state 2 at $\kappa = 0.2$, $P_2 = 2.2\%$, (b) state 2 at $\kappa = 0.6$, $P_2 = 36.8\%$, (c) state 6 at $\kappa = 0.4$, $P_6 = 30.0\%$, (d) state 6 at $\kappa = 0.6$, $P_6 = 0.5\%$, (e) state 5 at $\kappa = 0.6$, $P_5 = 3.3\%$, and (f) state 5 at $\kappa = 0.8$, $P_5 = 4.2\%$.

The avoided crossing at $\kappa = 0.55$, shown in Fig. 4.12, involves Floquet states 2, 5, and 6. The Husimi plots for these states are shown in Fig. 4.11. The relative dominance of each state changes as they pass through the avoided crossing since their shapes change. There is a passing of identity from state 2 to states 5 and 6, while state 2, to a large extent, takes on the identity of state 6.

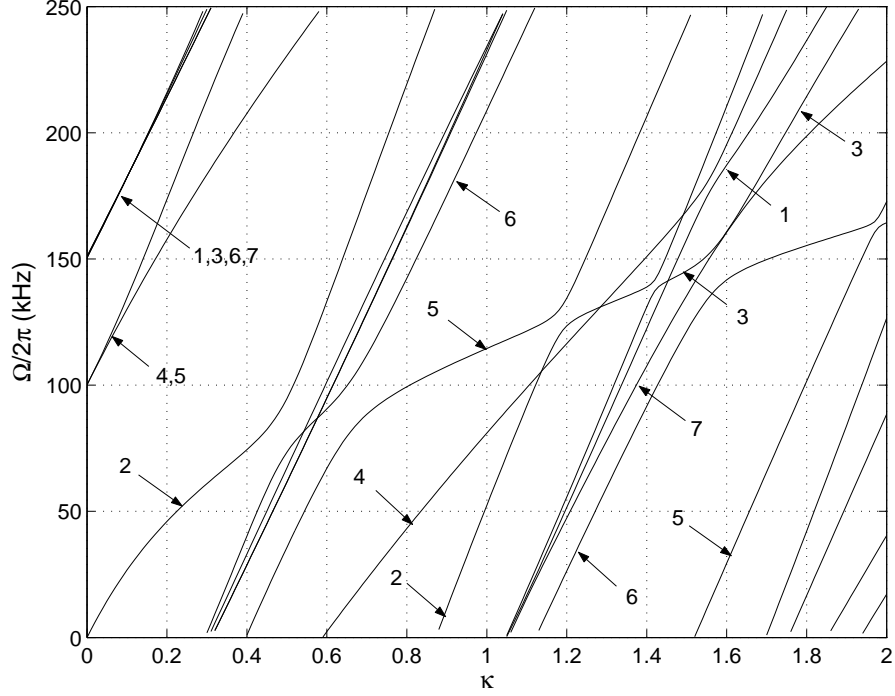


Figure 4.12: Floquet eigenphases for NIST Hamiltonian for 7 states as a function of κ at $\varepsilon = 0.29$. The overlaps at $\kappa = 1.66$ are $P_1 = 31.9\%$, $P_2 = 18.2\%$, $P_3 = 18.2\%$, $P_4 = 18.1\%$, $P_5 = 12.3\%$, $P_6 = 1.5\%$, $P_7 = 0.01\%$.

There are several isolated avoided crossings which involve the interchange of identities: (i) The avoided crossing at $\kappa = 1.19$ involves states 2 and 5. This avoided crossing causes state 5 and state 2 to exchange identities. This is clear when one compares state 5 before the avoided crossing, Fig. 4.13a, to state 2 after the avoided crossing, Fig. 4.13d. (ii) The avoided crossing at $\kappa = 1.57$ involves Floquet states 3 and 6. This avoided crossing causes state 6 and state 3 to exchange identity (shapes). This is obvious by comparing state 3 before the avoided crossing, Fig. 4.14a, to state 6 after the avoided crossing,

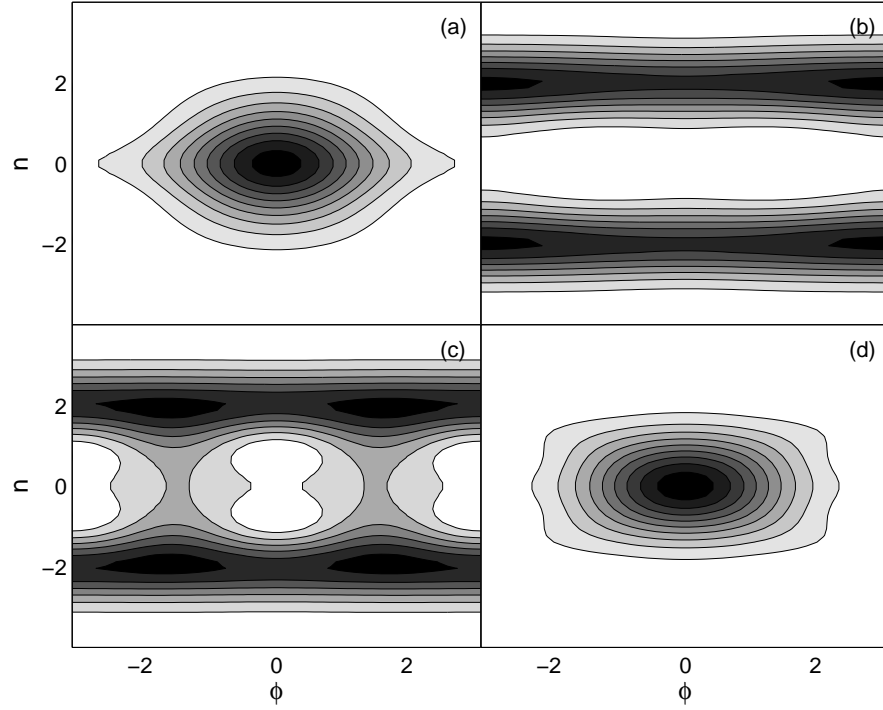


Figure 4.13: Husimi plots of Floquet eigenstates for NIST experiments at $\varepsilon = 0.29$ and selected values of κ for the avoided crossing at $\kappa = 1.19$: (a) state 5 at $\kappa = 1.1$, $P_5 = 10.7\%$, (b) state 5 at $\kappa = 1.3$, $P_5 = 30.9\%$, (c) state 2 at $\kappa = 1.1$, $P_2 = 28.3\%$, and (d) state 2 at $\kappa = 1.3$, $P_2 = 4.3\%$.

Fig. 4.14d. Note that as κ is increased from $\kappa = 1.19$ to $\kappa = 1.57$, the state with support on the large central island has changed from state 2 to 6 to 5, back to 2, then to 3, and finally to 6. These exchanges can be seen as the curve of the eigenvalue of state 2 at low values of κ is followed through each avoided crossing in Fig. ???. As each change takes place the relative dominance of each state changes as can be seen by comparing P_i for each state before and after the avoided crossings. The value of P_i , for each state is given in the figure caption

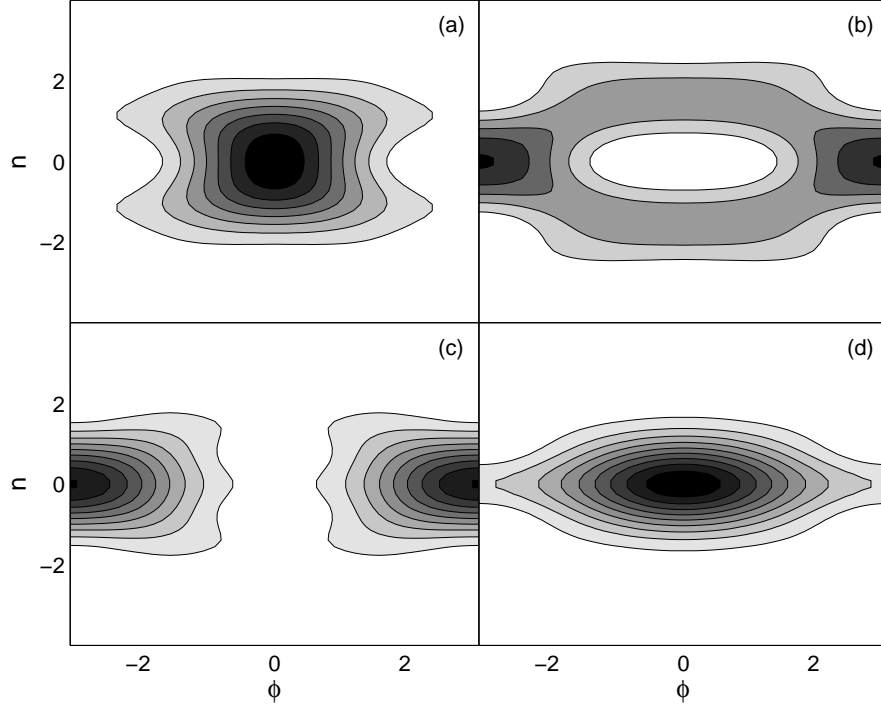


Figure 4.14: Husimi plots of Floquet eigenstates at $\varepsilon = 0.29$ and selected values of κ for the avoided crossing at $\kappa = 1.57$: (a) state 3 at $\kappa = 1.5$, $P_3 = 8.6\%$, (b) state 3 at $\kappa = 1.7$, $P_3 = 19.1\%$, (c) state 6 at $\kappa = 1.4$, $P_6 = 3.1\%$, and (d) state 6 at $\kappa = 1.7$, $P_6 = 2.5\%$.

for its Husimi plot. For example, in Fig. 4.11 state 2 goes from $P_2 = 2.2\%$ to $P_2 = 36.8\%$. In the shape of Fig. 4.11a at $\kappa = 0.2$, state 2 does not dominate. However, when it changes shape to that of Fig. 4.11b at $\kappa = 0.6$, it becomes a dominant state and will contribute to oscillation frequencies.

In Fig. 4.9 we show the dynamic tunneling frequencies that could be observed in an experiment in which κ is varied. As was the case in Fig. 4.8, only those frequencies originating from pairs of Floquet states which have an

overlap probability with the initial state greater than the threshold of $P_i P_j \geq 0.04$ are plotted as a function of κ . Note that at the experimental value of $\kappa = 1.66$, there are three oscillation frequencies. This matches Fig. 4.8 at the experimental value of $\varepsilon = 0.29$. Only one of these frequencies has a slow variation as a function of κ and this was the dynamic tunneling frequency observed in the experiment.

Chapter 5

Conclusions

The model Hamiltonians, with momentum quantized in units of $2\hbar k_L$, give extremely good predictions of the experimental results for the dynamic tunneling frequencies. This is especially true for the Texas experiments where Fig. 3.6 shows very good agreement between the measured frequencies and the theoretical frequency curves. Unfortunately, the NIST experiments did not systematically vary the potential amplitude parameters. As a result, we can't match the tunneling frequency plots with experimental data except at a few isolated points.

Because of the momentum quantization imposed by the dynamics of the experiment, we found that it was advantageous to use Floquet theory rather than Floquet-Bloch theory to analyze the experiment. The Floquet states and their corresponding quasienergies provide sufficient information to calculate dynamic tunneling frequencies. Apparently, the initial state can be adequately represented by a sum of Floquet states. The Floquet states which dominate the dynamics are the ones with the greatest overlap probability with the initial state.

Differences in the quasienergies of the dominant Floquet states give the

available frequencies for dynamic tunneling. If two Floquet states dominate the dynamics, then only one tunneling frequency will be observed. If three Floquet states dominate, then up to three tunneling frequencies are observable.

If a small number of Floquet state do not dominate, then no particular frequency will be observed. The full spectrum of frequencies is simultaneously and equally present. This condition would hold if there are no resonance islands to concentrate the Floquet states. By comparing Husimi plots to Strobe plots, it is obvious that some Floquet states tend to position themselves over the larger resonances. This allows an initial state which is sitting on a resonance to be decomposed into a small subset of the Floquet states. This in turn means that only a few tunneling frequencies will be present which enables them to be observed.

When multiple frequencies are predicted to be observable, sometimes not all of them are actually measured. The predicted oscillations that have a high frequency may simply be too high to be measured. There may be insufficient data to resolve the higher frequencies, or the high frequency oscillations may be lost due to dissipation. It is curious that the missing frequencies also tend to be the ones that are on oscillation curves that have large slopes. For example, of the three frequencies predicted by Fig. 4.9 in the NIST system, the only one reported by the experimentalists is on the curve which is relatively flat as a function of the pendulum amplitude, κ . For the Texas system, the largest error bars that are reported by the experimentalists [62] occur when the theoretical curves in Fig. 3.6 have the greatest slope.

As a result of these observations, measurement of tunneling frequencies seems to have two requirements. The primary requirement is having only a few dominant Floquet states in the decomposition of the initial state. Secondly, in the parameter regime of interest, the differences in the Floquet quasienergies of the dominant states needs to remain fairly constant.

In both experiments, the number of states within the chaotic region is very small. As a result, the Floquet states are very large relative to the size of the dynamical features. In particular, the Floquet states that sit on the resonance islands completely cover the islands and extend into the chaotic region. This means that initial states that are located within an island are not truly isolated from the chaotic region.

To achieve better isolation, we need to move to the semiclassical regime. In this regime, there will be many more states within the dynamical region of interest and the Floquet states will be smaller. It is conceivable that an initial state will then be a superposition of states that are almost completely confined to the regular region of a resonance island. We would then expect it to be easier to test for processes such as chaos-assisted tunneling.

Appendix

Appendix 1

Computer Codes

Much of the work of this thesis is numerical, so I will detail some of the code used to perform the simulations. I will limit the code to the more important routines and leave out the more common, but necessary, routines like the Runge-Kutta integrator which can be found in many numerical books [?].

1.1 Lyapunov Exponent

There are a number of ways to find the maximum exponent. The simplest is to just use a secondary orbit that is very close to the initial condition of interest. After evolving both orbits for a short period of time, the deviation is examined and stored. If necessary, the location of the secondary orbit is renormalized along the deviation vector so that it won't grow too large [5, 36].

```
double rksize = GetSTime(1e-7); // Runge-Kutta step size
int lyapsteps = 150000; // number of renormalization steps
int lyapout = 1000; // number of steps between outputs
double lyaptime = GetSTime(1e-2); // final time
double lyapsize = GetSTime(5e-6); // renormalization step
double lyapd0 = 1.0e-4; // nearby point distance
```

```

void GetLyap(double q0, double p0, int n, int nout,
double tau, double d0, ofstream& out) {
// Setup Calculation for Lyapunov Exponent
// y -> state vector
// n -> number of rescaling time steps (e.g. 1e5)
// nout -> number of time steps to skip before printing
// tau -> time between rescaling (about 0.2)
// d0 -> magnitude of the displacement (magnitude = 3e-4)

// Initial State
int nq = neq;
double* y = GetArray(nq);
y[0] = q0; y[1] = p0; //InitializeState(y,E);

// Get Displacement Vectors
double *d, *lyapvec;

// random normalized initial vector
srand(time(NULL));
double dmag=0; d = GetArray(neq);
for (int i=0; i<neq; i++) {
    d[i]= rand(); dmag += d[i]*d[i];

```

```

    }

    dmag = sqrt(dmag);
    for (int i=0; i<neq; i++) { d[i] *= d0/dmag; } // norm

    // Calculate Exponent
    double lyap = Lyap(n,tau,y,d,nout,out);

    // Print Result
    if (nout==0)
        out << GetRTime(n*tau) << "    " << lyap << endl;

    delete[] y;
    delete[] d;
}

double Lyap(int n, double tau, double* x, const double* d,
    int nout, ofstream& out) {
    // Benettin Method for Getting Largest Lyapunov Exponent
    // n -> number of time steps (e.g. 1e5)
    // tau -> time between rescaling (about 0.2)
    // x -> trajectory initial value
    // d -> displacement vector (magnitude = 3e-4)
    // nout -> number of time steps to skip before printing

```

```

double *y = GetArray(neq), *xold = GetArray(neq);
double *yold = GetArray(neq);

// Initial State
double d0 = 0, dmag = 0;
for (int i=0; i<neq; i++) {
    y[i] = x[i] + d[i];          // second point
    d0 += d[i]*d[i];             // euclidian norm
}
d0 = sqrt(d0);

// Iterate Forward
double h = rksize, hold; if (h>tau) h = tau;
double t, t0 = t0, tf, tr = 0, dt = 0;
double pinterval = nout*tau;
double dratio, lyap = 0, realt0 = GetRTime(t0);
double realtau = GetRTime(tau);
for (int i=0; i<n; i++) {
    // Iteration of Both Points
    t = t0 + tau*i; tf = t0 + tau*(i+1);
    hold = h; rev1 += Iterate(x,xold,t,tf,h);
    h = hold; rev2 += Iterate(y,yold,t,tf,h);
}

```

```

// Rescale Displacement
dmag = 0;
for (int j=0; j<neq; j++)
    dmag += pow(y[j]-x[j],2);
dmag = sqrt(dmag); dratio = d0/dmag;
for (int j=0; j<neq; j++) {
    y[j]-=x[j]; y[j]*=dratio; y[j]+=x[j];
}

// Print Intermediate Value
lyap += log(1/dratio);
if (nout>0 && (i+1)%nout==0) {
    out << (realt0+(i+1)*realtau) << " " // in s
<< lyap/((i+1)*realtau) << endl; // in s^-1
}
}

lyap /= n*realtau; // in s^-1

delete [] y;
delete [] xold;
delete [] yold;;

return lyap;

```



```
}
```

1.2 Quantum Floquet Analysis

The following code uses IMSL routines to find the Floquet matrix and its eigenvectors and eigenvalues. Additionally, the overlap with an initial coherent state is calculated which is used to find the dominant Floquet states.

```
#include "parameters.h"

/* matrices: k=0 is real part, k=1 is imag part */
#define floq(i,j,k)    floq[(j)*2*ldfloq+2*(i)+(k)]
#define eigvec(i,j,k)  eigvec[(j)*2*ldvec+2*(i)+(k)]

/* right hand side of differential equations */
void rights( int *, float *, float *, float *);

main(int argc, char *argv[]){
    float *y, *floq, *eigval, *eigvec;

    /* IMSL Parameters */
    /*-----*/
    memset(param, 0x00, 50*sizeof(float));
    param[3] = 50000000; /* used by IVPRK */
}
```

```

/* Allocate memory for the state vector */
if((y=(float*)calloc(2*nk,sizeof(float)))
    == NULL){
    printf("Error allocating memory");
    exit(1);
}

/* Allocate memory for the matrix */
ldfloq = ldevec = nk;
if((floq=(float*)calloc(2*ldfloq*nk,sizeof(float)))
    == NULL){
    printf("Error allocating memory");
    exit(1);
}

/* Allocate memory for the eigenvalues */
if((eigval=(float*)calloc(2*nk,sizeof(float)))
    == NULL){
    printf("Error allocating memory");
    exit(1);
}

/* Allocate memory for the eigenvectors */
if((eigvec=(float*)calloc(2*ldevec*nk,sizeof(float)))
    == NULL){
    printf("Error allocating memory");

```

```

    exit(1);
}

/* Open Data Files */
/*-----*/
ofloqptr = OpenFile(floqfile, "w");
oeigvalptr = OpenFile(eigvalfile, "w");
oeigvecptr = OpenFile(eigvecfile, "w");

/* Calculate Floquet Matrix */
/*-----*/
for(init=0; init<neq; init+=2){

    /* initialize y to zero except for initial p */
    for(i = 0; i<neq; i+=2){
        y[i] = 0;           /* real part */
        y[i+1] = 0;         /* imaginary part */
    }
    y[init] = 1;

    /* integrate equations */
    t = 0.0;
    tend = period;

```

```

ido = 1;
IVPRK(&ido,&neq,rights,&t,&tend,&tol,param,y);

/* floquet matrix */
for(i = 0; i < neq; i+=2){
    floq(i/2,init/2,0) = y[i];    /* real part */
    floq(i/2,init/2,1) = y[i+1]; /* imag part */
}

/* cleanup */
ido = 3;
IVPRK(&ido,&neq,rights,&t,&tend,&tol,param,y);
}

/* Print Out Floquet Matrix */
/*-----*/
for(i = 0; i < nk; i++){
    for(j = 0; j < nk; j++){
        fprintf(ofloqptr, "%14.8f", floq(i,j,0));
        fprintf(ofloqptr, "\n");
    }

    fprintf(ofloqptr, "\n");
}

```

```

for(i = 0; i < nk; i++){
    for(j = 0; j < nk; j++){
        fprintf(ofloqptr, "%14.8f", floq(i,j,1));
        fprintf(ofloqptr, "\n");
    }

/* Calculate Eigenvalues & Eigenvectors */
/*-----*/
/* Eigenvectors are stored in the columns */
EVCCG(&nk, floq, &ldfloq, eigval, eigvec, &ldevec);

/* Print Eigenvalues */
/*-----*/
for(i = 0; i < nk; i++){
    fprintf(oeigvalptr,"%9.6f  %9.6f",
        eigval[2*i],eigval[2*i+1]);
}

/* Print Eigenvectors */
/*-----*/
for(i = 0; i < nk; i++){
    for(j = 0; j < nk; j++)

```

```

        fprintf(oeigvecptr,"%15.7e %15.7e  ",
                eigvec(i,j,0), eigvec(i,j,1));
    fprintf(oeigvecptr, "\n");
}

```

```

/* Overlap with Gaussian */
/*-----*/
/* Initialize y to upper Gaussian */
p = -no; /* y[0] is <p=-no|y> */
mag = pow(sig*sig/M_PI,0.25);
for(i = 0; i<neq; i+=2){
    y[i] = mag*cos((p-p0)*x0);
    y[i] *= exp(-sig*sig*(p-p0)*(p-p0)/2);
    y[i+1] = -mag*sin((p-p0)*x0)
    y[i+1] *= exp(-sig*sig*(p-p0)*(p-p0)/2);
    p++;
}

```

```

/* Calculate overlaps */
for(j = 0; j < nk; j++){
    overlap_r = 0;
    overlap_i = 0;
    for(i = 0; i < nk; i++) {

```

```

        overlap_r += eigvec(i,j,0)*y[2*i];
        overlap_r += eigvec(i,j,1)*y[2*i+1];
        overlap_i += eigvec(i,j,0)*y[2*i+1];
        overlap_i -= eigvec(i,j,1)*y[2*i];
    }
    fprintf(oeigvalptr, "%12.9f\n",
        sqrt(overlap_r*overlap_r + overlap_i*overlap_i));
}

/* Cleanup */
/*-----*/
free(y);
free(floq);
free(eigval);
free(eigvec);
return;
}

```

Bibliography

- [1] M. Abramowitz and I. A. Stegun, editors. *Handbook of Mathematical Functions*. Dover, New York, 1972.
- [2] A. Ashkin. Atomic-beam deflection by resonance-radiation pressure. *Phys. Rev. Lett.*, 25:1321–1324, 1970.
- [3] Vitali Averbukh, Shmuel Osovski, and Nimrod Moiseyev. Controlled tunneling of cold atoms: From full suppression to strong enhancement. *Phys. Rev. Lett.*, 89:253201, 2002.
- [4] Basil Barbanis. On the isolating character of the third integral in a resonance case. *The Astronomical Journal*, 71:415–424, 1966.
- [5] Giancarlo Benettin, Luigi Galgani, and Jean-Marie Strelcyn. Kolmogorov entropy and numerical experiments. *Phys. Rev. A*, 14:2338–2345, 1976.
- [6] C. F. Bharucha, J. C. Robinson, F. L. Moore, Bala Sundaram, Qian Niu, and M. G. Raizen. Dynamical localization of ultracold sodium atoms. *Phys. Rev. E*, 60(4):R19–R22, 1999.
- [7] O. Bohigas. *Chaos and Quantum Physics*. Elsevier, Amsterdam, 1991.
- [8] O. Bohigas, M. J. Giannoni, and C. Schmit. Characterization of chaotic quantum spectra and universality of level fluctuation laws. 52:1–4, 1984.

- [9] O. Bohigas, S. Tomsovic, and D. Ullmo. Classical transport effects on chaotic levels. 65:5–8, 1990.
- [10] O. Bohigas, S. Tomsovic, and D. Ullmo. Dynamical quasidegeneracies and separation of regular and irregular quantum levels. 64:1479–1482, 1990.
- [11] H. P. Breuer and M. Holthaus. A semiclassical theory of quasienergies and floquet wave functions. *Annals of Physics*, 211:249–291, 1991.
- [12] M. Casartelli, E. Diana, L. Galgani, and A. Scotti. Numerical computations on a stochastic parameter related to the kolmogorov entropy. *Phys. Rev. A*, pages 1921–1925, 1976.
- [13] S. J. Chang and K. J. Shi. Time evolution and eigenstates of a quantum iterative system. *Phys. Rev. Lett.*, 55:269, 1985.
- [14] S. J. Chang and K. J. Shi. Evolution and exact eigenstates of a resonant quantum system. *Phys. Rev. A*, 34:7, 1986.
- [15] W. Chism, T. Timberlake, and L.E. Reichl. High harmonic generation in systems with bounded chaos. *Phys. Rev. E*, 58(2):1713–1723, 1998.
- [16] M.J. Davis and E. J. Heller. Quantum dynamical tunneling in bound states. *J. Chem. Phys.*, 75:246–254, 1981.
- [17] C. Dembowski, H. D. Graf, A. Heine, R. Hofferbert, H. Rehfeld, and A. Richter. First experimental evidence for chaos-assisted tunneling in a microwave annular billiard. *Phys. Rev. Lett.*, 84:867–870, 2000.

- [18] S. Dyrting, G. J. Milburn, and C. A. Holmes. Nonlinear quantum dynamics at a classical second-order resonance. *Phys. Rev. E*, 48:969–978, 1993.
- [19] Sigurd Dyrting. *Quantum Chaos in Atom Optics*. PhD thesis, University of Queensland, Australia, April 1995.
- [20] Albert Einstein. Zum quantensatz von sommerfeld und epstein. *Verh. Deut. Phys. Ges.*, 19:82, 1917.
- [21] M. A. Feit, J. A. Fleck, and A. Steiger. Solution of the schrodinger equation by a spectral method. *Journal of Computational Physics*, 47, 1982.
- [22] J. A. Fleck, J. R. Morris, and M. A. Feit. *Applied Physics*, 10, 1976.
- [23] S. D. Frischat and E. Doron. Dynamical tunneling in mixed systems. *Phys. Rev. E*, 57:1421–1443, 1998.
- [24] R. Graham, M. Schlautmann, and P. Zoller. Dynamical localization of atomic-beam deflection by a modulated standing light wave. *Phys. Rev. A*, 45(1):R19–R22, 1992.
- [25] M. C. Gutzwiller. Energy spectrum according to classical mechanics. *J. Math. Phys.*, 11:1791–1806, 1970.
- [26] T. W. Hansch and A. L. Schawlow. Cooling of gases by laser radiation. *Opt. Commun.*, 13:68–69, 1975.

- [27] E. J. Heller. Quantum effects in intramolecular energy transfer. *Chem. Phys. Lett.*, 60:338, 1979.
- [28] Michel Henon and Carl Heiles. The applicability of the third integral of motion: Some numerical experiments. *The Astronomical Journal*, 69:73–79, 1964.
- [29] W. K. Hensinger, H. Haffner, A. Browaeys, N. R. Heckenberg, K. Helmer-son, C. McKenzie, G. J. Milburn, W. D. Phillips, S. L. Rolston, H. Rubinsztein-Dunlop, and B. Upcroft. Dynamical tunnelling of ultracold atoms. *Nature*, 412:52–55, 2001.
- [30] W. K. Hensinger, A. G. Truscott, B. Upcroft, M. Hug, H. M. Wiseman, N. R. Heckenberg, and H. Rubinsztein-Dunlop. Experimental study of the quantum driven pendulum and its classical analog in atom optics. *Phys. Rev. A*, 64:033407, 2001.
- [31] K. Husimi. *Proc. Phys. Math. Soc. Jpn.*, 22:264, 1940.
- [32] R. V. Jensen, M. M. Sanders, M. Saraceno, and B. Sundaram. Inhibition of quantum transport due to “scars” of unstable periodic orbits. *Phys. Rev. Lett.*, 63:2771–2775, 1989.
- [33] M. Kozuma, L. Deng, E. W. Hagley, J. Wen, R. Lutwak, K. Helmer-son, S. L. Rolston, and W. D. Phillips. Coherent splitting of bose-einstein condensed atoms with optically induced bragg diffraction. *Phys. Rev. Lett.*, 82:871–875, 1999.

- [34] M. Latka, P. Grigolini, and B. J. West. Chaos-induced avoided level crossing and tunneling. *Phys. Rev. A*, 50:1071–1081, 1994.
- [35] P. Leboeuf and A. Mouchet. Tunneling and the band structure of chaotic systems. *Phys. Rev. Lett.*, 73:1360–1363, 1994.
- [36] A. J. Lichtenberg and M. A. Lieberman. *Regular and Chaotic Dynamics*. Springer-Verlag, New York, second edition, 1991.
- [37] W. A. Lin and L. E. Ballentine. Quantum tunneling and chaos in a driven anharmonic oscillator. *Phys. Rev. Lett.*, 65:2927–2930, 1990.
- [38] Robert Luter and L. E. Reichl. Floquet analysis of atom-optics tunneling experiments. *Phys. Rev. A*, 66:53615, 2002.
- [39] Robert Luter and L. E. Reichl. Tunneling between floquet states in atom optics experiments. *International Journal of Modern Physics B*, 17:4101–4112, 2003.
- [40] Robert Luter and L. E. Reichl. Tunneling between floquet states using a bose-einstein condensate. *J. Phys. Soc. Jpn.*, 72:134–139, 2003.
- [41] Pierre Meystre and Murray Sargent III. *Elements of Quantum Optics*. Springer-Verlag, New York, 1991.
- [42] F. L. Moore, J. C. Robinson, C. F. Bharucha, P. E. Williams, and M. G. Raizen. Observation of dynamical localization in atomic momentum

- transfer: A new testing ground for quantum chaos. *Phys. Rev. Lett.*, 73:2974–2977, 1994.
- [43] Gregory Oren Morrow. *Scaling of Localization Lengths in Quantum Dynamics*. PhD thesis, University of Texas at Austin, Austin, TX, May 1997.
 - [44] A. Mouchet, C. Miniatura, R. Kaiser, B. Gremaud, and D. Delande. Chaos-assisted tunneling with cold atoms. *Phys. Rev. E*, 64:016221, 2001.
 - [45] Amaury Mouchet and Dominique Delande. Signatures of chaotic tunneling. *Phys. Rev. E*, 67:046216, 2003.
 - [46] Marcel Novaes. Wigner and husimi functions in the double-well potential. *J. Opt. B*, 5:S342–S348, 2003.
 - [47] Asher Peres. Dynamical quasidegeneracies and quantum tunneling. *Phys. Rev. Lett.*, 67:158, 1991.
 - [48] J. L. Picque and J. L. Vialle. Atomic-beam deflection and broadening by recoils due to photon absorpton or emission. *Opt. Commun*, 5:402, 1972.
 - [49] William H. Press, Saul A. Teukolshy, William T. Vetterling, and Brian R. Flannery. *Numerical Recipes in C*. Cambridge University Press, Cambridge, New York, 1992.

- [50] L. E. Reichl. *Transition to Chaos in Conservative Classical Systems: Quantum Manifestations*. Springer-Verlag, New York, 1992.
- [51] J. C. Robinson, C. Bharucha, R. Jahnke, G. A. Georgakis, M. G. Raizen, Q. Niu, and Bala Sundaram. Study of quantum dynamics in the transition from classical stability to chaos. *Phys. Rev. Lett.*, 74:3963–3966, 1995.
- [52] J. C. Robinson, C. Bharucha, K. W. Madison, F. L. Moore, Bala Sundaram, S. R. Wilkinson, and M. G. Raizen. Can a single-pulse standing wave induce chaos in atomic motion. *Phys. Rev. Lett.*, 76:3304–3307, 1996.
- [53] John Charles Robinson. *Atom Optics: A New Testing Ground for Quantum Chaos*. PhD thesis, University of Texas at Austin, Austin, TX, December 1995.
- [54] J. J. Sakurai. *Modern Quantum Mechanics*. Addison-Wesley, Reading, Massachusetts, revised edition, 1992.
- [55] H. Sambe. Steady states and quasienergies of a quantum-mechanical system in an oscillating field. *Phys. Rev. A*, 7:2203–2213, 1973.
- [56] R. Schieder, H. Walther, and L. Woste. Atomic-beam deflection by the light of a tunable dye laser. *Opt. Commun.*, 5:337, 1972.
- [57] Marlan O. Scully and M. Suhail Zubairy. *Quantum Optics*. Cambridge University Press, Cambridge, 1997.

- [58] J. H. Shirley. Solution of the schr odinger equation with a hamiltonian periodic in time. *Phys. Rev.*, 138:979–987, 1965.
- [59] Rex T. Skodje, Henry W. Rohrs, and James VanBuskirk. Flux analysis, the correspondence principle, and the structure of quantum phase space. *Phys. Rev. A*, 40:2894–2916, 1989.
- [60] Daniel A. Steck, Valery Milner, Windell H. Oskay, and Mark G. Raizen. Quantitative study of amplitude noise effects on dynamical localization. *Phys. Rev. E*, 62:3461–3475, 2000.
- [61] Daniel A. Steck, Windell H. Oskay, and Mark G. Raizen. Observations of chaos-assisted tunneling between islands of stability. *Science*, 293:274–277, 2001.
- [62] Daniel A. Steck, Windell H. Oskay, and Mark G. Raizen. Fluctuations and decoherence in chaos-assisted tunneling. *Phys. Rev. Lett.*, 88(12):120406, 2002.
- [63] Daniel Adam Steck. *Quantum Chaos, Transport, and Decoherence in Atom Optics*. PhD thesis, University of Texas at Austin, Austin, TX, December 2001.
- [64] K. Takahashi. *Prog. Theor. Phys. Suppl.*, 98:109, 1989.
- [65] K. Takahashi and N. Saito. Chaos and husimi distribution function in quantum mechanics. *Phys. Rev. Lett.*, 55:645–648, 1985.

- [66] Todd Timberlake and L.E. Reichl. Changes in Floquet-state structure at avoided crossings: Delocalization and harmonic generation. *Phys. Rev. A*, 59(4):2886–2893, 1999.
- [67] Steven Tomsovic. Chaos-assisted tunneling in the absence of reflection symmetry. *J. Phys. A: Math. Gen.*, 31:9469–9481, 1998.
- [68] Steven Tomsovic. Tunneling and chaos. *Physica Scripta*, T90:162–165, 2001.
- [69] Steven Tomsovic and Denis Ullmo. Chaos-assisted tunneling. *Phys. Rev. E*, 50:145–162, 1994.
- [70] Carl Wieman and Leo Hollberg. Using diode lasers for atomic physics. *Rev. Sci. Inst.*, 62:1, 1991.
- [71] Y. B. Zeldovich. *Sov. Phys. JETP*, 24:1006, 1967.

Index

- Abstract, vi
- Acknowledgments*, v
- Atom Optics*, 1

- Bibliography*, 120
- bifurcation, 51

- cantori, 50
- Classical Chaos
 - Poincaré Surfaces of Section*, 14
- Classical Chaos*, 3, 14
- Computer Codes*, 100
- Conclusions*, 96

- Dedication*, iv
- Double Well System
 - Energy Levels*, 7
 - Tunneling*, 11
 - Wave Functions*, 10
- Double Well System*, 7
- Dynamic Tunneling
 - Modulated Potential Well View*, 35
 - Moving Lattice View*, 38
- Dynamic Tunneling*, 34
- dynamic tunneling, 4

- Floquet Theory*, 25

- General Theory*, 7

- Hamiltonians in Atom Optics*, 30
- Henon-Heiles System*, 15
- Husimi Plots*, 29

- Introduction*, 1

- KAM tori, 3, 50

- NIST Experiment
 - Classical Dynamics*, 77
 - Experiment Hamiltonian*, 74
 - Experimental Results*, 75
 - Floquet Analysis*, 79
 - Floquet States for Varying Amplitude*, 89
 - Floquet States for Varying Modulation*, 82
 - Hamiltonian Derivation*, 74
 - Hamiltonian Scaling*, 75
 - Quantum Evolution*, 78
 - System Model*, 74
 - Theoretical Hamiltonian*, 76
- NIST Experiment*, 74

- Pendulum*, 31
- Periodic Hamiltonians*, 17
- Poincaré Surfaces of Section, 14

- Quantum Chaos*, 3

- Strobe Plots*, 18

- Texas Experiment
 - Classical Dynamics*, 49
 - Experiment Hamiltonian*, 40
 - Experimental Results*, 47
 - Floquet Analysis*, 59
 - Hamiltonian Derivation*, 42
 - Hamiltonian Scaling*, 46

Quantum Evolution, 54
System Model, 40
Theoretical Hamiltonian, 47
Texas Experiment, 40
Tunneling, 4
Underwater Acoustics, 18

Vita

Robert Raymond Luter, Jr. was born in Corpus Christi, Texas in 1959. After his family moved to Austin a few years after his birth, he went to school in Austin and eventually graduated from Lanier High School. For college, he attended the University of Texas in Austin and graduated with a B.S. in Aerospace Engineering. He was then commissioned as an officer in the United States Air Force. The Air Force sent him to Wright-Patterson AFB to the Air Force Institute of Technology where he ultimately received a M.S. in Astronautical Engineering. He then served as an engineering officer for a number of years at Los Angeles AFB while working on various satellite programs for Space Division of the USAF. After leaving the service, he attending classes in physics at the University of California in Los Angeles. After completing work at UCLA, he moved back to Austin to attend the University of Texas. He subsequently joined the statistical mechanics group and started working with Dr. Linda Reichl on topics in quantum chaos theory.

Permanent address: 8807 Redfield Ln. Apt. 215
Austin, Texas 78758

This dissertation was typeset with \LaTeX^\dagger by the author.

[†] \LaTeX is a document preparation system developed by Leslie Lamport as a special version of Donald Knuth's \TeX Program.